METAL-TRANSFER-MOLDING (MTM) TECHNIQUE FOR MICROMACHINED RF COMPONENTS

A Dissertation
Presented to
The Academic Faculty

By

Yanzhu Zhao

In Partial Fulfillment of the Requirements for
the Degree of

Doctor of Philosophy
in Electrical and Computer Engineering

Georgia Institute of Technology

June 2008

Dedicated to my family

ACKNOWLEDGEMENTS

First and foremost, I would like to express my deepest gratitude to my advisor, Professor Mark G. Allen, for his support, faith, superb and patient guidance throughout my pursuit of PhD. I am grateful for spending time under his mentorship, and his model role also help to shape my research attitude. It has been my honor to have him as my advisor.

I would like to thank Professor J. Stevenson Kenney for serving as the chairman for my proposal examination and thesis committee. I would also like to thank Professor Oliver Brand, Professor Joy Laskar, and Professor Peter J. Hesketh for serving on my thesis committee. I appreciate their advice and support, which was invaluable to my degree completion.

I would like to acknowledge the members of the Microsensors and Microactuators (MSMA) group at Georgia Institute of Technology for their unforgettable support, advice, and friendship. Special thanks go to Dr. Yong-Kyu Yoon, Dr. Yoon-Su Choi, Dr. Jin-Woo Park, Dr. Guang Yuan, Dr. Florent Cros, Dr. Brian English, Dr. Michael Fonseca, Dr. Seong-Hyok Kim and Xiaosong Wu for their idea and help with the laboratory process development. I would also like to express my great gratitude to Bo Pan and Yuan Li for their generous help with the device characterization. I would also like to thank Mr. Richard Shafer, laboratory manager, and Mrs. Purnima Sharma, laboratory administrator, for their help with the technical and administrative works. I would like to thank the staff of the Microelectronics Research Center, their work maintaining the operation of the cleanroom is extremely important for my research. I would also like to thank Dr. Guoan

Wang and Gang Huang for their friendship through my school days at Georgia Tech.

I gratefully thank my parents for their love and care. I owe them a huge debt of gratitude for their selfless support and encouragement.

Last but not least, I would like to thank my parents, parents-in-law, and my wonderful wife and lifelong friend, Xintian Gu, and my dear daughter, Emily Zhao, for their endless love, faith, support and encouragement. Without them, I could not have made it through my Ph.D. study.

CONTENTS

LIST OF TABLES

LIST OF FIGURES

SUMMARY

This dissertation reports a metal-transfer-molding (MTM) technique for simultaneous implementation of air-lifted RF passive components, as well as coplanar waveguide (CPW) structures, in a high performance and potentially cost-effective fashion. A metal transfer mechanism is introduced into the conventional micro-molding process to realize polymer-core RF passive components and integration. A system-on-package (SOP) integration scheme of front-end RF components can be realized by this process.

Several air-lifted RF components based on MTM technology have been presented with excellent performance. The first component is a CPW bandstop filter on a flexible organic substrate. The filter comprises a unique air-gap CPW to reduce the dependence of filter performance on substrate non-idealities. The measured characteristic shows a loss of less than 2.5dB in passband and more than 20dB in stopband, with more than 40% lower loss than a conventional planar filter. The second component is an integrated Ka-band monopole antenna array, with resonant frequency ranging from 26GHz to 42GHz in a compact size. 21.5% 10dB bandwidth for the monopole antennas has been achieved. The third component is a reduced-size high-Q cavity resonator based on evanescent-mode operation. An unloaded Q exceeding 500 and more than 40% size reduction have been achieved from micromolded organic materials.

As an integration application of the MTM technology, a novel wireless passive airflow sensor based on the RF evanescent-mode cavity resonators has been also

presented. The sensor makes use of RF technology to measure wind velocity through changes in the resonant frequency with applied airflow. Compared with reported wireless sensors based on conventional RF cavity resonator, this design has advantages such as compact size and greatly improved sensitivity. The presented airflow sensor shows a 360MHz frequency shift per m/s airflow. By embedding an ultra-wide-bandwidth monopole (UWB) antenna, wireless interrogating has also been demonstrated for the passive sensor. The resonance shift has been successfully detected in wireless measurement.

Overall, the RF components developed in this thesis illustrate the great potential of MTM technology in both wireless communication and sensor areas.

Chapter 1

Introduction

1.1 RF Front-end Components

1.1.1 Current RF Front-End Module for Wireless Communication system

The past decades have witnessed a rapid growth in high-frequency (2-100GHz), microwave and millimeter wave wireless communication markets. New standards include mobile Wireless Local Access Network (WLAN), Local Multipoint Distribution System (LMDS) and satellite communications (GPS, Direct TV, Multifunction Advanced Data Link (MADL)). All of these standards desire high performance while maintaining low cost, small volume and integration capability.

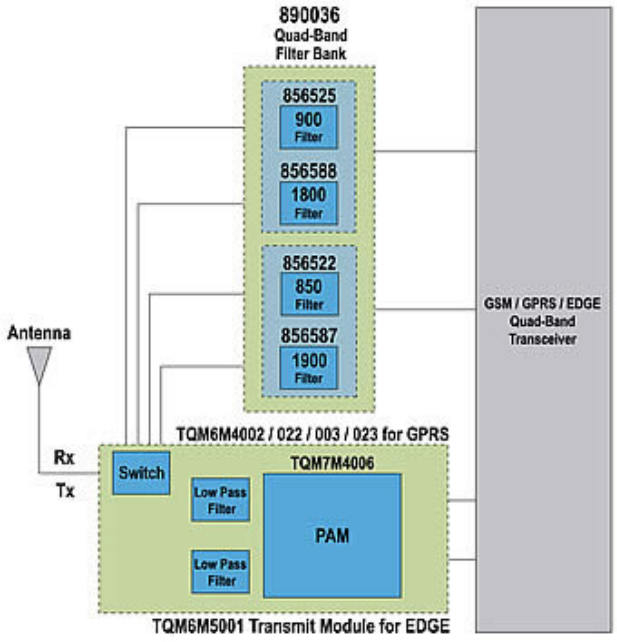

Figure 1.1 Schematic of TriQuint Semiconductor RF front-end design for WCDMA/EDGE handsets [1]

Generally, wireless subsystems consist of different components such as high frequency transceivers and digital processors. The RF front-end is a key part between the antenna and the digital baseband system. Figure 1.1 shows an example RF front-end module for WCDMA/EDGE handsets by TriQuint, Inc [1]. For a receiver, this front-end includes all the filters, low-noise amplifiers (LNAs), and down-conversion mixers needed to process the modulated signals received at the antenna into signals suitable for input into the baseband analog-to-digital converter (ADC). Sensitivity and selectivity are the primary concerns in receiver design. Conversely, a transmitter up-converts an outgoing signal prior to passage through a high power amplifier [2, 3]. The design of the receiver and transmitter share many common elements—such as local oscillators or antennas.

RF front-end is the most critical part of the entire transceiver. RF front-ends are composed of both integrated circuits (ICs) and passive devices including antennas and filters that are not integrated on the semiconductor substrate. These components are based on different materials and technologies. While the integration of active components in RF systems has paralleled the rapid progress of IC technology, resulting in the fact that the active components of RF systems occupy only a small fraction of board real estate, passive components have not advanced in a similar manner, not only because of geometrical scaling limitations governed by operating frequency, but also because of the lack of mature fabrication technologies for high quality factor (Q) passive integration. Furthermore, these new requirements for next generation microwave systems are hard to realize at the same time by using traditional RF circuit designs. Innovations in RF front-end passive component designs must be made to improve RF performance with continued affordability. Antennas and filters/duplexers are key components in RF front-end circuits,

and the need of reduced size and high performance requires novel RF front-end architectures and new fabrication techniques.

1.1.2 Millimeter-wave antennas

For the past several decades, substantial progress in millimeter wave antennas has been made for use in a wide range of applications such as radio astronomy, radar, imaging, or communication systems [4, 5]. These antennas include wire antennas (dipoles, monopoles, Yagi-Uda antennas, loops, etc.), patch antennas (microstrips, patch resonators, etc.), aperture antennas (rectangular horns, circular apertures, etc.), reflector antennas (parabolic reflectors, corner reflectors, etc.), and end-fire antennas (Vivaldi, tapered slots etc.) [6]. Advanced millimeter wave systems would benefit from having these radiating elements integrated with transmitting or receiving circuits on the same substrates in a monolithic form; such systems have the advantages of compactness, portability, and low-cost in mass production. Among the various antenna schemes, planar printed circuit antennas for monolithic millimeter wave systems have been considered as promising candidates because of their low profile, light weight, conformability, low-cost, and ease of manufacture. There is an increasing interest in complete monolithic systems which combine antenna elements or arrays on the same substrates as integrated RF front-end detector and amplifier circuits [7]. In these applications, substrates are often much thicker and have higher dielectric constants than at lower frequencies. One of the advantages of having a thick substrate is that the expense of backside processing (such as thinning) is eliminated. However, the printed antennas on thick dielectric substrates suffer from severe degradation of the electrical performance due to surface waves, mutual

coupling, and dielectric loss of the substrate. Bandwidth and input impedance are additional properties that are strongly affected by substrate thickness [8]. The lowest order surface wave (TM0) has a zero cutoff frequency, and thus is excited to some degree even on very thin substrates. As the substrate becomes thicker, more surface wave modes can exist, and more power can be coupled into these waves. Mutual coupling between elements in arrays involves the transfer of power from one element to a nearby element via space waves (direct radiation) or by surface waves. Coupling levels greater than roughly 20-30 dB may have a deleterious effect on array performance. There have been efforts to reduce substrate effects, including thinning the substrates [9], using bandgap structures [10], and building very thin dielectric layers [11]. However, the improvement of the antenna performance is still limited and the additional processes greatly increase the costs.

1.1.3 High-Q Resonator

The sensitivity of a wireless receiver is determined by noise and nonlinearity in the RF front-end. The pre-select filter selects the desired frequencies from a wide spectrum. By doing this, the pre-select filter rejects all other nearby signals. It also suppresses large out-of-band interference which may overload (cause distortion due to strong signal) the front-end. In extremely high-power cases, the interference may even burn out the low-noise amplifier. On the other hand, the selectivity of the entire system is wholly governed by the pre-select filter. In a multi-functional system, there may be a wide range of working frequencies. Thus, high-Q narrow-band pre-select filters are necessary to reject the image frequencies and out-of band interference.

Resonators or filters based on lumped-element circuits can achieve a very compact size while maintaining good performance up to 10 GHz. The disadvantage of this approach is that it is not feasible to design a filter operating over 10 GHz because most of the embedded passive components resonate below 10 GHz, resulting in a decrease in Q as the frequency increases. Planar resonators based on microstriplines or coplanar waveguides (CPW) are low profile and easy to integrate. In Monolithic Microwave Integrated Circuit (MMIC) applications, most filters are half-wavelength microstrip filters, coplanar waveguide (CPW) filters and other planar filters. However, due to the high substrate loss and metal loss, their Q is usually below 300. CPW resonators typically have a Q below 200 due to the more severe metal loss [12]. The low Q translates into poor performance such as excessive insertion loss for a filter.

The traditional approach for the realization of high-Q filtering is using waveguide cavities, coaxial-line transmission line sections and/or dielectric resonator (DRs). Waveguide resonators typically have a very high Q value ranging between 3000 and 20000 [13]. They are widely used in wireless duplexers and wireless communication base stations where extremely sharp channel selections are required. However, complex transitions need to be designed to connect waveguide resonators/filters to other circuits. In addition, waveguide resonators/filters are bulky, heavy and expensive to fabricate. Therefore, only under circumstances where extremely high performance is required and relatively large volume is allowed are waveguide filters implemented. Coaxial-line resonators typically have a moderately high Q value between 1000 and 5000 [14]. Coaxial-line filters are relatively smaller than waveguide filters due to the high dielectric constant used. However, the higher the dielectric constant used, the lower the Q, due, for

example, to increased loss in the dielectric materials. Dielectric resonators have relatively small volumes with a Q of up to 50,000. Nevertheless, the resonant frequencies of a DR are very sensitive to temperature, humidity and electromagnetic interference. Thus they should be carefully packaged and tuned to work properly. As a result, the cost is increased significantly. Other high Q resonators such as film bulk acoustic resonators (FBAR) are difficult to integrate with other circuits [15]. Overall, the traditional non-planar approaches of high Q resonator are either bulky and costly, or difficult to integrate with other components in RF front-end circuits for current mobile wireless communication applications. High-Q resonators with relatively compact size and high integration capabilities are greatly desired for the next generation RF front-ends.

1.2 Motivation

1.2.1 Micromachined 3-D RF Components

While planar components suffer from poor performance in millimeter wave applications, and traditional non-planar components suffer from integration difficulties and high cost, micromachined 3-D RF structures have attracted much interest, because the additional degree of freedom provides great opportunities to improve performance, and the miniature size increases integration capabilities. However, those 3-D RF structures have not been widely reported yet. This is due in part because the fabrication of such non-planar devices is not easy and not cost-effective due to lengthy fabrication steps or assembly requirements. If an easy and efficient way for 3-D RF structure fabrication and integration is established, it would provide an alternative to planar components and give additional degrees of freedom in designing and implementing with optimized

performance. In last decades, new micromachining technologies that can be integrated with IC fabrication methods have been developed in the area of Micro-Electro-Mechanical-System (MEMS) [16-18]. Recently these technologies have been exploited for the fabrication of 3-D RF passive components.

Earlier efforts of 3-D RF passive components based on MEMS have been made to lumped components such as inductor and capacitor by using advanced MEMS technology [19-20]. Recently Y. K. Yoon and J. W. Park reported a 3-D high-aspect-ratio, high-Q solenoid-type RF inductor [21]. The inductor is 900μm in height and has a 600μm wide air-core area, shows a maximum Q-factor of 84 and inductance of 1.17nH at 2.6GHz. M. Ozgur, M. E. Zaghloul reports low cost CMOS inductors by backside micromachining for RF applications. Quality factors better than 16 are achieved for 10nH inductor have been achieved [22]. S. O. Choi and Y. K. Yoon demonstrated a tunable capacitor by using a micro-channel filled with two immiscible fluids of different dielectric constants as dielectric materials [23]. A tunable resonator based on the capacitor has been demonstrated with a tuning bandwidth of 15% (0.27Ghz) at 1.8Ghz.

Further efforts based on MEMS technology have been made to realize other front-end components such as transmission lines, antennas, and filters [24, 25]. Among these technologies, air-lifting of planar RF components by micromachining has been demonstrated to be very promising. By lifting the components from the substrate and generating a solely air interface instead of an air/dielectric interface, the substrate loss and dispersion can be minimized.

There are generally three air-lifting mechanisms reported for micromachined RF passive components. Figure 1.2 shows a schematic of the air-lifting mechanisms,

comprising: elevated air-lifting, vertical air-lifting, and extruded air-lifting. Compared with their planar counterparts, these components have micromachined 3-D metalized structures connected with transmission lines. In the following there is a brief review of these air-lifted RF components.

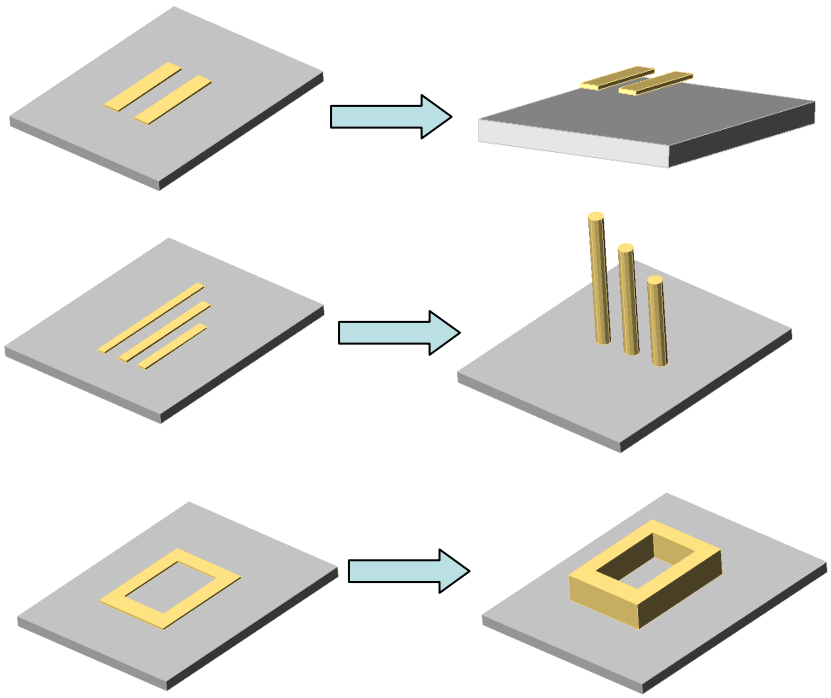

Figure 1.2 Schematic of the air-lifting mechanisms of RF components:
(a) elevated air-lifting (b) vertical air-lifting (c) extruded air-lifting

(a) Elevated air-lifting

This is the most common air-lifting mechanism in the literature. By elevating the printed components using MEMS fabrication technology, the substrate dielectric loss and dispersion characteristics due to the air/dielectric interface can be reduced. H. S. Lee and D. H. Shin reported a new type of dielectric-supported air-gapped microstrip line (DAML)

structure with the air-gapped area between the signal line and ground metal [26]. This DAML structure is developed using MEMS surface micromachining techniques with the air-bridge connection between the signal lines, in order to achieve low losses over the wide impedance range. A 1.1dB/cm line loss has been achieved by the proposed structure.

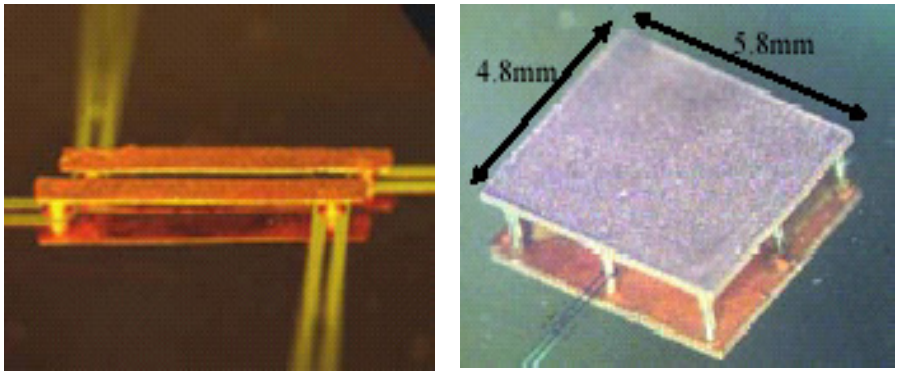

(a) Air lifted coupler [10] (b) Patch antenna [9]

Figure 1.3 Reported 3-D RF components by elevated air-lifting
(a) broadband coupler (b) patch antenna

B. Pan, Y. K. Yoon and Y. Zhao successfully demonstrate an elevated coupler by using surface micromachining technology [27] (Figure 1.3). A 10 dB return loss and a 12.5dB coupling has been achieved over the frequency range of 15GHz to 45GHz on a lossy soda-lime glass substrate. An elevated patch antenna with increased bandwidth and radiation pattern has also been reported recently [28] (Figure 1.3).

(b) Vertical air-lifting

Planar RF components usually have a size comparable to the half or quarter wavelength of the signal at the frequency of interest. Although the size can be reduced by using substrates with high dielectric constant, the substrate loss simultaneously increases. By vertically mounting the components, the substrate effect is minimized and the utilized area of the substrate can also be reduced. For example, a monopole antenna vertically standing on the substrate suffers less from substrate modes when compared to patch antennas since it is radiating the electromagnetic wave directly through the air.

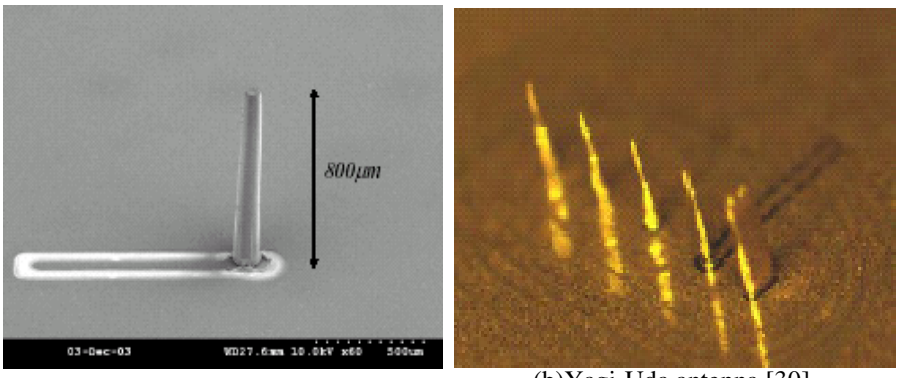

(a)W-band monopole antenna [29] (b)Yagi-Uda antenna [30]

Figure 1.4 Reported 3-D RF components by vertical air-lifting
(a) W-band monopole antenna (b) Yagi-Uda antenna

Y. K. Yoon and B. Pan report a vertically mounted W-band quarter wavelength monopole antenna by using high-aspect-ratio micromachining (Figure 1.4) [29]. The antenna has a height of 800um and 10dB bandwidth up to 15%. They further report a vertical Yagi-Uda antenna in W-band with a 10dB bandwidth up to 12% [30]. The radiation pattern is also greatly improved by using this air-lifting mechanism.

(c) Extruded air-lifting

By using extrusion of the planar structures, the presence of the substrate materials can be minimized. This airlifting mechanism is especially useful in high-Q cavity resonator or waveguides. Coplanar realization of a diplexer with planar resonators and filters is generally avoided due to their low quality factor and the substrate loss. While cavity resonators or waveguides have high-Q, the use of these waveguide components in high-frequency wireless communication systems has been limited, due in large part to their high cost of manufacturing and difficulties of integration. With the recent development in micromachining technologies, micromachined cavity resonators inside a silicon wafer have been demonstrated with measured unloaded Q of up to 4500 for Ka-band [31]. Y. Li further demonstrates a W-band CPW-fed waveguide filter with 2.9% bandwidth and a 4.14dB insertion loss in passband (Figure 1.5) [32].

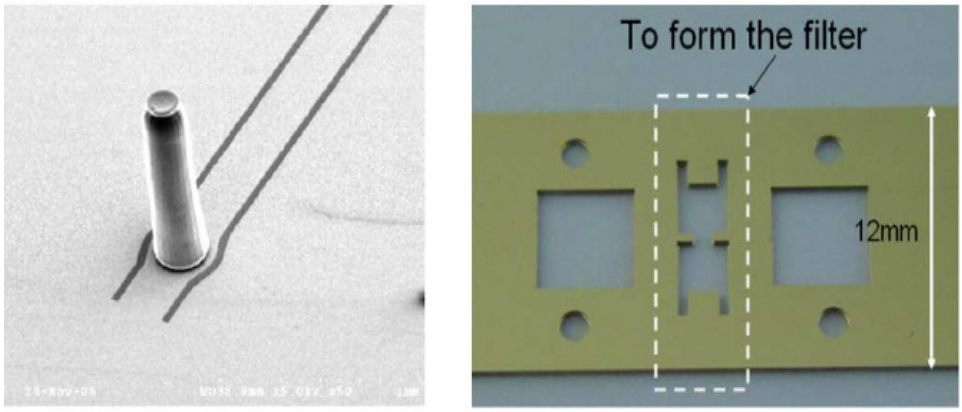

(a) (b)

Figure 1.5 Reported W-band CPW-fed RF waveguide filter by extruded air-lifting by Y. Li [32] (a) CPW feeding structures with probe; (b) micromachined cavity in silicon wafer

Overall, several types of 3-D RF front-end components have been successfully demonstrated respectively from antenna, coupler to filter. The performance is greatly

improved over the planar counterparts by using an air-lifting design approach. However, the fabrication techniques and materials vary greatly for the demonstrated components, including SU-8 surface micromachining, silicon deep etching, 3-D electroplating, and laser ablation. It is very challenging to fabricate and integrate these 3-D components by a common fabrication technology and material. Furthermore, it is difficult to find a suitable packaging method for these components with different materials and geometry.

1.2.2 RF System-on-Package (SOP)

The emergence of convergent systems requires an integrated solution for all sensing, computing, and communicating functions. Although there are various integration approaches like system-on-chip (SOC) and multi-chip-module (MCM), the system-on-package (SOP) approach has been identified as an attractive solution to assimilate multiple system functions into one compact, low-cost, high-performance package.

System-on-Chip (SOC) approach envisions a fully integrated system on a single wafer [33]. This approach is attractive from a cost standpoint, because the entire system (or chip) needs to be packaged only once. However, at higher frequencies (f>10GHz), standard silicon-based processes such as CMOS process suffer from low quality factor passives and poor RF isolation characteristics. Other SOC technologies such as gallium-arsenide (GaAs) have low substrate loss, but are more expensive. Silicon germanium (SiGe) is a lower cost replacement for GaAs for some applications, but it is still a relatively lossy substrate for passive RF components.

At high frequencies (f > 10 GHz), the best solution is to build passive functions on a separate low-loss RF substrate (the package). SOP is similar to the MCM approach, but allocates a greater responsibility to the package. In a MCM system, the package houses different chips, and performs the functions of powering, cooling and interconnecting these chips. In a SOP system, the package performs all the above mentioned functions; in addition, it houses passive functionality that is built on, or embedded inside, the package [34, 35]. Recently, there has been an increasing interest in developing a multilayer dielectric substrate SOP approach to achieve the integration of diverse passive and active components without compromising cost and size, including the LTCC and LCP technologies.

Low-temperature co-fired ceramic (LTCC) is one of the very few substrate technologies that satisfies nearly all the SOP requirements [36] at high frequency. It has the attractive feature that is can be laminated into multilayer homogeneous dielectric substrates and packages. Despite these advantages, LTCC may not be ideal for all applications. LTCC is expensive compared to conventional laminate materials, and it is not particularly suited for applications that require large amounts of horizontal real estate. Furthermore, printed antennas on LTCC substrates suffer from reduced efficiency because of the relatively high dielectric constant of the ceramic. Another disadvantage with the LTCC process is that its process temperature ($800^{\circ}C \sim 1000^{\circ}C$) may not be acceptable for some fully integrated solutions. Other drawbacks include the metallization techniques available with the LTCC process and the brittle nature of the material.

Liquid crystal polymer (LCP) has been identified as another candidate for SOP because of its excellent packaging characteristics [37]. LCP has a unique combination of

properties that makes it a viable technology for SOP-based systems. It is quasi-hermetic and has the potential to act both as a substrate and a package. Being a polymer, it is considerably cheaper compared to ceramics and other composite materials. Its multilayer lamination capabilities make it suitable for the integration of various modules. However, the integration cost is considerately higher than the conventional methods, and the substrate effects still remain for printed components.

Air-lifting of RF passive components has great potential for next generation high-performance wireless communication system. While a number of air-lifted components have been demonstrated using several types of micromachining technologies, a universal low cost and high efficiency technology enable the integration of airlifted RF components is highly desired. From the standpoint of system-on-package (SOP) integration, these 3-D RF passive components are needed to be fabricated in a one-step process on the same substrate.

In addition to wireless communication systems, another very important application of RF system-on-package technologies is the wireless sensor. Wireless sensors, translating nonelectrical input signals into wirelessly-detectable RF information, have become more and more ubiquitous in our daily life. While wireless pressure sensors have been widely commercially available in the automobile market, the recent applications of wireless sensor have been expanded into almost every area. There is a growing interest of combining micromachined sensing structures and microelectronic building blocks on a single chip [38]. Compared with wireless communication system, it becomes even more challenging to integrate not only the RF components, but also the mechanical sensing structures (such as MEMS membrane or cantilever) on the same

substrate. Figure 1.6 shows a concept of the SOP integration of 3-D components including both resonators and sensor elements. The 3-D RF components usually have different size and geometry due to the different air-lifting mechanisms, and the sensor elements have micrometer or millimeter scale mechanical structures. This thesis aims at the development of a new micromachining technology that enables such an RF SOP integration for not only the air-lifted components but also for micromachined mechanical sensing elements.

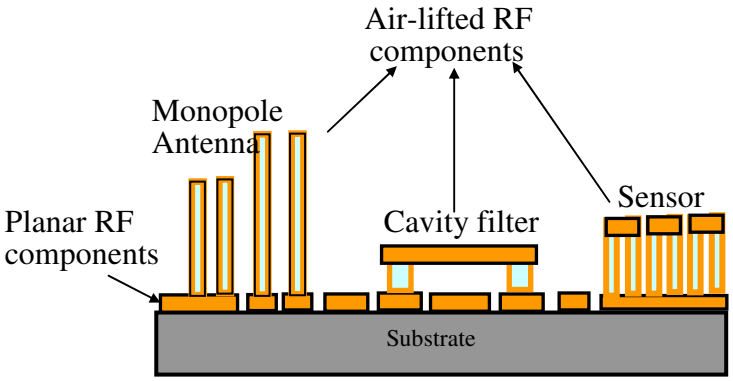

Figure 1.6 concept integration of air-lifted RF components of different functionalities and geometries on the same substrate

1.3 Dissertation Outline

This dissertation can be divided into two parts. The first part (Chapter 2 and Chapter 3) is concentrated on the development of the fabrication technology, and the second part (Chapter 4 and Chapter 5) is focused on the new RF component design and characterization.

Chapter 2 introduces and reviews the polymer-core concept for 3-D RF components, which is a basis for the fabrication technologies in this dissertation. As they

are very commonly reported polymer-core fabrication technologies, stereolithography and SU-8 micromachining are briefly reviewed in both advantages and disadvantages. In order to further demonstrate the main limitations of current fabrication technologies for polymer-core RF components, a fabrication example based on SU-8 micromachining is discussed in detail, and the main challenges are summarized.

Chapter 3 aims at an all-in-one solution to the challenges proposed in Chapter 2. First, the fact that molding technology can be an excellent candidate for 3-D RF components fabrication and integration is demonstrated. Then a metal-transfer mechanism is introduced into the conventional micromolding process, creating a one-step fabrication technique for both the polymer-core and metal-pattern. The proposed metal-transfer-molding (MTM) technique is further characterized in several aspects, such as fabrication limitations and process parameter optimization. Finally the established MTM process is compared with other micromachining technologies, and attractive applications for this technology are proposed.

Chapter 4 presents the design, fabrication and characterization of several novel 3-D RF components based on MTM technology. These 3-D components are especially designed to demonstrate the air-lifting mechanisms, including air-gap CPW transmission line (elevated air-lifting), quarter wavelength monopole antenna (vertical air-lifting), and evanescent-mode cavity resonator (extruded air-lifting). These 3-D components are usually very difficult to fabricate by other micromachining technologies such as SU-8 fabrication, but benefit greatly from the simplicity of MTM process. The measurement results show excellent agreement with simulation and a greatly improved performance over planar device counterparts.

In order to demonstrate the great potential of the MTM technique in future wireless applications, Chapter 5 presents a novel airflow sensor design integrating both the 3-D RF components and mechanical sensing structures. The proposed sensor includes a reduced-size RF cavity resonator, CPW to cavity transition, and sensing diaphragm/beam structure. It first demonstrates a sensing mechanism based on evanescent electro-magnetic fields, and presents a simplified equivalent circuit model for the sensitivity analysis. It then presents a simple CPW-to-cavity transition method enabling ease of integration. The measurement result shows an excellent sensitivity of the resonant frequency to the sensing beam deviation. The second part of Chapter 5 further introduces a wireless interrogation method for the sensor applications. By integrating ultra-wide-bandwidth (UWB) antennas, the resonance of the cavity resonator can be wirelessly detected. Two wireless interrogation mechanisms have been demonstrated without any help of external amplifier or active circuits for the passive sensor design.

Chapter 6 presents the conclusion and future outlook of this work. The overview of this dissertation work is shown in Figure 1.7.

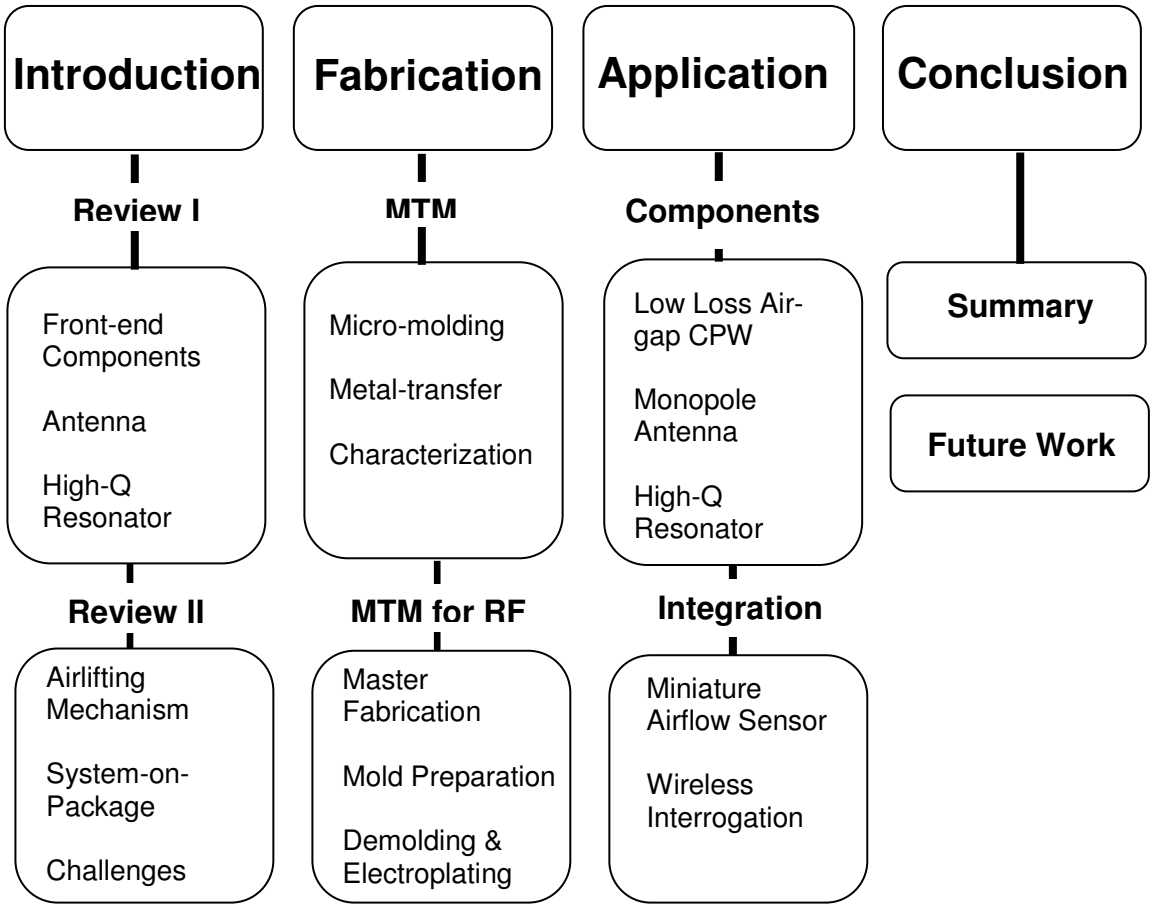

Figure 1.7 Overview of dissertation work

Chapter 2

Review of Micromachined RF Front-end Components

Planar RF passive components suffer from substrate dielectric loss, mutual coupling with their substrate, and surface wave perturbation issues. These problems become more predominant when the frequency is in millimeter wave range. One potential solution is introducing 3-D RF passive components by micromachining technologies. In the past decades, a series of new solid freeform fabrication techniques have emerged to realize three-dimensional (3-D) structures in the micro-scale. These 3-D micromachining techniques have the potential to become an enabling technology for the next-generation compact and high quality-factor RF components replacing older MEMS technologies, such as plate-through-mold [39], silicon micromachining [31], and LIGA processing [40]. Among all these techniques, the polymer-core technology has been recently successfully demonstrated for RF components fabrication [27-30]. It has many advantages such as low cost and high performance.

2.1 Polymer-Core Conductor Technology

As is shown in Figure 2.1, considering the fabrication approach for a high-aspect-ratio post conductor, conventional via filling by electroplating is very challenging while coating of metal over a polymer column is much easier. The metal coatings can be simply electroplated from several microns to tens of microns depending on the desired current density for the specific applications.

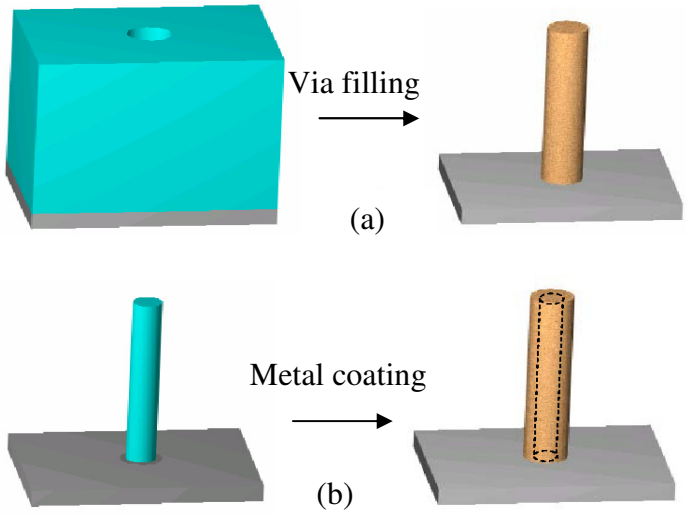

Figure 2.1 Approaches for vertical conductor: (a) solid conductor (b) polymer-core conductor

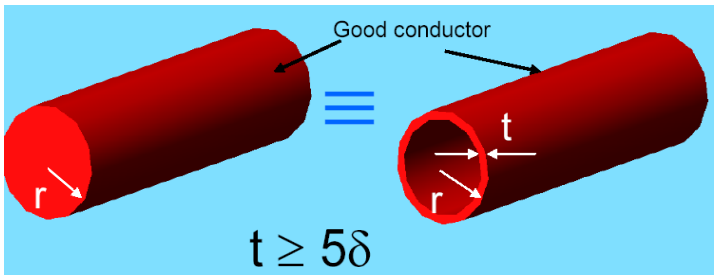

Figure 2.2 Solid conductor vs. hollow conductor in high frequency [21]

It is well known that as frequency increases, an electromagnetic wave propagating through a good conductor attenuates very quickly in the depth direction of the conductor and the resultant electric current flows through the outermost portion of the conductor. A 3-D RF component could be fabricated much more efficiently using a hollow shaped conductor with a polymer core, especially as operation frequencies increase.

The current density J in an infinitely thick plane conductor decreases exponentially with depth d from the surface, as follows [41]:

$$J = J_s e^{-d/\delta} \tag{2.1}$$

where δ is a constant called the *skin depth*. This is defined as the depth below the surface of the conductor at which the current density decays to 1/e (about 0.37) of the current density at the surface (J_S). It can be calculated as follows [41]:

$$\delta = \sqrt{\frac{2\rho}{\omega\mu}} \tag{2.2}$$

A hollow conductor whose conductor thickness is greater than five skin depths is considered electrically equivalent to the solid conductor, where outer diameters of both conductors are the same, as in Figure 2.2 [21]. For example, the skin depth of copper and gold at 30GHz and 100GHz is listed the Table 2.1. For a polymer pillar with a copper coating more than 2μm, an RF signal of 30GHz or higher frequency can be conducted without any additional loss when compared with a solid conductor. The 2μm copper coating can be easily fabricated by electroplating on a thin seed layer. The polymer-core components with electrical functionalities comprise three parts: (1) a polymer-core backbone structure; (2) metal conductor coating and (3) interconnects. The polymer-core provides a backbone structure; the metal coating conducts the current or electro-magnetic waves, and interconnects provide the input/output as well as the connection of all the conductors.

Table 2.1 Skin Depth of Copper and Gold at 30 and 100GHz

	30 GHz	100 GHz
Cu	0.38 μ m	0.20 μ m
Au	0.45 μm	0.25 μ m

Metallization quality, especially surface roughness, is very important for polymer-core RF components because the RF signal is conducted by the metal layer. The metallization quality can be characterized by the metal-polymer adhesion and surface roughness.

Poor adhesion between the metal coating layer and polymer-core leads to metal de-lamination, which, if this progresses to metal cracking, generates RF impedance change or even discontinuity.

The surface roughness of the metal coating affects the performance such as quality factor or conduction loss. The metal conduction loss from the plated surface roughness can be quantified by an equivalent effective conductivity (σ_{eff}), which is inversely proportional to the effective surface area of the conductor as following [42]:

$$\sigma_{eff} = (\frac{S}{S + \Delta S})\sigma \qquad (2.3)$$

The power loss increases with the decrease in the conductivity by the equation [41]:

$$P_{loss} = \frac{1}{2}\left(\sqrt{\frac{\pi f \mu}{\sigma_{eff}}}\right)\int_s |J_s|^2 ds \qquad (2.4)$$

where S is the surface area, ΔS represents the additional surface area due to roughness and σ is the ideal conductivity value of the plated metal. While the copper plating roughness can be minimized to tens of nanometers by optimizing the plating process [42], the surface roughness of the polymer-core component is mainly determined by the polymer structure surface. The performance of the RF components is highly affected by the surface roughness. For example, due to a 2μm surface roughness, the effective surface area of a cavity is expanded by about 17%, and the unloaded quality factor of the cavity decreases to 85% of the ideal model.

Based on the above discussion, high metallization quality is required for polymer-core RF components to achieve the desired performance. A series of 3-D polymer-core RF components have been reported recently using stereolithography and SU-8 surface micromachining. By using the polymer-core conductor combining epoxy backbone patterning with subsequent metallization, passive RF components such as antennas, couplers, inductors, etc, have been successfully demonstrated.

2.2 Polymer-Core RF Components by Stereolithography

Stereolithography is a fast, maskless, and layer-by-layer additive process capable of building truly 3-D, high aspect-ratio, and lightweight microscale and mesoscale structures. The automatic vertical building-up of distinct two-dimensional layers precludes the use

of mask-based fabrication methods. These unique properties have made stereolithography promising for truly 3-D and highly integrated RF and microwave components.

As is shown in Figure 2.3, stereolithography creates a three-dimensional part by scanning a laser beam on a liquid monomer and laser curing it into polymer (photo-polymerization) in a line-by-line and layer-by-layer sequence. The layer-by-layer polymer fabrication creates truly three-dimensional structures and vertically integrated structures in one piece. The structure model is created in CAD software such as AutoCAD, and the structure is 'sliced' into layers of 25μm thick with high resolution.

The fabrication tolerance analysis of the polymer stereolithgraphy has been studies in detail and the fabrication tolerances have been found to be 0.187% [43]. The stereolithography technique enables the fabrication of high-Q RF components such as narrow-band filters, and the ability to design in three dimensions makes the design and fabrication of vertically integrated high- RF components feasible.

Figure 2.4 demonstrates an example of a vertically integrated helix antenna and filter front-end module by stereolithography [44]. This Figure illustrates the 3-D monolithic packaging capability of this process to integrate large voids, such as filter cavities, and nontraditional 3-D shapes, such as a freestanding helix antenna.

However, stereolithography for non-prototype production of next-generation RF/microwave components is challenged by its serial fabrication nature, lack of RF-applicable material options, and metallization difficulties. It usually takes several hours to fabricate one batch of the devices due to the laser scanning speed. The materials options are limited to only several types of commercially available SLA resin and are also very expensive. The thickness of each scan layer is 25μm or more, leading to

considerable surface roughness which degrades the RF performance such as the quality factor.

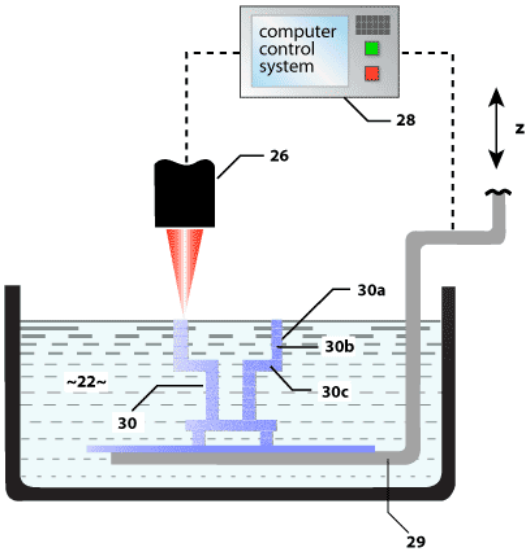

Figure 2.3 Experimental schematic of stereolithography process

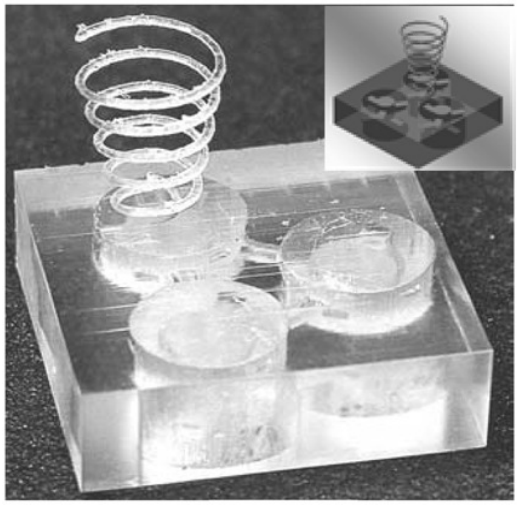

Figure 2.4 Spiral antenna made by stereolithography [44]

Furthermore, stereolithography is only a fabrication method for polymer backbone structures, and cannot concurrently pattern interconnects on the structure, so the fabricated components can only be connected manually with other components or active circuits. As a result, stereolithography is suitable for components prototyping or small quantity production, but is less studied to the the manufacturing of large numbers of RF components.

2.3 Polymer-Core RF Components by SU-8 Micromachining

SU-8 micromachinging technology has been widely used in various MEMS applications. SU-8 (Microchem, Inc.) [45], a negative tone photodefinable epoxy, is known to give a very good sidewall profile with UV lithography and is currently the primary material to make polymer-core structures.

Table 2.2 Summary of Reported SU-8 Air-lifted RF Components

Component	Frequency	Height Profile	Performance Improvement
Microstrip Line	5-50GHz	7μm, 10μm	Low loss and low dispersion
Monopole Antenna	76-95GHz	800μm	Better bandwidth
Yagi-Uda Antenna	25GHz	800,715, 560μm	Better bandwidth, higher gain
Patch Antenna	25GHz	600μm	Better bandwidth, higher gain
Microstrip Coupler	15-45GHz	200μm	Broad bandwidth, higher efficiency
Resonator	30GHz	300μm	Higher Q (219)

By using the SU-8 polymer-core conductors, a series of passive RF components such as antennas, couplers, inductors, etc, have been successfully demonstrated [27-30]. The geometry and performance improvement of the reported SU-8 polymer-core RF components are listed in Table 2.2. SU-8 micromachining is compatible with CMOS processes, and relatively easy to fabricate high-aspect-radio (up to 10:1) structures. Recent development of SU-8 micromachining technologies such as inclined exposure technology and multi-layer processing enable some truly 3-D micro structures [46，47].

The fabrication process for SU-8 polymer-core RF components generally includes backbone structure fabrication, sacrificial layer patterning, and metal coating followed by sacrificial layer removal. The most challenging is the accurate metallization of both the 3-D components and interconnects. Coplanar waveguide (CPW) is usually utilized as interconnect of polymer-core RF components. CPW is composed of a center conductor and two ground conductors. The slots between the conductors are usually tens of microns. On the other hand, the 3-D RF components are hundreds of microns. So an accurate metallization of both the 3-D components and interconnects is required in order to achieve the desired performance.

However, most reported work in SU-8 micromachined RF components focuses on the component design and characterization, and there is less discussion regarding process limitations for low-cost and reliable fabrication. In this chapter, an example of a micromachined SU-8 polymer-core conductor array is proposed and discussed. The process limitations for this structure are demonstrated in detail.

The proposed design of a micromachined SU-8 polymer-core conductor array is shown in Figure 2.5. Each device has 100 pillars as electrodes, and each pillar is 100μm

in diameter and 700μm high. The center-to-center distance of the pillars is 280μm, therefore the distance between adjacent pillars is 180μm. The pillars and the substrate are made from the same material thus improving the mechanical strength. The pillars are interconnected so as to form a 'checkerboard' potential pattern. Adjacent pillars in a row or column have opposing electric potential. The proposed structure is a typical polymer-core micromachined component with polymer backbone, metal conductor coating and interconnect.

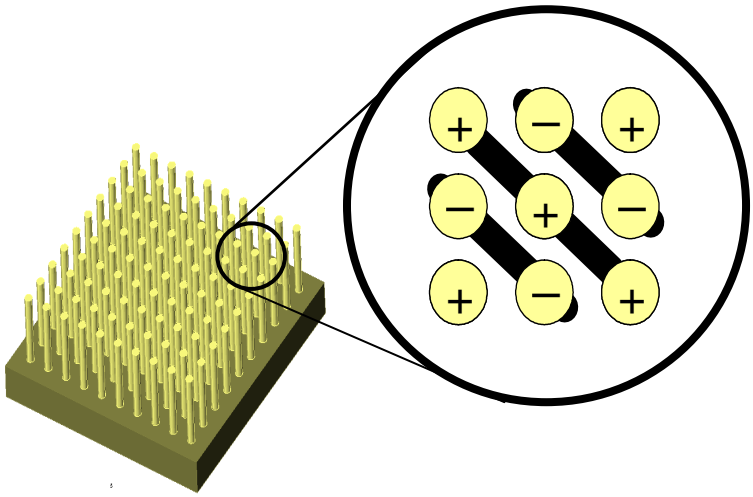

Figure 2.5 Schematic of a checkerboard pattern of polymer-core conductor array

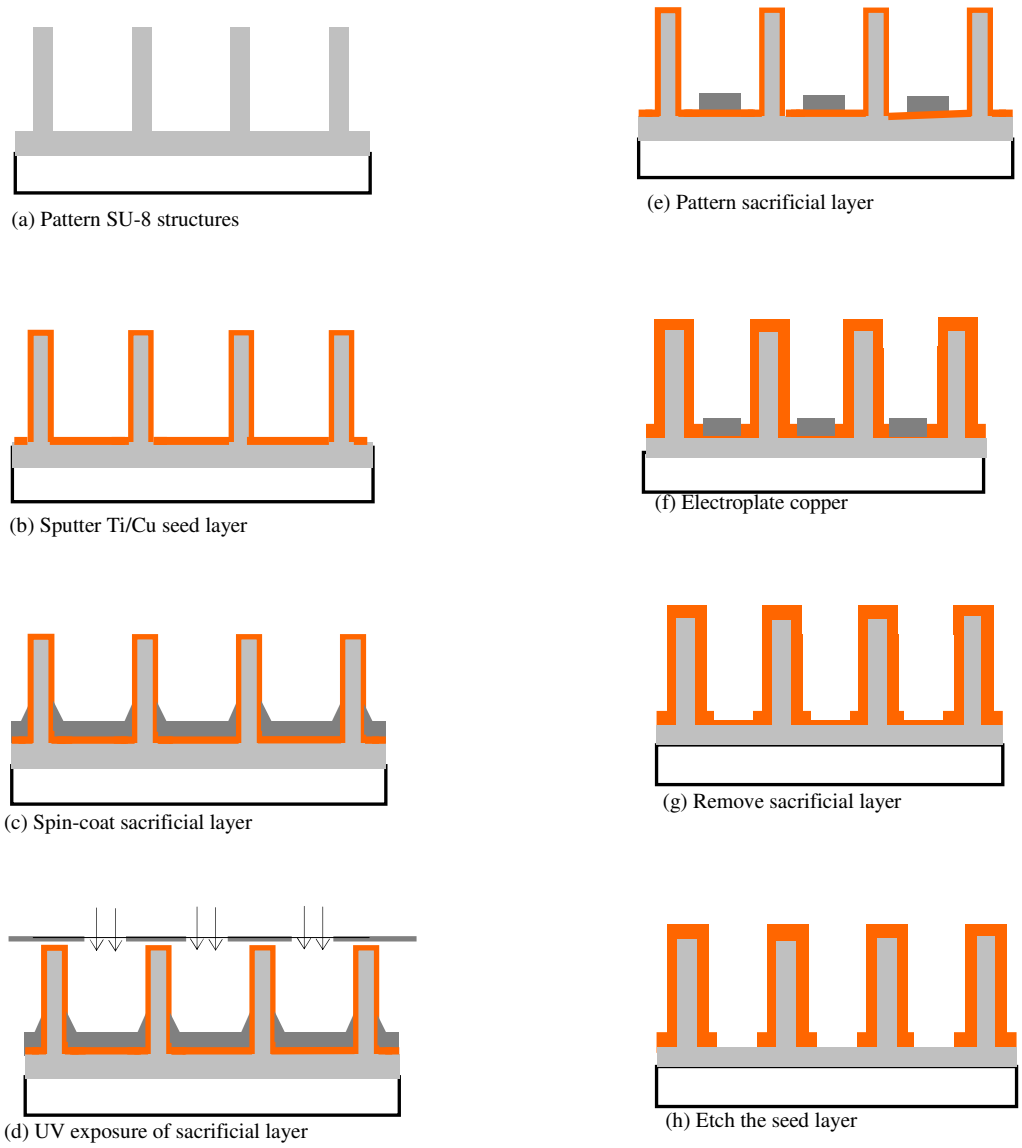

Figure 2.6 Fabrication process of polymer-core electrode array by SU-8 micromachining

The fabrication of the polymer backbone is based on SU-8 micromachining and is shown in Figure 2.6. First, an approximately 1mm thick layer of SU-8 is spin-coated on a transparent glass substrate. After soft baking, the SU-8 is exposed from the front in order to form the 700μm high pillar array and the rectangular walls (a). Because the high-

aspect-radio SU-8 structure has relatively poor adhesion to the substrate and is very easy to delaminate [48], the SU-8 is weakly blanket-exposed from the back, i.e., through the glass substrate, to form the 300μm thick substrate of the pillar array (a). The exposure is followed by a post-exposure bake to cross-link the SU-8 structure. After developing, a Ti/Cu (30nm/200nm) layer is sputtered to cover the whole structure as a seed layer (b). An O_2 plasma treatment is usually needed to improve the surface adhesion of the SU-8 structures before the seed layer deposition. Then an additional thin SU-8 layer (10-20μm thick SU-8 2005) is spin coated on the device (c). After soft baking, the thin SU-8 layer is exposed to form an electroplating mold (d). The exposure here is proximity mode, because the mask is separated approximately 700μm from the resist. After post baking and developing (e), a 10μm thick metal coating is electroplated into the mold to cover and interconnect the pillars (f). Then, the SU-8 electroplating mold is removed by reactive-ion-etching (RIE) (g), and the seed layer Cu/Ti is etched in a selective copper etch (NH_3OH saturated by $CuSO_4$-$5H_2O$) and 10% HF respectively (h).

Figure 2.7 shows the fabricated polymer-core conductor array, and Figure 2.8 shows a measured current curve to demonstrate that it can successfully conduct a transient current up to 0.5A.

However, the fabrication of this polymer-core electrodes array is relatively complicated. There are at least eight steps of processes including one step of high-aspect-ratio lithography, one step of proximity photolithography of the sacrificial layer, one step of thin film sputtering, one step of electroplating, and a developing process and an RIE etching process. The process window is narrow because of the number of processes and the challenges of several critical steps. In particular the processes from 2.7(d) to 2.7(f) are

for the selective metallization and have narrow windows. To successfully fabricate such structures, the whole process had been developed and optimized for more than three months, and the yield is still relatively low.

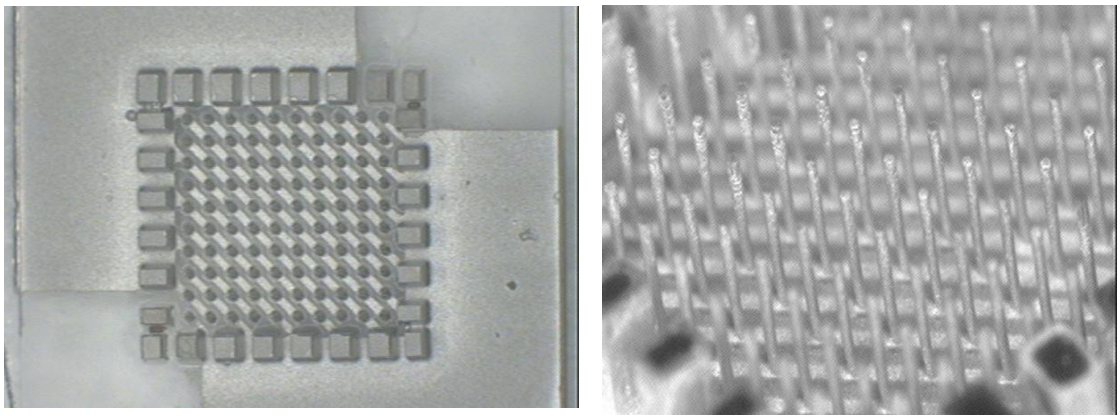

Figure 2.7 Fabricated polymer-core conductor array by SU-8 micromachining

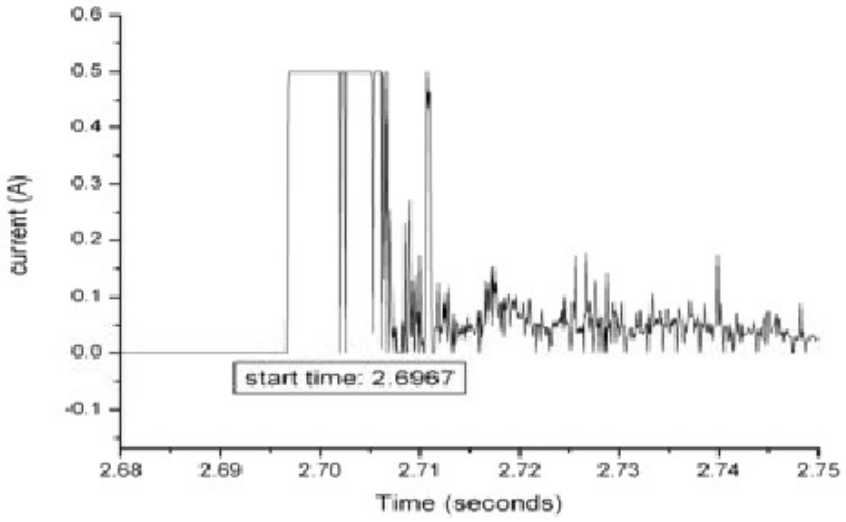

Figure 2.8 Measured transient current by the polymer-core MEA

The fabrication of polymer-core RF components has even much higher requirements than the micro-electrode-array, because a small fabrication defect may not change the resistivity for DC current, but could generate a large RF impedance change.

In summary, there are several challenges for the SU-8 fabrication of polymer-core technology. First, the adhesion between the SU-8 backbone structure and the common RF substrates such as silicon wafer, quartz, LCP, and glass is usually very poor [48], especially for the high aspect- ratio structures; second, the metal patterning is usually accomplished by patterning a sacrificial layer by proximity photolithography, such as the process in Figure 2.7(d). Because of the surface tension of the sacrificial layer and the optical diffraction of proximity photolithography, a discontinuity of the polymer-core conductors often occurs as reported in Figure 2.9 [49].

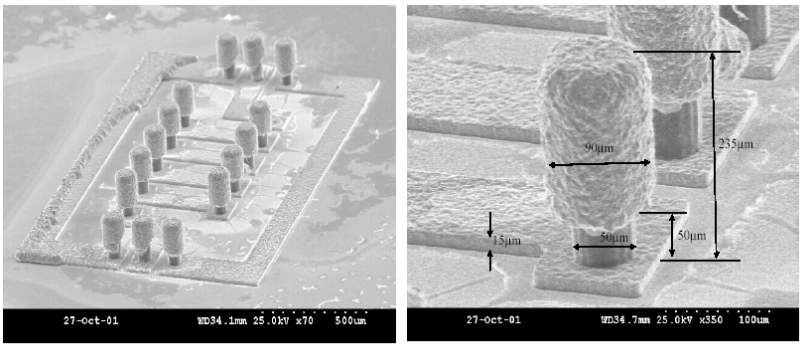

(c) (d)

Figure 2.9 Discontinuity of polymer-core structures due to sacrificial layer [34]

Furthermore, in system-on-package (SOP) integration, multifunctional RF components are required to be implemented on a single substrate and package to realize the promise of a low-cost, low-loss, and miniaturized microwave front-end module. However, these air-lifted RF components usually have very different geometries and

aspect ratios from each other. For example, Table 2.2 shows a summary of the geometry of the reported air-lifted RF components. Monopole antennas are as high as a quarter wavelength (nearly 1mm in W-band), while an air-lifted coupler is usually at a height of less than two hundred microns. It is very challenging to fabricate these 3-D structures with different height on the same substrate by SU-8 micromachining.

Most important, the cost is always the first consideration for personal wireless applications. Compared with planar RF components, although these air-lifted components have superior advantages such as low substrate loss and high quality factors, the fabrication cost of these air-lifted components is considerably higher because of the multiple lithography, deposition, and etching steps. Therefore, it is highly desirable to develop a simple low-cost fabrication technique for the fabrication and integration of air-lifted RF components with comparable cost to printed components.

Chapter 3

Metal-Transfer-Molding (MTM) Development

Planar RF components are usually fabricated by screen printing or etching, which is very simple and low-cost. However, for 3-D RF components, fabrication technologies based on SU-8 surface micromachinin, silicon etching or stereolithography have been utilized, and have higher cost. Micromolding, a widely utilized 3-D manufacturing technology, is a very promising candidate for the polymer-core components that can simultaneously achieve high performance and low cost.

3.1 Molding Technology of 3-D Polymer Structures

The micromolding of thermoplastic polymers is possibly the cheapest manufacturing technology for non-electronic micro devices. The fabrication costs of molded micro parts are typically mostly independent of the complexity of the design. For many kinds of three-dimensional (3-D) microstructures, it is usually challenging to make the initial versions of these structures using standard micromachining techniques in high yield. However, once the mold master has been made, thousands of replicas can be molded with relatively little effort. The cost of the raw material in most cases is negligibly low, because only small material quantities are required for micro components. Therefore, parts fabricated by micromolding, even from high-end materials, can be suitable for applications requiring low-cost and disposable components.

Thermoplastic materials are a very large material class, which allows one to find a suitable polymer for many diverse applications. There are polymers that are stable at temperatures as high as 250 ^{o}C (e.g., polyetheretherketone, PEEK) and others that resist aggressive chemicals such as alkaline solutions, acids, and solvents (e.g., perfluoralkoxy, PFA). Polymers are electrical and thermal insulators, but when filled with appropriate powders they can be used as electrical conductors, heat sinks, and even magnets. Molded micro-structures can be either soft and elastic such as polyoxymethylene (POM) or hard and brittle such as polysulfone (PSU). They are available from optically transparent materials such as cycloolefin copolymer (COC) and opaque ones such as polyamide (PA) filled with graphite. Polymers such as PVDF even exhibit a piezo-electric effect.

Therefore, micromolding of thermoplastic polymers, or reaction-injection molding of thermosetting polymers, is a very promising fabrication technique of micro components for commercial applications. The development of micromolding spans more than 30 years, and much experience and knowledge has been accumulated. Molding machines and materials are commercially available and routinely used in industry every day.

Micromolding techniques are widely utilized in many areas, such as most CD and DVD data storage, optical components such as micro-lenses [50], waveguides [51], optical gratings [52], and photonic structures [53]. There are also a variety of molded micro-fluidic devices by using PDMS micromolding, such as pumps [54], valves [55], capillary analysis systems [56], flow sensors [57], and many lab-on-a-chip applications. Molding technology has been widely used in microelectronics packaging to physically protect integrated circuits and increase the long-term reliability of electronics [58, 59].

Recently molding technology has also been utilized for the transfer of desired geometries into a thin resist layer on a silicon wafer to replace traditional photolithography [60].

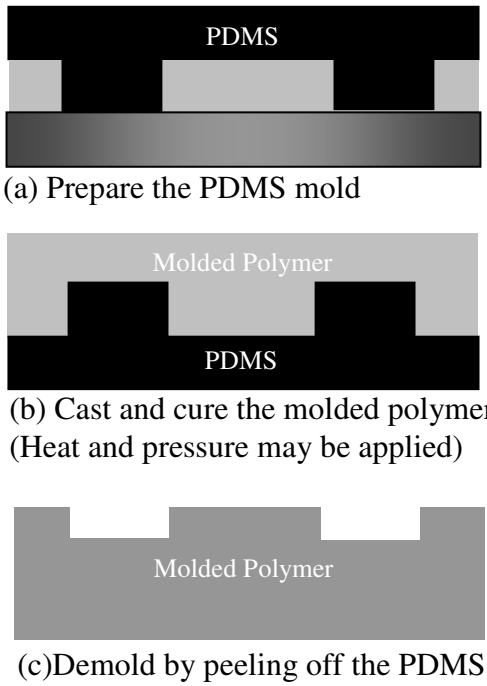

Figure 3.1 Micromolding process by using PDMS mold

Usually, most problems in micromolding occur during demolding. During the demolding process, micro-structures may be torn apart, deformed, or destroyed. In particular, when there are high-aspect-ratio structures, the demolding process becomes more difficult. One of the methods to solve this problem is to use poly(dimethylsiloxane) (PDMS) as the mold material. PDMS is a widely used material in soft-lithography, such as molding, embossing, and transfer printing [61, 62]. It has several unique advantages suitable for the molding process. For example, PDMS is an elastomer material so that it can be easily peeled from the molded structures. PDMS also has an extremely low

surface energy (19.7mJ/cm^2), so the adhesion between the PDMS mold and the molded polymer materials is very low. Figure 3.1 shows the general process of micromolding by using a PDMS mold. First a mask structure is made by photolithography, and then the PDMS mold is prepared by casting and cure the pre-polymer. The molding polymer is cast in the PDMS mold. After the curing, the PDMS mold is peeled off.

Because of the unique properties of the PDMS mold, various micro-structures can be easily molded using the PDMS mold. Several examples are shown in Figure 3.2, such as high-aspect-ratio needle structures (Figure 3.2a) [63], multi-layer structures (Figure 3.2b) [64], or re-entrant microstructures (Figure 3.2c). The molded structures by PDMS have a high fidelity to the master structures, such as the structure dimension and surface roughness. Moreover, the PDMS mold usually can be re-used in subsequent molding process.

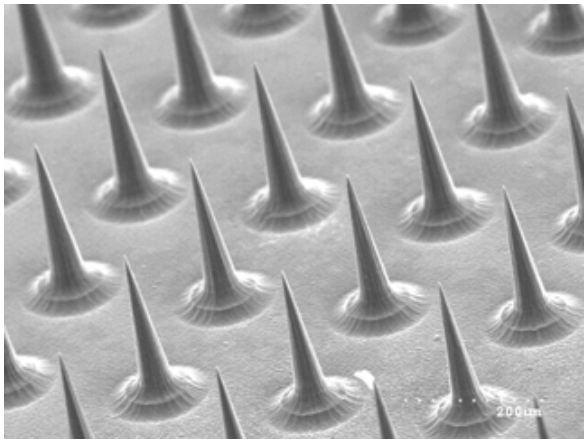

(a) Molded micro needles by PMMA ([63])

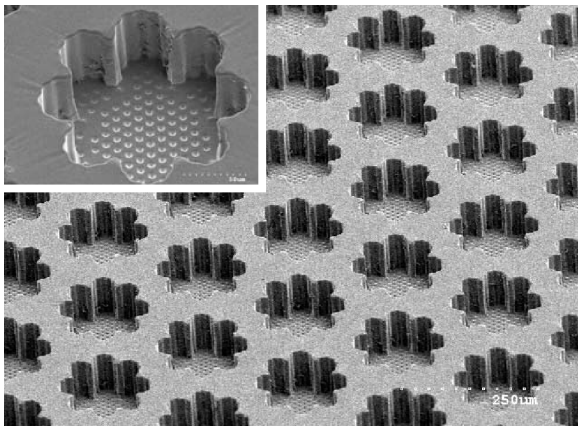

(b) Molded micro structures on PU cell substrate ([64])

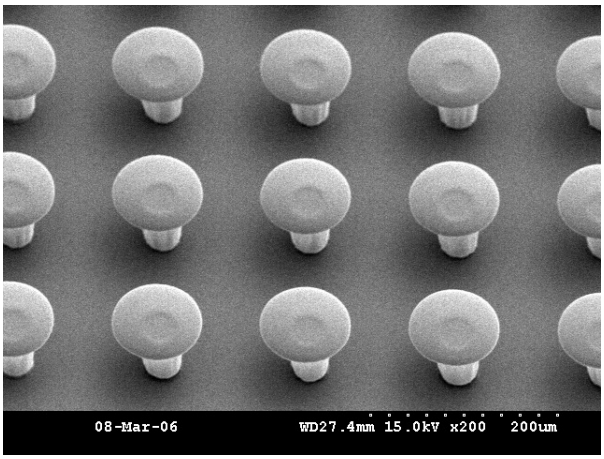

(c) Molded re-entrant structures by SLA resin

Figure 3.2 Molded examples by PDMS micromolding

3.2 Metal Transfer in Molding Process

Because of these unique advantages, molding technology has great potential for the fabrication of polymer-core RF components. Compared with SU-8 micromachining, a micromolding process has greatly reduced cost, and many more material choices with desirable dielectric, mechanical, and thermal properties. However, current molding technology is mostly utilized in manufacturing of non-electrical devices. A main reason

may be the difficulties in accurate metallization for the molded components. In particular, when the molded components contain substantial three-dimensionality, standard metal coating and patterning techniques such as photolithography, etching, and lift-off may become challenging. In this work we examine the possible approaches to accurate metallization of molded 3-D polymer structures.

Techniques for two-dimensional (2-D) metal patterning on inorganic substrates are usually photolithography, lift-off, or etching, while for the metal patterning on organic substrates such as polymers or epoxies, lithographic techniques based on printing are potential candidates for unusual applications in plastic electronics, biotechnology, and other fields because they avoid many limitations of conventional methods. They also require only simple, low-cost tools (i.e., molds, stamps, and presses).

Several printing approaches have been recently demonstrated for patterning metal electrodes for organic electronic components; these include nanotransfer printing (nTP) [65, 66], soft contact lamination [67], cold welding [68], cathode transfer [69], and thermal imaging [70]. Compared with other printing methods, when applied with soft, elastomeric stamps, nTP can be performed without the high pressures that are required with stamps made of rigid materials; In addition, it has been demonstrated that noncovalent surface forces can be sufficiently large to perform nTP [71].

Figure 3.3 schematically illustrates the steps for noncovalent nTP. The first step is coating a stamp of poly(dimethylsiloxane) (PDMS) with a thin metal film. Placing this metal-coated stamp onto a flat, smooth substrate leads to “wetting”, which provides intimate contact between the two surfaces without the need to apply external pressure. Mild heating 50–80 °C for a sufficient time, followed by removal of the stamp, leaves a

metal pattern in the geometry of the relief features on the substrate. The edge roughness of the features in both cases is 10–30 nm. The transfer mechanism is based simply on the different strengths of nonspecific adhesion between the PDMS-metal and substrate-metal interfaces.

There is no specific covalent chemical interaction between the materials used for printing and either the stamps or the substrates. The nTP technique has been exploited in applications of organic microelectonics [71]. However, metal pattern transfer based on nTP has been demonstrated only on relatively planar substrates and has been limited to 2-D patterns. In many MEMS applications, such as micro electrode arrays (MEA), there are needs for 3-D selective metallization. In this work, the same metal transfer mechanism is introduced to the conventional molding process, and a simple selective metallization technique is presented.

As shown in Figure 3.3, after the transfer printing process, the metal film on the raised region of the PDMS stamp is printed onto a substrate; meanwhile, the metal film left on the PDMS stamp is actually patterned as well, and only the recessed region and the side walls are coated by metal film. So the remaining metal film in the PDMS is 'pre-patterned' by the nTP process, and has a 3-D structure. This patterned metal film can be also transferred to the molded polymers based on the same mechanism, i.e., differing strengths of nonspecific adhesion between the PDMS-metal and polymer-metal interfaces. For most materials, the adhesion strength of the PDMS interface is weaker than that of the metal/cast polymer interface, primarily because of the extremely low surface energy (19.8 mJ/m^2) of the PDMS. Table 3.1 shows the surface energies of some common polymers [72]. Most common polymers have higher surface energies than PDMS.

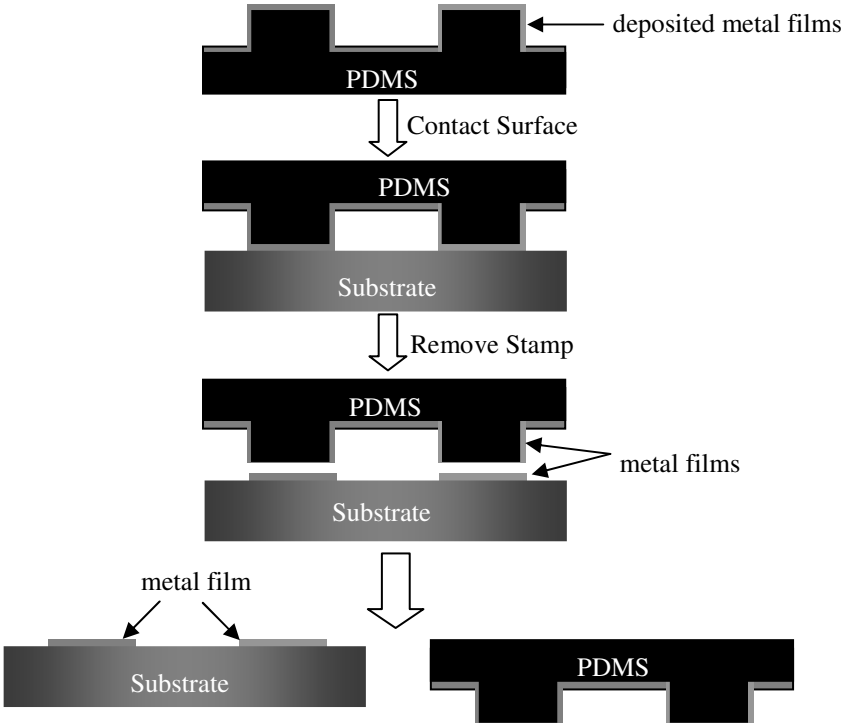

Figure 3.3 Process flow of nano transfer printing (nTP)

Table 3.1 Surface Energies of Some Common Polymers

Polymer Name	Surface Energy at 20 °C (mJ/m^2)
Polyethylene-linear PE	35.7
Polyethylene-branched PE	35.3
Polypropylene-isotactic PP	30.1
Polyisobutylene PIB	33.6
Polystyrene PS	40.7
Poly-a-methyl styrene PMS (Polyvinyltoluene PVT)	39.0
Polyvinyl fluoride PVF	36.7
Polyvinylidene fluoride PVDF	30.3
Polytrifluoroethylene P3FEt/PTrFE	23.9
Polytetrafluoroethylene PTFE (Teflon™)	20.0
Polyvinylchloride PVC	41.5
Polyvinylidene chloride PVDC	45.0

Polychlorotrifluoroethylene PCTrFE	30.9
Polyvinylacetate PVA	36.5
Polymethylacrylate (Polymethacrylic acid) PMAA	41.0
Polyethylacrylate PEA	37.0
Polyethylmethacrylate PEMA	35.9
Polybutylmethacrylate PBMA	31.2
Polyisobutylmethacrylate PIBMA	30.9
Poly(t-butylmethacrylate) PtBMA	30.4
Polyhexylmethacrylate PHMA	30.0
Polyethyleneoxide PEO	42.9
Polytetramethylene oxide PTME	31.9
Polyethyleneterephthalate PET	44.6
Polyamide-6,6 PA-66	46.5
Polyamide-12 PA-12	40.7
Polydimethylsiloxane PDMS	**19.8**
Polycarbonate PC	34.2
Polyetheretherketone PEEK	42.1

Figure 3.4 schematically illustrates the fabrication steps of the proposed 3-D metal pattern transferring process. A PDMS stamp is created by casting and curing Sylgard-184 prepolymer against a silicon master patterned by conventional photolithography and etching. Then, the PDMS stamp is coated with a thin metal film (usually Au/Ti), which covers not only the raised and recessed regions of the stamp mold but also the sidewalls (a). A transfer printing process is performed to remove the metal film on the raised regions of the stamp mold. In this process, the freshly metal-coated stamp mold is immediately placed onto a flat, smooth substrate of relatively high surface energy compared with PDMS (b). The substrate typically used is a polyester tape or silicon tape. However, our interest is the original PDMS stamp with metal film coated on the recessed region. An appropriate structural polymer in a liquid state (e.g., uncured, melted or with solvent) is cast onto the PDMS stamp mold. Vacuum and heat may be

utilized to ensure that the liquid-state polymer fully wets the recessed regions of the stamp mold (d). After the cast polymer is solidified, the PDMS stamp mold is peeled off and the metal film within the recessed region is completely transferred to the molded structures (e).

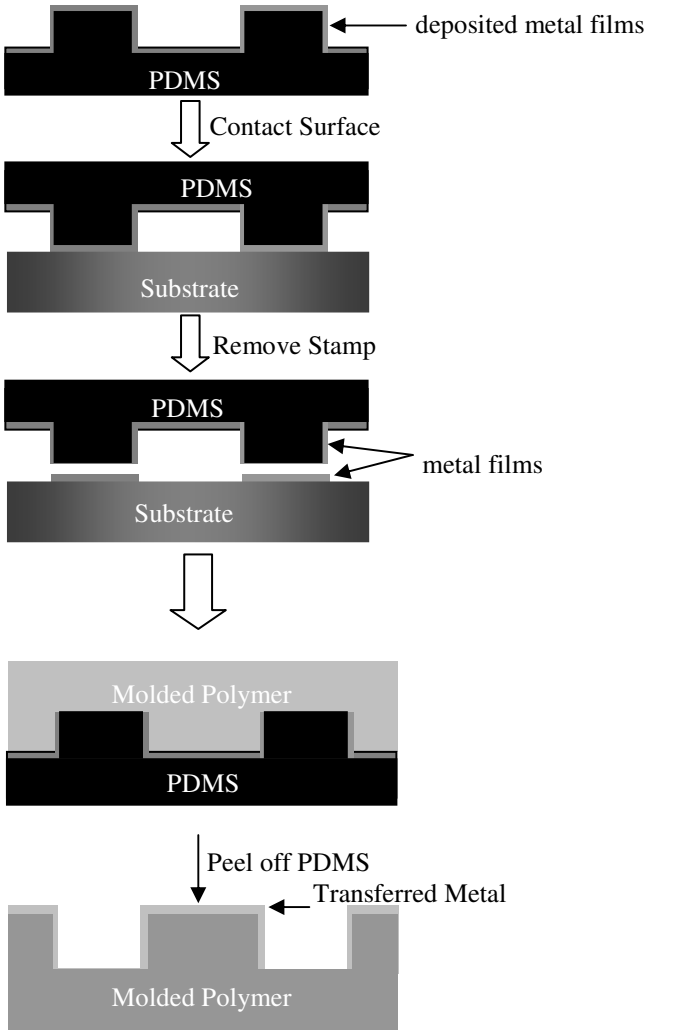

Figure 3.4 Process flow of metal-transfer-molding (MTM)

Figure 3.5 displays a series of microscope pictures of the metal-transfer-molding process. Figure 3.5(a) shows a PDMS mold with metal coating by DC sputtering, and 3.5(b) shows the removed metal pattern on a polyester tape surface. 3.5(c) shows the PDMS mold with pre-patterned metal layer, and Figure 3.5(d) shows the final molded PU structures with selective metallized surfaces.

To demonstrate the capabilities of MTM for different scales and structures, a series of experiments have been performed. Figure 3.6 displays a set of SEM and microscope images of several types of 3-D structures with some representative scale features made of various polymers. The dimensions range from 2 μm to 100 μm, and the aspect ratio defined as width to height is approximately 1:1. The extruded 3-D structures are coated by transferred metal, while there is no metal observed on the bottom substrate because of the pre-patterning by nTP.

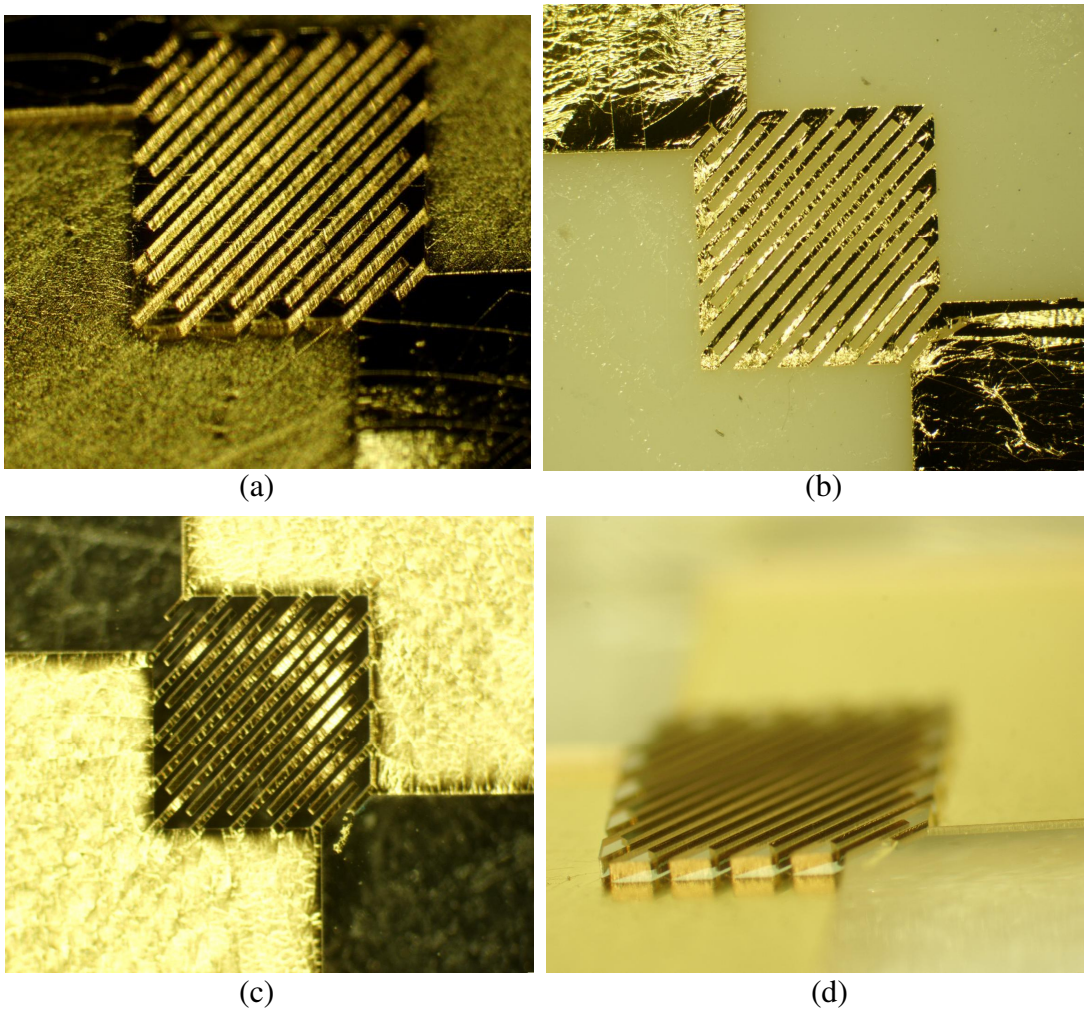

Figure 3.5 Microscope pictures of a MTM process example (a) PDMS mold with metal coating (b) removed metal pattern by polyester tape (c) pre-patterned metal film on the PDMS mold (d) Metal transfer molded structures on PU

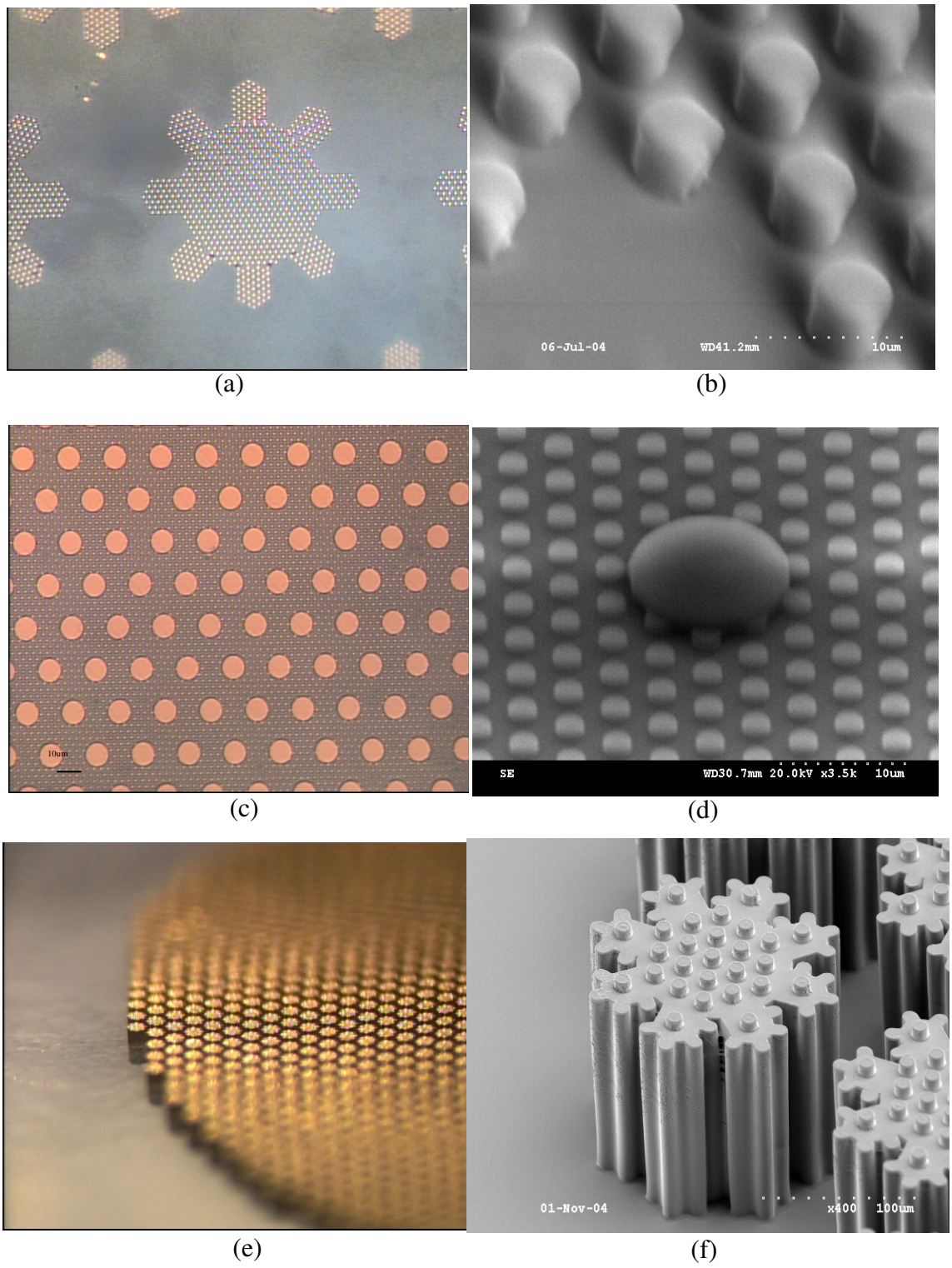

(a) (b)

(c) (d)

(e) (f)

Figure 3.6 Examples of different scales of metal transfer molding technique (a)(b) 2μm pillar array; (c)(d) 2μm and 10μm combined dimple array; (e)(f) high aspect ratio snowflake structures

3.3 Characterization of Metal Transfer

Several polymers that are widely used in replica molding have been utilized for the 3-D metal transfer demonstration: thermoplastic polymers such as polymethyl-methacrylate (PMMA), polyurethane (PU); biodegradable polymers such as poly(L-lactic acid) (PLLA); photo-curable polymers such as epoxy acrylate resin; and negative photo resists such as SU-8. Table 3.2 shows the molding recipes of these polymer materials. For these materials, the metal film (Au) is completely transferred from the PDMS to a control film of the same metal and the transferred gold film on the molded polymers shows similar adhesion strength with the directly deposited gold film based on the Scotch™ tape adhesion tests. The transferring of multilayer metal films is investigated in this molding process. In our tests, a 100nm thick Au film and a 30nm Ti film are deposited by DC sputtering or e-beam evaporation. The multilayer construction of the metal film (Au/Ti) yields films with better structural integrity, higher adhesion, and fewer cracking defects than the case of Au alone.

Table 3.2 Molding Recipes of Several Polymers

	Component	Vacuum	Heating	Curing time	UV treatment
PU	A:B-10:9	No	No	< 30min	No
PMMA	1	No	Yes (hotplate 50 ° C)	1 day-3 days	No
SLA	1	Yes	No	2 hrs	UV exposure >1000mJ
SU-8	1	No	Yes (hotplate 95 ° C)	>20hrs	UV exposure
PLLA	1	Yes	Yes (Oven 180 ° C)	1hr	No

To study the adhesion of metal transfer, a scotch tape test has been done for the transferred metal film on different materials. Commercially available scotch tapes such as Scotch Magic Tape, Scotch Blue Painter's Tape, and Scotch Masking Tape, are used for the tests. All the tapes have good adhesion and smooth adhesive surface to ensure a conformal and uniform contact with the tested surface. Before peeling off, the tapes are pressurized on the sample surface for 20min to ensure a conformal contact. The adhesion between transferred AU films with PMMA, SLA and SU-8 are investigated. The reported surface energy of these polymer materials are listed in table 3.3 [72-74].

Table 3.3 Surface Energy of Tested Polymer Materials

Polymer	SU-8	PU	PMMA	SLA Epoxy
Surface Energy	25-28mJ/m^2	43mJ/m^2	33-50mJ/m^2	35mJ/m^2

The scotch tape tests are performed for several polymer materials with transferred metal film in different thickness. The result is shown in Figure 3.8, SU-8 and PU have the best adhesion among the tested polymers, which is in accordance with the different surface energy for the materials.

For sputtered Au films under 100nm, more than 90% of the area of the Au film remains on the sample surface after the scotch tape test, which shows similar adhesion as that of the directly-deposited metal films. For a sputtered Au film of 170nm, the area of the remaining Au films is different than the molding materials. Figure 3.8 shows both the remaining film adherence area and reported surface energy of the molded materials.

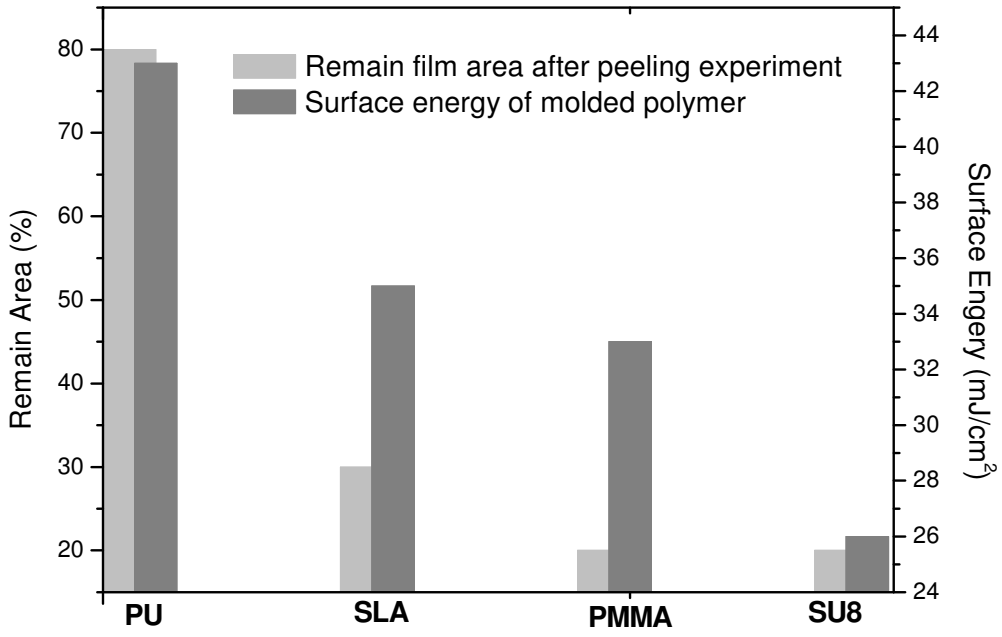

Figure 3.7 Scotch tape test results of metal film adhesion for different polymers

Although it has been demonstrated that non-covalent forces can be large enough to transfer gold from PDMS to other materials in the conventional nTP process, mild heating (50-80^{o}C) is usually needed to reduce the transfer time from several days to hours [71]. However, for the replica molding process, the metal transfer is in part a result of the solidification of the cast polymer. In some processes the metal transfer can be completed within a minute. For example, the epoxy acrylate resins (Accura® si100) can be cured by high intensity UV light (10mW/cm^2 for 50 seconds) and the gold film is completely transferred from PDMS after demolding.

Furthermore, in the conventional nTP process, metal transfer to substrates with large surface roughness is less effective than a substrate with small surface roughness [71], while in this metal transfer molding process, there is no significant roughness effect observed in metal transferability as long as the liquid-state polymer conformally wets the

interface during the molding step. To demonstrate metal transferring over a large rough surface, as shown in Figure 3.9, PDMS molded from a master structure with simulated roughness (dimple arrays with different density and dimension) is coated with Au/Ti, polymers such as SU-8, PMMA, and PU are cast on the PDMS mold, and the gold film is found to be transferred from the PDMS completely. For transfer printing, gold on a rough surface can not be completely transferred to a smooth substrate due to the roughness on the mold surface, while for metal transfer molding, the fluidic polymers wet all the rough surface and form a high quality bond with the Au film to achieve a complete transfer.

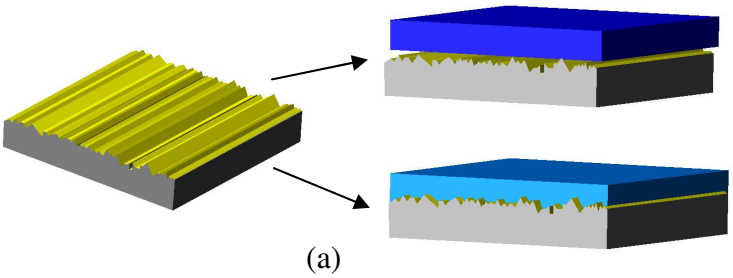

(a)

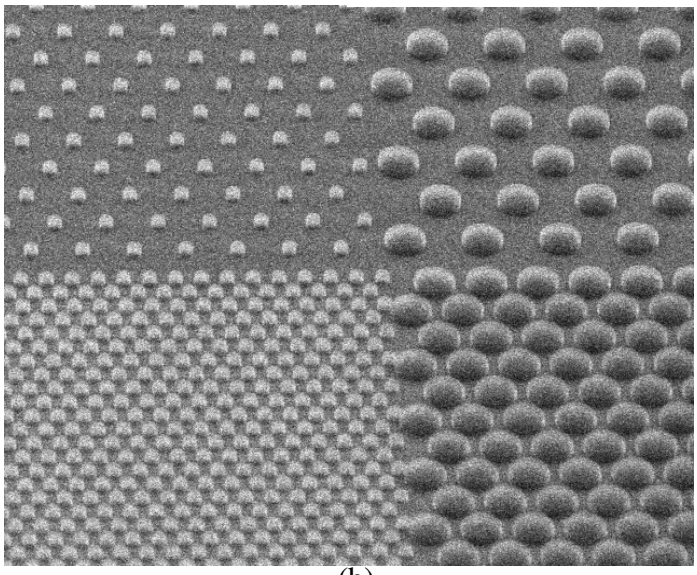

(b)

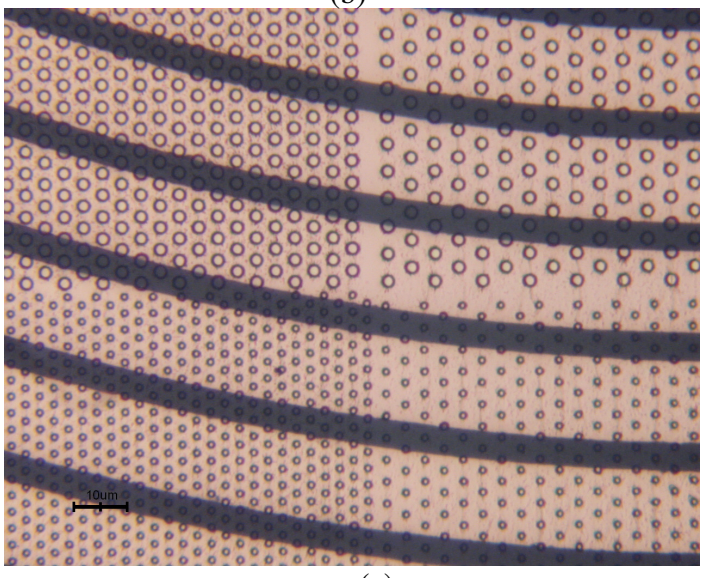

(c)

Figure 3.8 Demonstration of surface roughness effect of MTM (a) Schematics of the roughness effect on the metal transferring printing and molding; ; (b) simulated “roughness” on a stamp by photolithography (d)metal pattern is completely transferred from the “rough” PDMS surface to the cast polymer.

3.4 RF Micromachined Structures by MTM

For 3-D RF components with improved performance, not only the 3-D components themselves, but also the interconnections, such as transmission lines, should be fabricated in a simple and effective fashion. The details of the MTM process for such structures are discussed below.

3.4.1 Master Structure Fabrication Techniques

By using this 3-D metal transferring process, not only can extruded micro structures such as posts or lines can be metallized during replica molding, but also a patterned electrical connection of these structures can be formed simultaneously. This approach can be utilized for the fabrication of polymer core air-lifted RF components. It comprises three steps:

Master fabrication A master device is initially fabricated and can be used repeatedly to generate multiple batches of molds and devices. There are many approaches to master realization, including conventional photolithography on either thick or thin resists, as well as stereolithography. A popular technique from the MEMS community is the photolithography of negative photo-definable epoxy SU-8 to make high-aspect-ratio 3-D structures. A typical multilayer fabrication process is shown in Figure 3.9. A first layer of SU-8 is patterned to define the structure of the planar RF components such as the transmission line, which in this work, is a coplanar waveguide (CPW). Then, several layers of SU-8 are patterned one by one to define the 3-D structures with differing height, such as a monopole antenna array at various resonant frequencies. After the multiple exposures and bake steps, the structure can be finalized in one develop and cure step.

Using this multilayer SU-8 fabrication technique, a structure with different height profiles can be very precisely defined. An example of this multilayer structure is also shown in Figure 3.10.

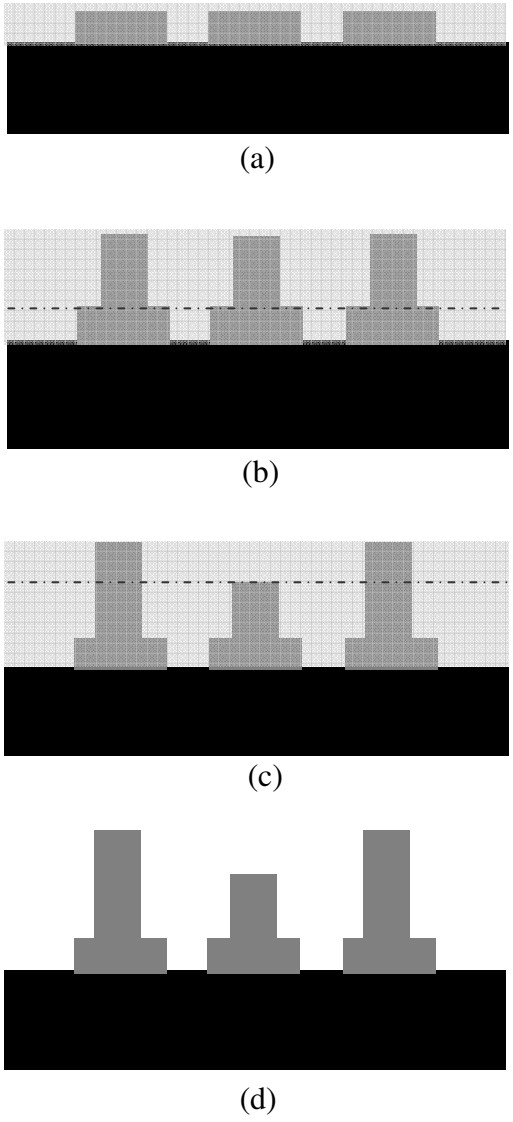

Figure 3.9 Process flow of multi-layer fabrication of SU-8

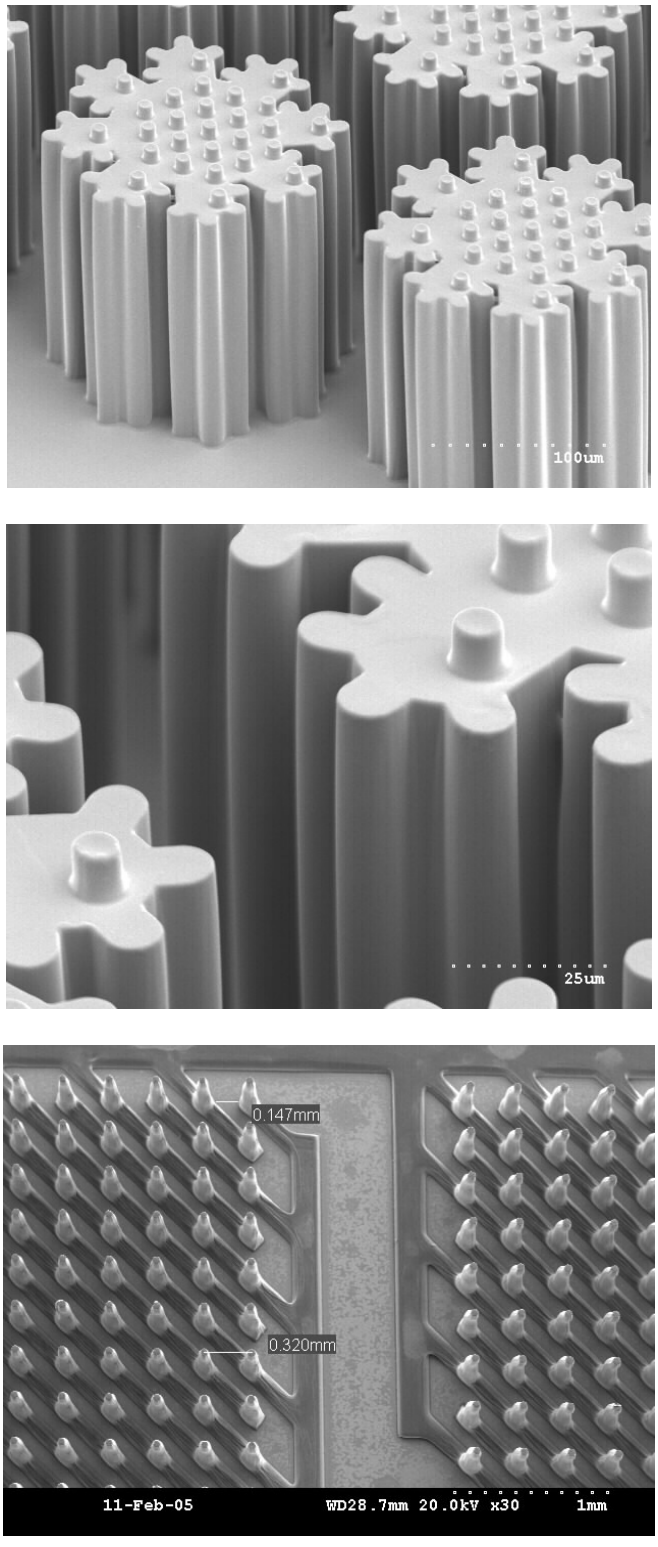

Figure 3.10 Fabricated examples of multi-layer SU-8 process

3.4.2 Metal Patterning Techniques

Mold preparation After the master is fabricated, a negative mold is created by casting and curing a suitable molding material, such as polydimethylsiloxane (PDMS), around the master. Commercially available Sylgard 184 prepolymer (Dow Corning) is used in this work. The mold is then separated from the master structure.

Mold metallization The PDMS mold is coated with a thin metal film (usually 200 nm–500 nm Au or Au/Ti multilayer) by e-beam or DC sputter deposition. A transfer printing process is performed to remove the metal film on the raised regions of the stamp mold (Figure 3.11) by immediately placing the freshly metal-coated PDMS mold onto a flat, smooth substrate leads to "wetting" that provides intimate contact between the two surfaces. The substrate that we use is a standard polyester tape (SherconTM PC21 masking tape) with a thin layer of adhesive. The polyester tape is gently peeled off and the metal layer on the raised region is transferred to the tape. Now the original PDMS mold has a metal film coated only on the recessed regions that were originally patterned during the master fabrication step, and no subsequent patterning on three-dimensional surfaces is required.

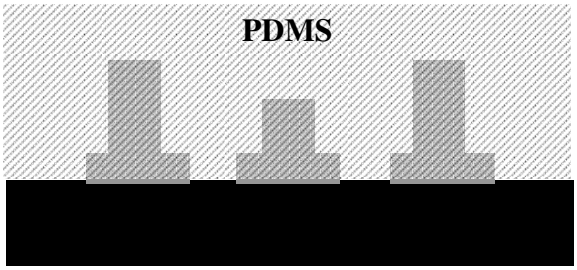

Cast and cure silicone rubber (PDMS)

(a)

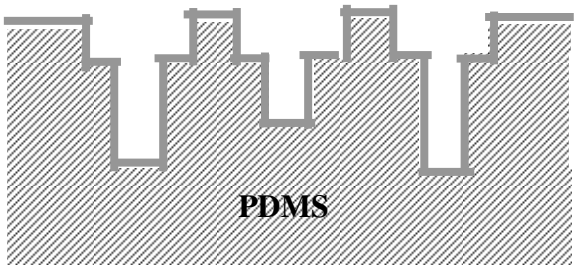

Prepare PDMS mold coated with Au

(b)

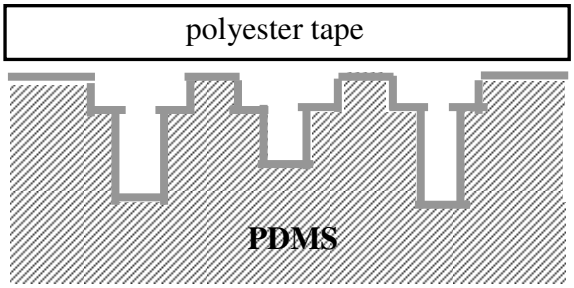

Conformal contact the top surface of PDMS with a high energy surface

(c)

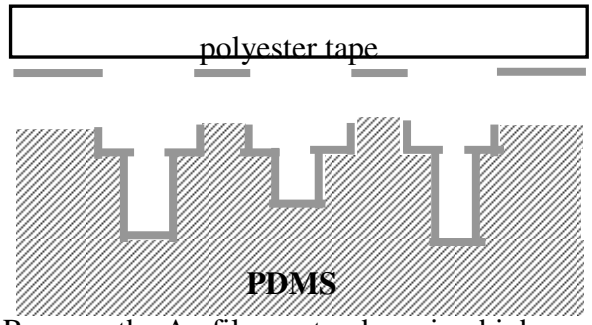

Remove the Au film on top by using high energy surface

(d)

Figure 3.11 Mold preparation process flow

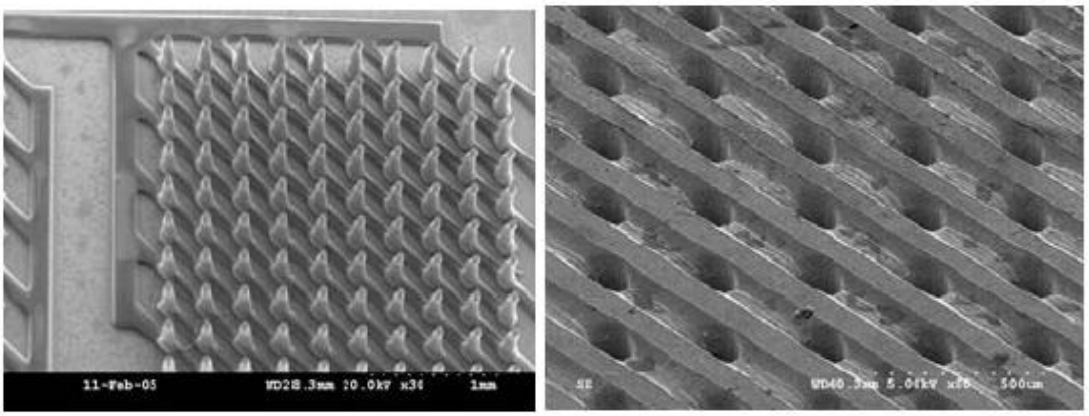

(a) (b)

Figure 3.12 An array of high aspect ratio electrodes (100 μm diameters)
(a) master (b) PDMS mold

Metal-Transfer-Molding Polymer (uncured, melted or dissolved in solvent) in the liquid state is cast into the PDMS mold. Although standard injection molding approaches can be used in this step, for the polymers studied in this work, only vacuum or heat was necessary to ensure full wetting of the PDMS mold by the polymer. Further, it was observed that the patterned metal film on the recessed regions of the mold aided wetting. After the cast polymer is solidified, the PDMS stamp mold is peeled off and the metal film within the recessed region is completely transferred to the molded part (Figure 3.13). The transferred metal is then optionally thickened using electroplating of appropriate metals.

Figure 3.14 shows a molded micro post array coated with gold film using metal transfer, and the posts are electrically interconnected so as to form a 'checkerboard' pattern. The pattern is fabricated in a simple molding process. In chapter 1, the same structure is made by SU-8 micromachining which include more than 6 process steps.

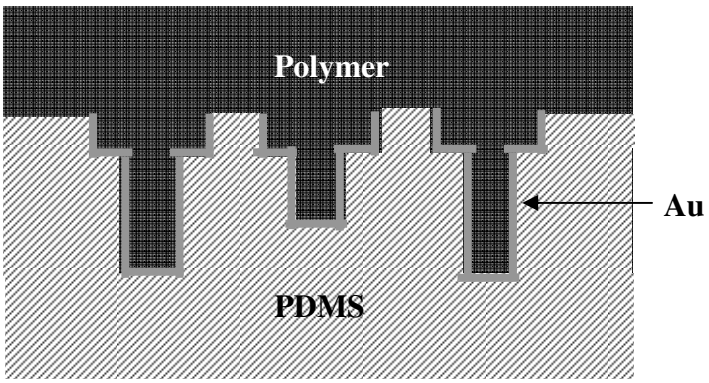

Casting polymers and

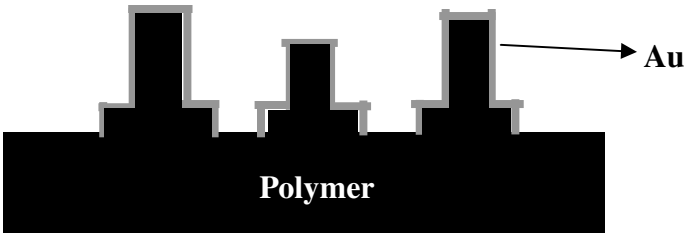

De-molding with metal transfer

Figure 3.13 Process flow of final step of metal-transfer-molding

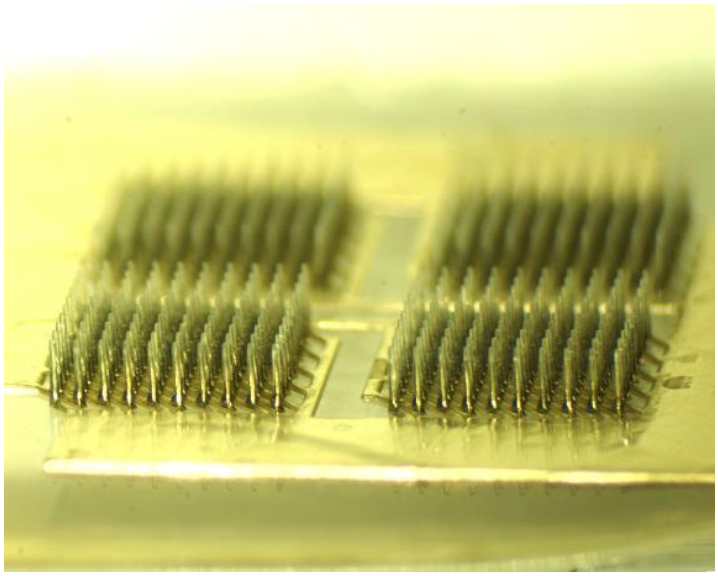

Figure 3.14 Metal transfer molded MEA with checkerboard pattern electrical connection

3.4.3 Summary of MTM Technique

Compared with the SU-8 surface micromachining approach, the MTM technique has several unique advantages. First, the fabrication process is much simpler and easier. Once the PDMS mold is prepared, the remaining processes are metal sputtering, molding, and electroplating, and these processes can be repeated on the same PDMS mold to produce more batches of devices. It should also be noted that these processes can performed without the use of a cleanroom, so the fabrication cost may be greatly reduced. Since the molded RF components are made from the same materials as the substrate, so there is no potential for de-lamination of the 3-D components, especially when compared with the previously- presented SU-8-based devices, this property is very useful for the air-lifted components and subsequent packaging process.

The summary comparison of different micromachining techniques is listed in Table 3.2. In the following work, a series of millimeter wave components are demonstrated by MTM process.

Table 3.3 Process comparison of solid conductor process, SU-8 micromachining, and metal-transfer-molding (MTM) process

	Solid Conductor Process	Polymer-Core Conductor Process	
	Via Mold Electroplating	SU-8 Surface Micromachining	Metal-Transfer-Molding
Conductor type	Solid	Hollow	Hollow
Patterning materials	Conventional photoresist	SU-8	Most thermoplastic polymers
Structure aspect ratio	~5	~10	~5 (~10 achievable by additional mask)
Metallization	Via filling plating (difficult, long time)	Coating plating (easy, short time)	Coating plating (easy, short time)
Mechanical adhesion	Moderate	Weak [48]	Very Strong
Photolithography (2 layer structures)	3 times (Via mold patterning)	3 times (SU-8 patterning and selective metallization)	0 times (for mold replica)
Facilities needed	Photolithography Sputtering Plating Etching	Photolithography Sputtering Plating Etching	Sputtering Molding Plating
Preferred RF applications	High Power MEMS Conductor	Single air-lifted RF/mm-wave component	Multiple 3-D RF/mm-wave components

Chapter 4

Development of Air-lifted RF Components by MTM

The MTM technique developed in this work has been demonstrated successfully in the fabrication of metallized 3-D polymer structures, and these structures have great potential in high frequency applications. In this chapter, several RF components such as air-gap coplanar waveguide (CPW), monopole antenna, and evanescent-mode high-Q cavity resonator are developed based on the MTM technology.

4.1 Low Loss Coplanar Waveguide (CPW)

4.1.1 Concept

Transmission lines are the basic interconnect units of RF components. CPW has become more and more popular for microwave monolithic and hybrid integrated circuits due to its advantages of compact size, lower dispersion, and easy integration of series and shunt devices. In spite of the wide use of printed planar circuits in microwave and millimeter wave systems, metallic waveguides still play an essential role in various components like antenna feeds, high-Q filters, diplexers, and so on. Therefore, the increased use of CPW circuits in both commercial and military systems will drive the search for high performance, easy integration, and low cost transitions to rectangular waveguides. A second important advantage of CPW which has recently emerged is in the design of microwave probes for on-wafer characterization of field effect transistors and for fast, inexpensive evaluation of microwave integrated circuits. In order to fully utilize

these advantages, transitions between CPW and other microwave transmission media are required.

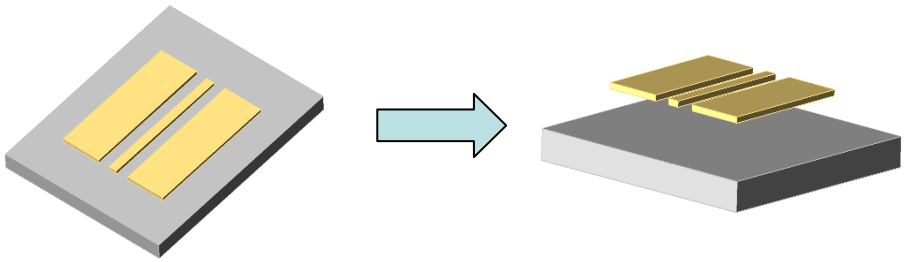

Figure 4.1.Air-lifting of CPW transmission lines for reducing substrate effects

However, the geometric structure of these conventional transmission lines has dielectric loss and dispersion characteristics due to the substrate effects and degrades the circuit performance at high frequency range. To reduce this substrate effect, one of the techniques is the air-lifting of both of the center and ground conductors, thus, air is the only dielectric material between the conductor and ground (Figure 4.1). Research into low-loss transmission lines using MEMS technology is proceeding in several groups [26, 76-77]. While the transmission line structures reported have excellent advantages concerning the loss characteristic in high frequency when compared to the conventional transmission line, the lengthy fabrication steps greatly increases the cost. In addition, the integration of CPW and other RF components is important for the development of system-on-package. Thus, an easy realization of low loss CPW is highly desired for the low cost RF system-on-package (SOP).

A design for CPW with air gaps suitable for the MTM process is shown in Figure 4.2. Figure 4.3 shows the simulated electric field for this CPW design, illustrating that the electric field is mainly confined between the edges of the metal lines. As a result, most of

the substrate couplings occur in these E-field crowded regions. Thus, removal of the material in these regions is predicted to significantly reduce the substrate coupling and the subsequent loss.

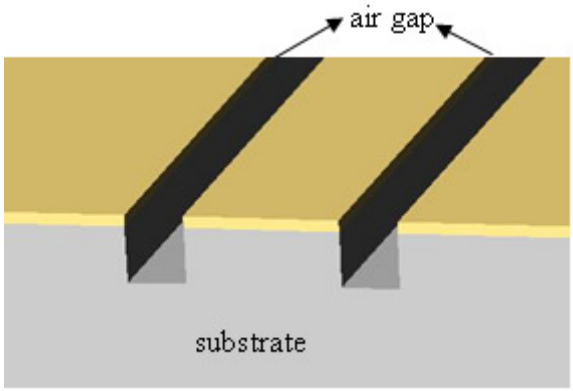

Figure 4.2. Concept of CPW with air-gaps

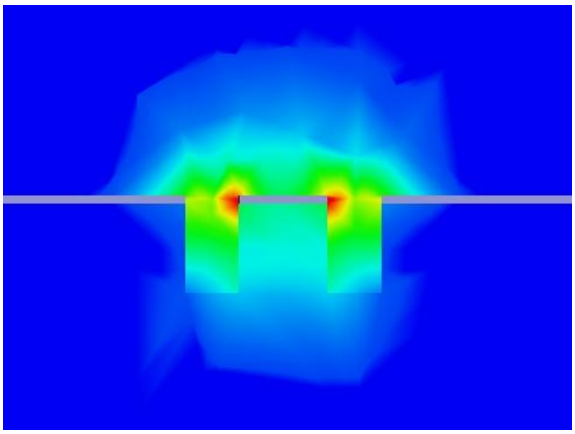

Figure 4.3 Simulated electric field of CPW with air-gaps by HFSS 10.0

4.1.2 Design and Fabrication

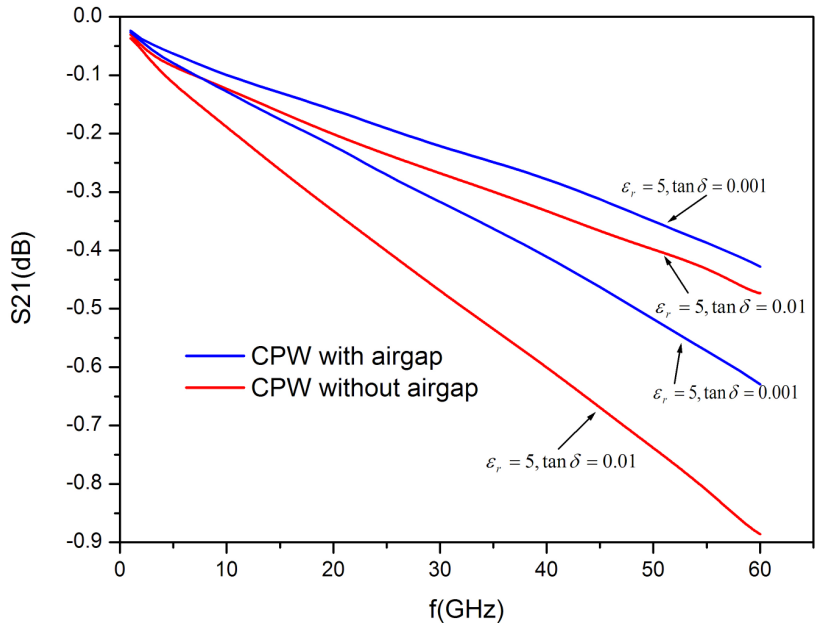

Figure 4.4 Transmission loss of CPW line on epoxy resin with or without air-gap

Figure 4.4 shows the simulated transmission loss for a 5mm CPW with or without air gap by the simulation program HFSS 10.0. In a lossy substrate, the transmission loss can be greatly reduced by the existence of the air gap. For example, on a substrate of $\varepsilon = 5$, $\delta = 0.01$, the transition loss of the conventional 5mm long CPW is 0.1dB, while the 50 μm air gap reduces the loss to less than 0.05dB.

Because most of the electrical field is within air gaps, the effective dielectric constant of the CPW is reduced. As a result, the characteristic impedance of the waveguide is increased. Figure 4.5 shows the calculated impedance of the CPW using standard lithography or molding of epoxy (ε =5.0) as compared with the airgap CPW. The characteristic impedance has been calculated as a function of the normalized center

conductor width using HFSS 10.0. The gap width and depth are fixed at 50 μm for these curves in order to maintain compatibility with both fabrication and measurement facilities. The ground plane is assumed to be infinite in the simulations.

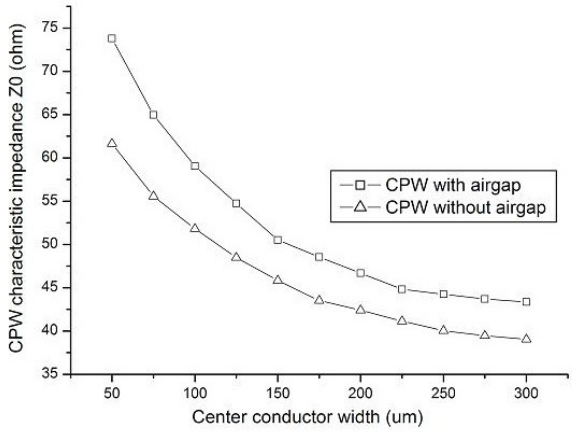

Figure 4.5 Impedance of CPW line on epoxy ($\varepsilon = 5$, $\delta = 0.01$) with or without air gap

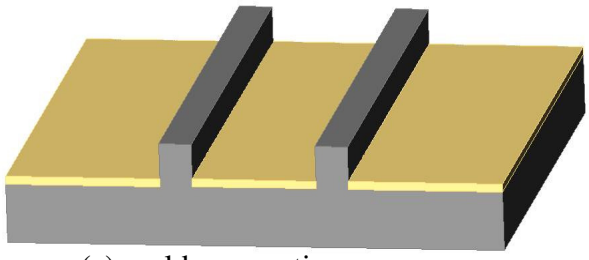

(a) mold preparation

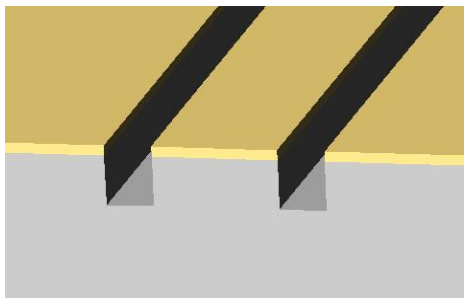

(b) metal transfer molding

Figure 4.6 Fabrication process of CPW with air-gap by MTM

The fabrication of CPW structures using metal MTM is shown in Figure 4.6. After removing the metal film on the raised surface of the PDMS mold by polyester tape, the metal film on the bottom transfers to the molded polymers, where electrically isolated air gaps are uniquely formed. Using this molding and a subsequent electroplating process, a CPW transmission line with air gap can be directly formed without any etching process. After electrodeposition of 2 microns or more of copper, the air gap CPW can be formed for RF signals more than 30GHz. The transferred metal layer also coats the side wall of the air gaps. However, there is no electroplated copper on the side wall due to the narrow opening, so only the surface of CPW transmission lines can propagate RF signals.

4.1.3 Applications to CPW Filter

A CPW bandstop filter is designed and fabricated using the MTM process. The filter is based on a short-circuited transmission line $\lambda/4$ resonator [41].

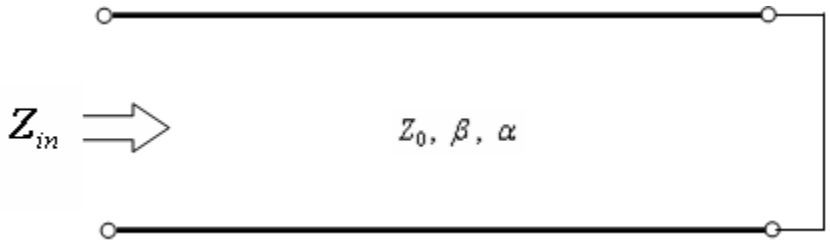

Figure 4.7 Schematic of short-circuited transmission line resonators

Consider a length of lossy transmission line, short circuited at one end, as shown in Figure 4.7. The line has a characteristic impedance Z_0, propagation constant β, and

attenuation constant α. At the frequency $\omega = \omega_0$, the length of the line is l. The input impedance is:

$$Z_{in} = Z_0 \frac{1 - j \tanh \alpha l \cot \beta l}{\tanh \alpha l - j \cot \beta l} \tag{4.1}$$

Now assume $l = \lambda/4$ at $\omega = \omega_0$, where $\lambda = 2\pi/\beta$, and let $\omega = \omega + \Delta\omega$ then for a TEM line,

$$\beta l = \frac{\omega_0 l}{v_p} + \frac{\Delta\omega l}{v_p} = \frac{\pi}{2} + \frac{\pi\Delta\omega}{2\omega_0} \tag{4.2}$$

where v_p is phase velocity, and so

$$\cot \beta l = \cot(\frac{\pi}{2} + \frac{\pi\Delta\omega}{2\omega_0}) = -\tan \frac{\pi\Delta\omega}{2\omega_0} \approx \frac{-\pi\Delta\omega}{2\omega_0} \tag{4.3}$$

Also, $\tanh \alpha l \approx \alpha l$ for small loss, using these results in equation 4.1,

$$Z_{in} = Z_0 \frac{1 + j\alpha l \pi\Delta\omega / 2\omega_0}{\alpha l + j\pi\Delta\omega / 2\omega_0} \approx \frac{Z_0}{\alpha l + j\pi\Delta\omega / 2\omega_0} \tag{4.4}$$

This result is of the same form as the impedance of a parallel RLC circuits as following:

$$Z_{in} = \frac{1}{(1/R) + 2j\Delta\omega C} \tag{4.5}$$

Using this analogy the shorted $\lambda/4$ line is equivalent to a resonator with:

$$R = \frac{Z_0}{\alpha l} \tag{4.6}$$

$$C = \frac{\pi}{4\omega_0 Z_0} \tag{4.7}$$

$$L = \frac{1}{\omega_0^{\ 2} C} \tag{4.8}$$

The resonator of Figure 4.7 thus has a parallel type resonance for $l = \lambda / 4$.

To further reduce the size of $\lambda / 4$ resonator, this filter is then designed as a triple-folded CPW short stub structure [77]. The width of each stub finger is 50μm. Figure 4.8 shows the schematic of the filter design. The filter length is 1mm on the substrate.

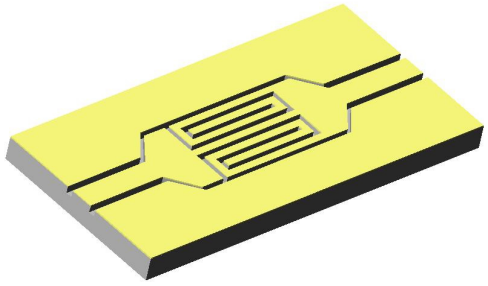

Figure 4.8 Triple-folded design of CPW band-stop filter

A photomicrograph of the PDMS mold of the band-stop filter is shown in Figure 4.9(a), and the metal film on the raised region of the PDMS mold is removed by a polyester tape shown in Figure 4.9(b). The fabricated filter is shown in 4.9(c), and 4.9(d) shows an array of filters arrays made on a flexible epoxy substrate by MTM processes.

The characteristics of the MTM molded filters with 35 μm or 25 μm air gaps are given in Figure 4.10(a)(b). An insertion loss (S_{21}) of less than 2.5 dB at pass band is

observed. The insertion loss in the stopband is approximately 20dB which is very close to the HFSS simulation. The loss in passband is due to both the substrate loss and conduction loss. According to the simulation, the dielectric loss can be reduced to only 0.5dB of total loss (dielectric loss and conduction loss) by using this air gap configuration. Compared with the high dielectric loss of about 2dB by a conventional CPW transmission line, the air gap structures greatly reduces the substrate loss. Results from the metal-transfer-molded bandstop filters demonstrate that planar components such as CPW transmission lines and stub filters can be successfully fabricated using this molding process. An integration of the CPW transmission line and high-aspect-ratio monopole antennas is further demonstrated.

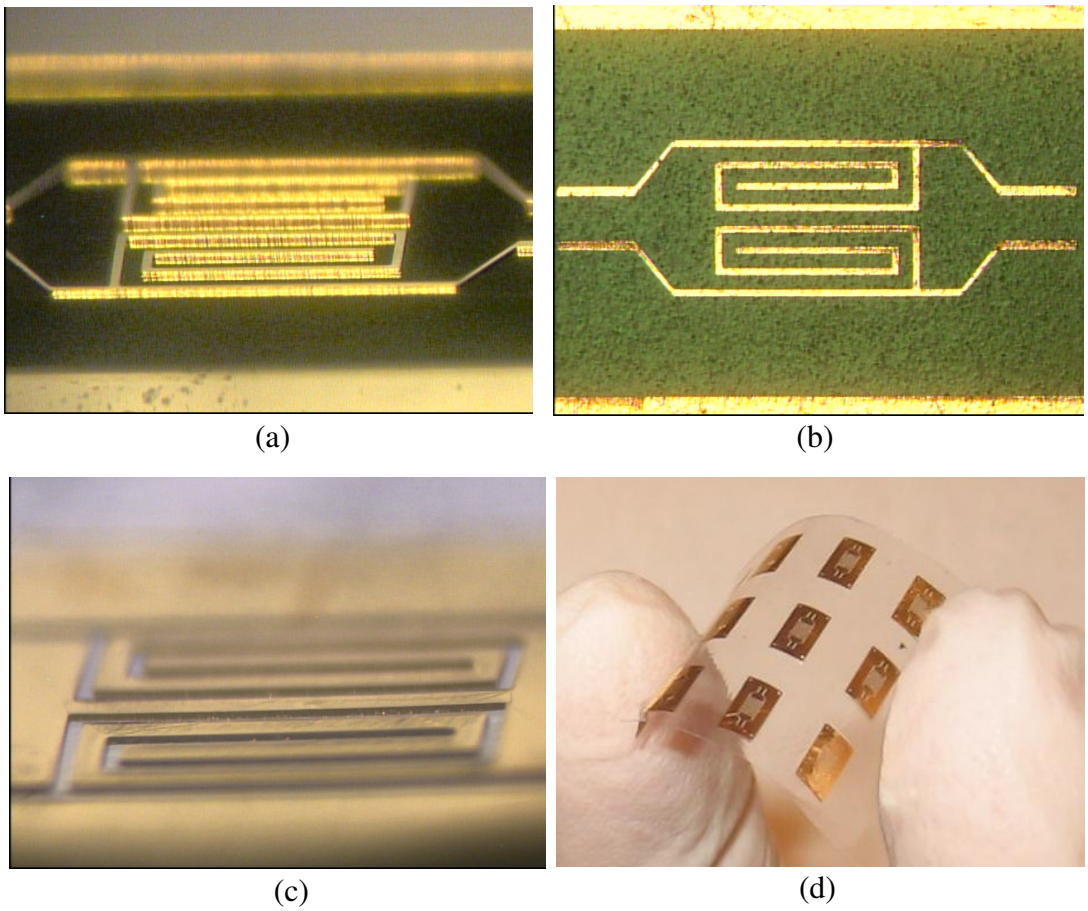

Figure 4.9 Fabrication process of triple-folded CPW band-stop filter by MTM process (a) PDMS mold with metal coating (Ti/Au) (b) Removed metal pattern by polyester tape (c) MTM filter structure on PMMA (d) Filter array on a flexible PMMA substrate

(g)

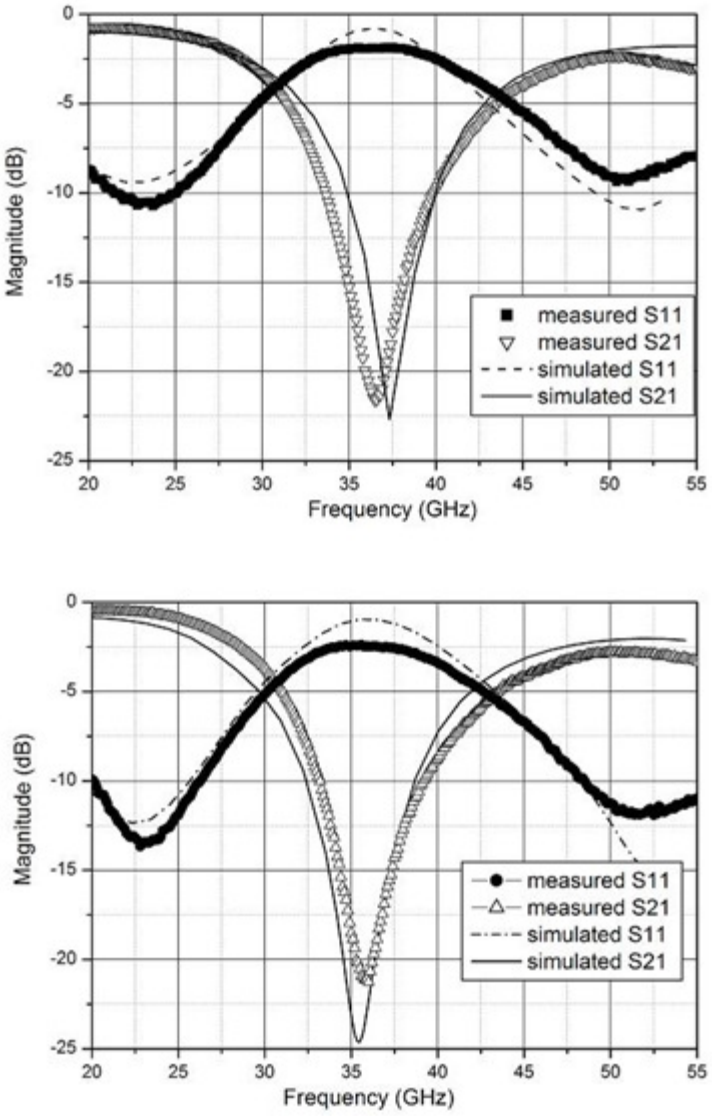

Figure 4.10 Measured and simulated S11 and S21 of MTM band-stop filter with (a) 35μm air gap (b) 25μm air gap

4.2 Ka-Band Monopole Antenna

One of the key components for a wireless millimeter-wave system is its radiating structure, i.e., antenna. Although wire antennas (e.g., dipole or monopole antennas) can be considered as alternatives to printed-circuit patch antennas because of their broad bandwidth, low loss, and reduced dependence on the substrate, fabrication difficulty has prevented them from being efficiently implemented and integrated in a cost-effective fashion.

4.2.1 Half Wave Dipole and Quarter Wave Monopole

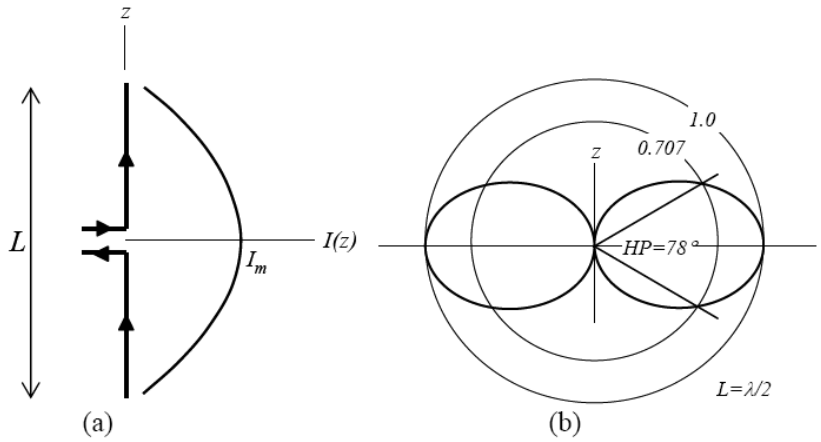

Figure 4.11 A center-fed dipole antenna:
(a) Schematic and current distribution when L=λ/2; (b) Radiation pattern when L= λ/2

A monopole antenna is considered as a dipole antenna that has been divided in half at its center feed point. An analysis of a quarter-wavelength monopole antenna can be deduced from that of a half-wavelength dipole antenna. A half wave dipole antenna is resonant antenna having a standing wave over the length and zero input reactance at resonance, thus eliminating the need for tuning to achieve a conjugate impedance match. A dipole oriented along the z-axis is depicted in Figure 4.11a. It is fed at the center and

the currents of each wire are equal in magnitude and opposite in direction. The current distribution along the antenna is assumed to be sinusoidal and current-distribution measurements indicate that it is a good assumption as long as the antenna is thin and based on ideal wire made of good conductors [63]. The current distribution can be written as Equation 4.9:

$$I(z) = I_m \sin[\beta(\frac{L}{2} - |z|)], \qquad |z| \le \frac{L}{2} \tag{4.9}$$

where I_m is the peak current and β is the wave constant. The far-field electric and magnetic field of a dipole antenna is determined by integrating the fields for an infinitesimal dipole of length dz at a distance r from the antenna:

$$E_\theta = j\eta I_m \frac{e^{-j\beta r}\cos[(\beta L/2)\cos\theta] - \cos(\beta L/2)}{2\pi r \sin\theta} \tag{4.10}$$

$$H_\phi = jI_m \frac{e^{-j\beta r}\cos[(\beta L/2)\cos\theta] - \cos(\beta L/2)}{2\pi r \sin\theta} \tag{4.11}$$

where η is the intrinsic impedance of the medium which is 120π in air. The θ-variation of this function determines the far-field pattern.

For $L = \lambda/2$, the normalized far-field pattern $F(\theta)$ is written in the following equation and depicted in Figure 4.10(b). The 3dB beamwidth is 78° shown in Figure 4.11(b).

$$F(\theta) \equiv \frac{E_\theta}{E_{\theta,\max}} = \frac{\cos[(\pi/2)\cos\theta]}{\sin\theta} \qquad (4.12)$$

The radiation power P is calculated by integrating the Poynting vector over the sphere surrounding the dipole antenna. It is expressed in simple terms for the half wave dipole in air as following:

$$P = 36.5 I_m^{\,2} \qquad (L = \lambda/2) \qquad (4.13)$$

The radiation resistance R_r is then calculated as:

$$R_r = \frac{2P}{I_m^{\,2}} = 73\Omega \qquad (L = \lambda/2) \qquad (4.14)$$

The impedance Z_A of an ideal half wave dipole is expected to have only resistance term when $L = \lambda/2$. The quarter wave antenna thus has an impedance of half of the dipole, i.e. 36.5Ω.

In fact, the dipole antenna has resonance at a slightly shorter dipole length than $\lambda/2$, where the reactance term is zero. As the wire thickness increases, the inductance contribution from the thick wire is more significant, thus the dipole should be further shortened to accomplish resonance. Table 4.1 shows the approximate the wire length for resonance with various wire diameter $2a$ and length L [78].

Table 4.1 Wire length vs. resonant frequency for dipole or monopole

Length to diameter ratio ($L/2a$)	Shortening required [%]	Resonant length		thickness class	Geometry
		Dipole (L)	Monopole(L/2)		
5000	2	0.49λ	0.245λ	Very thin	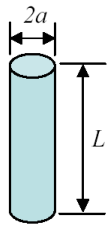
500	4	0.48λ	0.24λ	Thin	
50	5	0.475λ	0.238λ	Less thick	
10	9	0.455λ	0.228λ	Thick	

4.2.2 Design Concept

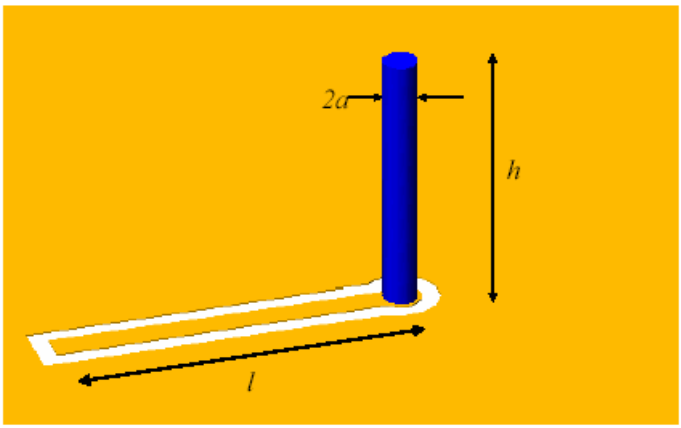

Figure 4.12 Schematic of the CPW fed vertical monopole antenna

In our work, the length to diameter radio between 10 and 20 is utilized, so according to table 4.1, the resonant wavelength is designed at

$$\lambda = \frac{h}{0.228} \tag{4.15}$$

where h is the height of the monopole antenna.

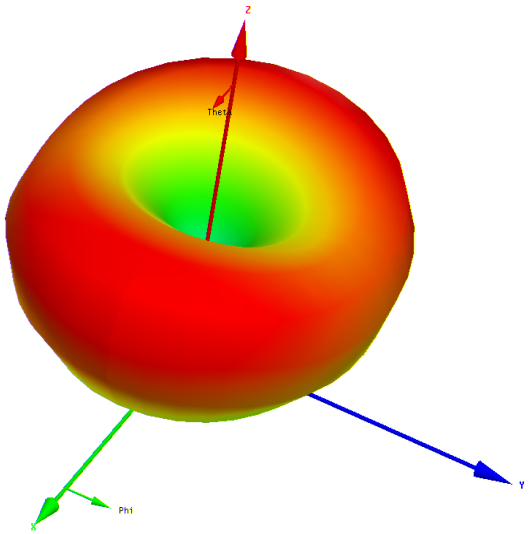

Figure 4.13 Simulated radiation pattern of a vertical monopole antenna

A CPW-fed vertical monopole antenna is shown in Figure 4.12. One of the unique properties of the monopole antenna is omni-directional radiation pattern (Figure 4.13). It is very useful in RF high-data-rate transceiver module or chip-to-chip wireless communications [64]. At higher frequencies such as Ka-band or W-band, the copper transmission line suffers from the high loss and dispersion. Wireless data link at these frequencies has a great potential for the future chip-to-chip interconnect. Monopole antenna is a good candidate because of its compact size and omini-directional radiation pattern.

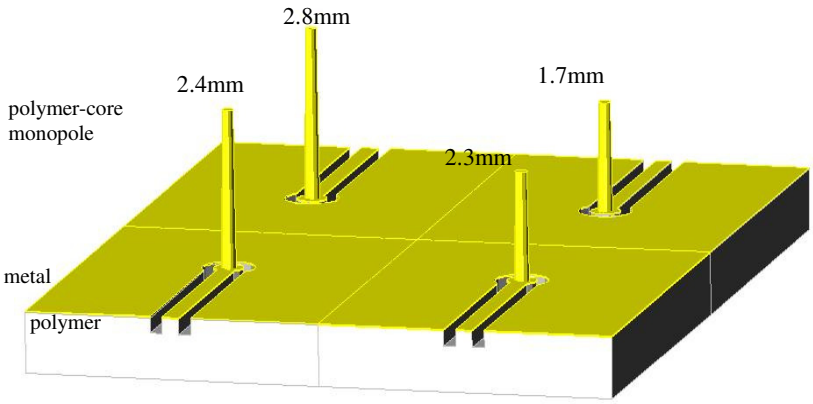

Figure 4.14 Schematic of a monopole antenna array operating in 26, 30, 32, 42GHz

The quarter-wavelength monopole antenna in W-band has been successfully demonstrated using the polymer-core surface micromachining technique [19]. However, since the aspect-ratio is about 10:1 and the height for the monopole in W-band (1 mm to 680 μm) is close to the fabrication limits of SU-8 micromachining, it is very challenging to precisely control the monopole height. Besides, the adhesion of the high-aspect-ratio polymer structures with substrates such as glass, silicon, or quartz is generally poor. Using a molding process offers the advantages of precise height control as well as ease of integration with other radiation structures at different resonant frequencies. An array of cylindrical quarter-wavelength monopole antennas fed by CPW on the same substrate operating and covering most Ka-band is fabricated to demonstrate the simultaneous integration of 3-D and planar RF components by MTM. Both the monopoles and the substrate are made of molded epoxy resin with an aspect ratio of up to 14:1.

In our design, the central operating frequency for the monopole is chosen in Ka-band (18-40GHz): 26GHz, 30GHz, 32GHz, and 42GHz, and these four monopoles are used to cover the Ka-band. The feeding schematic is simply connecting the CPW line

without other impedance transforming techniques which would not perturb the radiation pattern (Figure 4.14).

4.2.3 Fabrication and Measurement

The master structures are fabricated by 3-D stereolithography, and the molded structures are made by photo-curable epoxy resin (Accura® si100) which can be solidified by UV light (10mW/cm^{2}second) within 1 minute after casting, and the metal is completely transferred during this short solidification period. All monopoles of the same diameter (200 μm) and of different heights (1.7 mm to 2.8 mm) are molded on the same substrate. The fabricated device is shown in Figure 4.15. Since the aspect ratio is as high as up to 14: 1, an additional post-molding metal deposition step is needed to metallize the protruding portions of the monopoles by using a shadow mask. This step is only needed for high-aspect-ratio structures to achieve the conformal metal coatings on the sidewalls, while a precise pattern such as the CPW transmission line on the substrate has been achieved during the metal transfer molding process. The transferred and further deposited metal film work as a seed layer in the following electroplating process by which the final metal layer thickness is about 10μm (to be more than five times the skin depth).

All the monopole pillars and the substrate are molded from the same material, so there is no mechanical interface between the substrate and the 3-D structures. Unlike the previous polymer core techniques using SU-8 on a glass or quartz substrate, there is no thermal expansion mismatch and delaminating issues for the MTM molded RF devices.

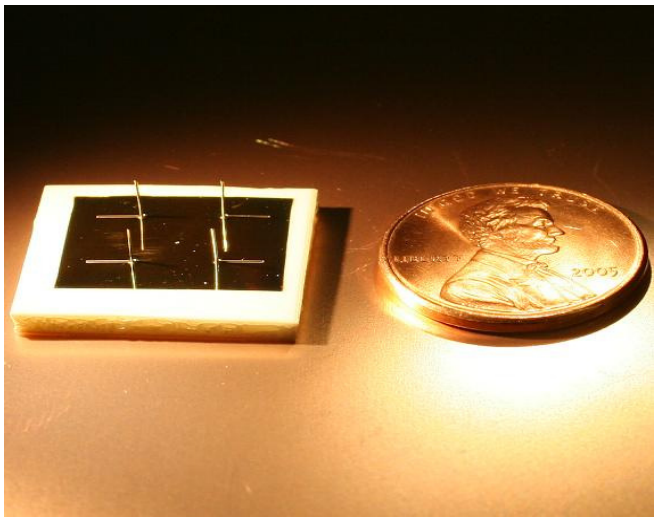

(a)

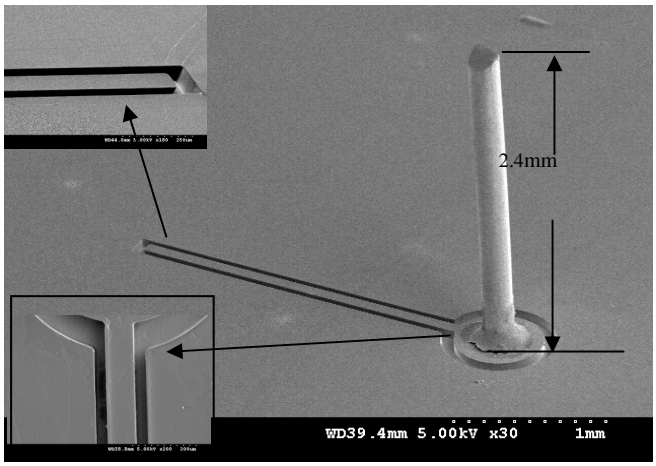

(b)

Figure 4.15 Fabricated monopole antenna array (a) a picture of a fabricated monopole antenna array operating at resonant frequencies from 25GHz to 42GHz. (b) a SEM picture of the monopole antenna with height of 2.4mm

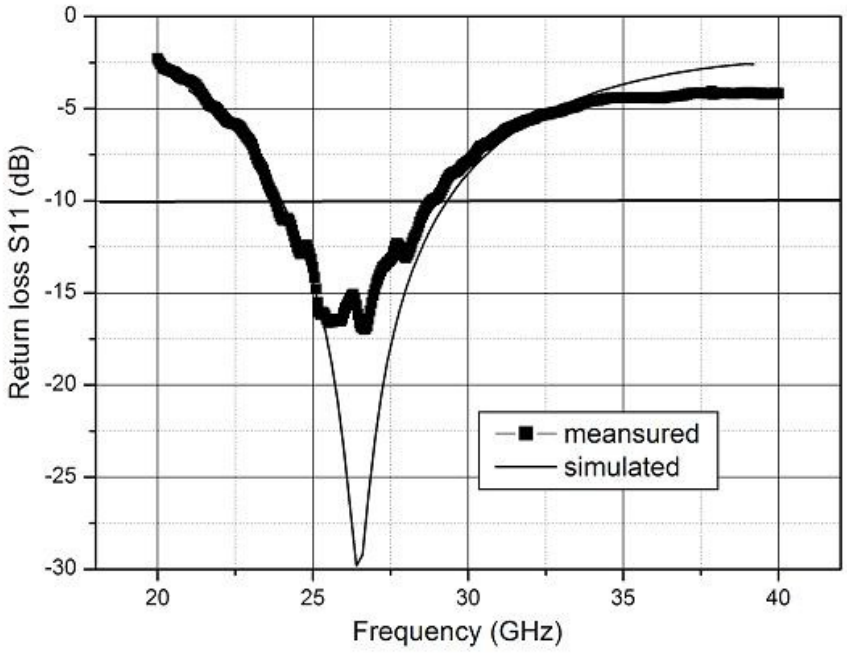

(a) Return loss of 2.83mm high monopole antenna

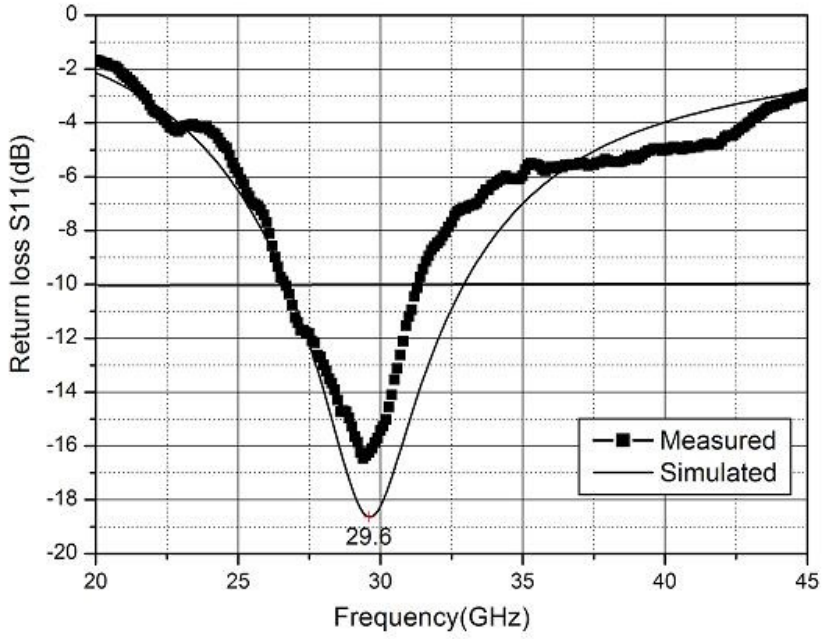

(b) Return loss of 2.43mm high monopole antenna

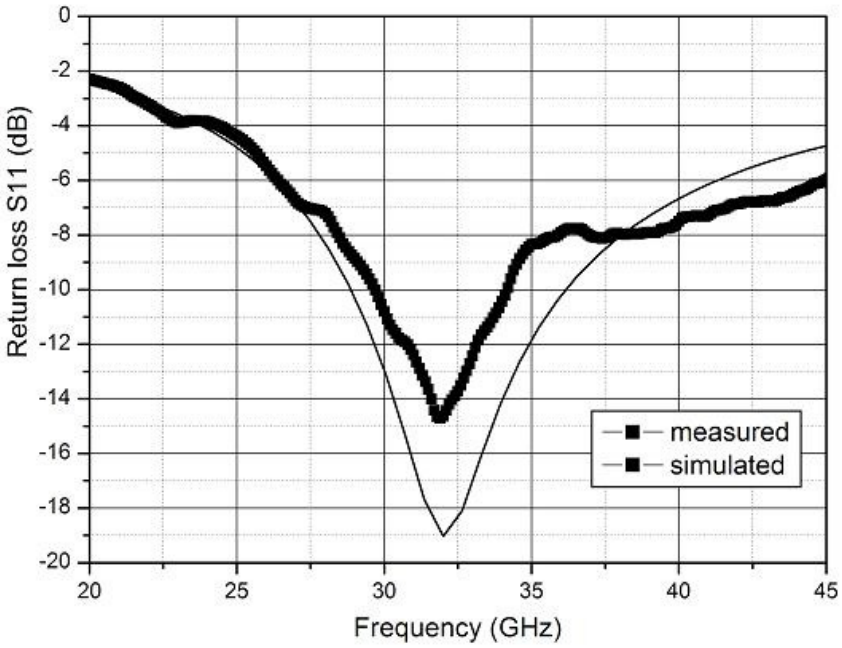

(c) Return loss of 2.34mm high monopole antenna

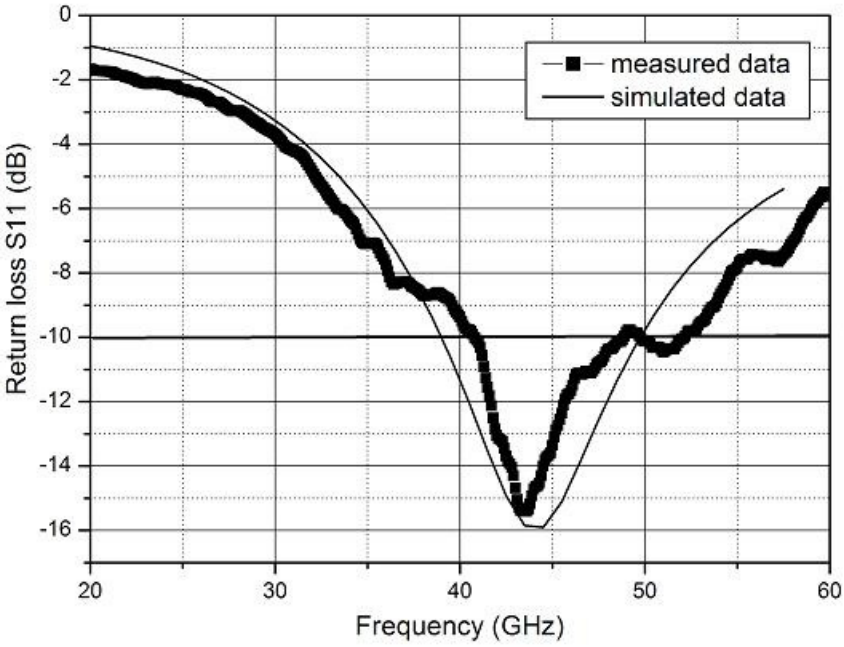

(d) Return loss of 1.71mm high monopole antenna

Figure 4.16 Characteristics of MTM fabricated monopole antennas

4.2.4 Discussion

An S11 measurement is performed using an Agilent 8510X vector network analyzer as shown in Figure 4.16. Greater than 15 dB return loss bandwidth is achieved. The 10 dB-bandwidths at the resonant radiation frequencies are 21.5%, 15.8%, 14.1%, and 18.4%, respectively, for the tested structures. The measurements show a good radiation performance at all the resonant radiation frequencies, and simulation by HFSS10.0 shows very close results to the measured resonant frequency and bandwidth.

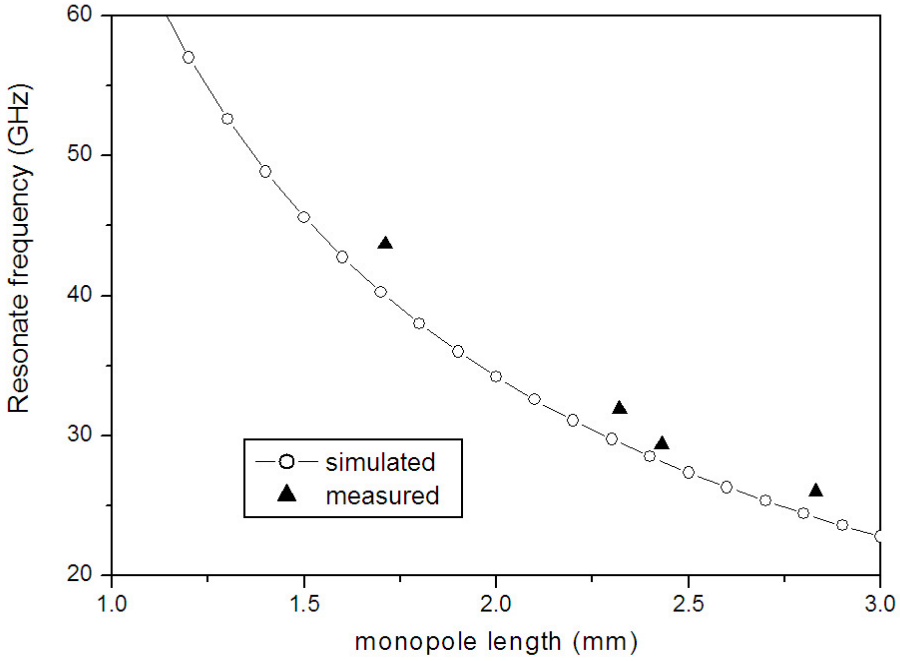

Figure 4.17 Measured and simulated resonant frequency vs. monopole height

The control of the resonant frequency is also very important as is the bandwidth. As discussed previously, the monopole is cylindrical with a diameter of *2a* rather than an

ideal wire with zero thickness. The non-ideal cylindrical monopole therefore has an inductive reactance term attributable to the nonzero width of the conductor when it is driven at the radiating resonance frequency of an ideal monopole of the same height. This reactance term results in the non-ideal monopole having its actual resonance at a slightly lower frequency than that of an ideal monopole. Alternatively, if a particular resonant frequency is desired, the monopole length can be reduced to achieve the ideal monopole resonant frequency. The simulated and measured resonant frequencies of the quarter-wavelength monopoles are plotted in Figure 4.17. The aspect-ratio of the actual monopoles is slightly different from 10:1 (all monopoles have a 200μm diameter with different heights), which explains the small deviation between the simulated and measured results.

4.3 Miniature Cavity Resonators

4.3.1 Review of Cavity Resonators

A high-Q resonator is a very important millimeter-wave component and is widely used in the design of high-selectivity filters and diplexers. Such resonators are also required in many applications such as LANs, point-to-point communications, automotive radar, and RF sensors. There has been an increasing effort to develop cavity resonators to achieve high Q performance in a low-cost fashion.

Planar resonators and cavity resonators are widely used in wireless communication systems. Table 4.2 shows a comparison of these two types of resonators. Planar resonators are extensively used in RF design due to their simplicity and low

fabrication cost, but they usually have limited Q and require low loss substrates. Conventional microwave high Q resonators made by metallic rectangular or cylindrical waveguides are heavy, large, and costly to manufacture. Furthermore, they do not allow for easy integration with monolithic integrated circuits. With the maturity of micromachining techniques in fabricating microwave circuits, it is now possible to make miniature micromachined waveguides or cavities [79, 80] as building blocks for the development of high-Q resonators or filters. The quality factor that can be achieved with this technique is much higher than the quality factor of traditional microstrip resonators either printed on a dielectric material or suspended in air with the help of a dielectric membrane [81].

Table 4.2 Comparison of planar resonator and cavity resonator

	 **Planar Resonator**	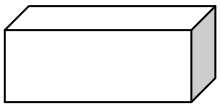 **Cavity Resonator**
Size	Compact	Bulky
Q	Low (typically <200)	High (typically >1000)
Fabrication Cost	Low (lithography, etching)	High (Metal Machining)
Integrate Capability	High	Low

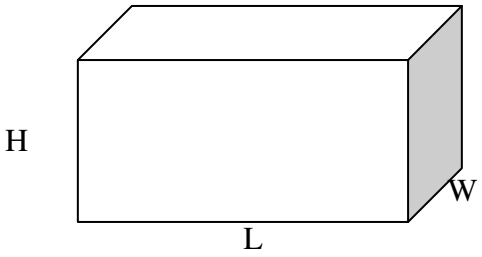

Figure 4.18 Schematic of rectangular cavity resonator

One of the most-studied micromachining techniques for cavity resonators is silicon micromachining. However, the cavity dimension is limited because of the silicon wafer thickness, and the etching process is time-consuming and costly. Moreover, the half wavelength cavity resonator with air dielectric takes large space on the board. Figure 4.18 shows a rectangular cavity resonator. The resonant frequency of the T_{mnl} mode is obtained from Equation 4.13 [41]:

$$f_{res} = \frac{c}{2\pi\sqrt{\varepsilon_r}}\sqrt{(\frac{m\pi}{L})^2 + (\frac{n\pi}{H})^2 + (\frac{l\pi}{W})^2} \qquad (4.16)$$

For example, for an air-filled cavity with equal length and width, Table 4.3 shows the example dimension of several resonators with air dielectric operating at TE101 mode. At common frequencies for current wireless communication systems such as 2.4GHz, the dimension of the cavity is close to 9cm, which is very challenging to be integrated in mobile devices.

Table 4.3 Example dimensions for cavity resonator with air dielectric

Frequency	2.4GHz	5.8GHz	10GHz	30GHz
Dimension	88.5mm	44.3mm	21.2mm	7.1mm

The cavity size can be reduced by filling the cavity with high dielectric constant materials; however the quality factor Q decreases greatly due to the introduced dielectric loss. Meantime, the dielectric constant changes with the environment temperature, which can reduce the stability of the resonant frequency and increase the packaging cost.

In many situations, size reduction is required due to space and weight restrictions, while filter performance can not be greatly sacrificed. Thus, compact, low-loss filters are commonly designed utilizing the evanescent-mode concept [82]. Evanescent-mode filters have advantages over half-wavelength cavity-based filters such as a smaller size and an improved spurious-free region with a low insertion loss [83]. High-Q evanescent-mode filters have been widely implemented in the form of comb line and ridge waveguide filters. Reduced-size evanescent-mode resonators have also been implemented in band-stop filter designs [84]. However, all the aforementioned topologies are difficult to be monolithically integrated with other RF components. Polymer-core techniques using the MTM process have great potential for the fabrication of these structures in a low-cost and rapid fashion.

4.3.2 Design Concept

Figure 4.19 shows the concept of an evanescent-mode cavity resonator. By loading a resonant cavity with a post in center, the resonant frequency of the cavity can be

reduced, while a relatively high unloaded quality factor is maintained. The post is shorted electrically with the cavity itself.

An HFSS full-wave eigen-value analysis is performed to determine the resonant frequency and the operating mechanisms of the resonator. Since there is no simple analytical equation for the evanescent-mode resonators, HFSS10.0 eigen-mode analysis method is utilized to analyze the resonators.

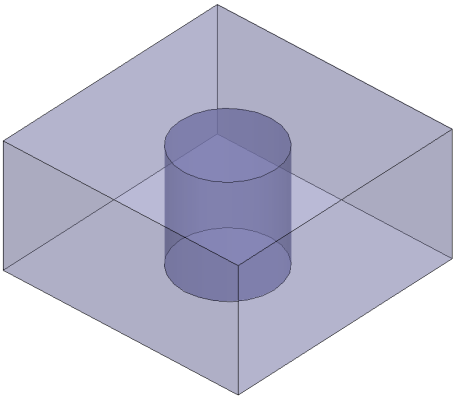

(a)

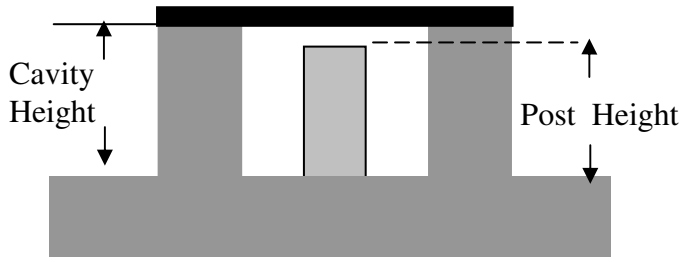

(b)

Figure 4.19 Schematic of evanescent-mode cavity resonators
(a) concept view (b) cross-sectional view

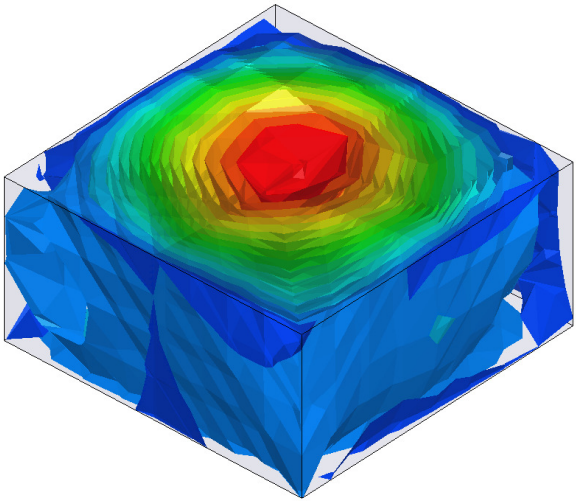

(a)

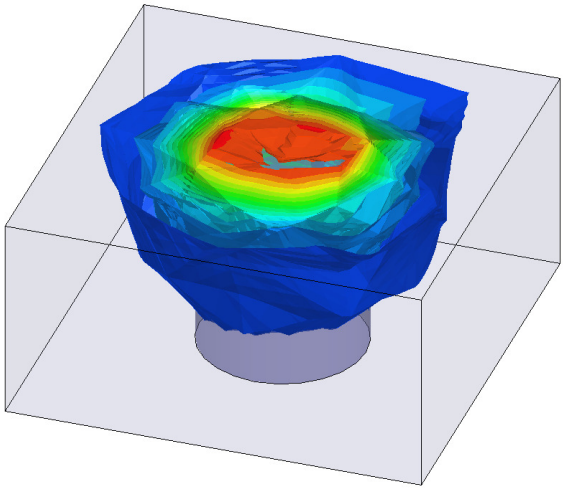

(b)

Figure 4.20 E-field inside the cavity by HFSS10.0 eigenmode simulations
(a) rectangular cavity resonator (b) evanescent mode cavity resonator

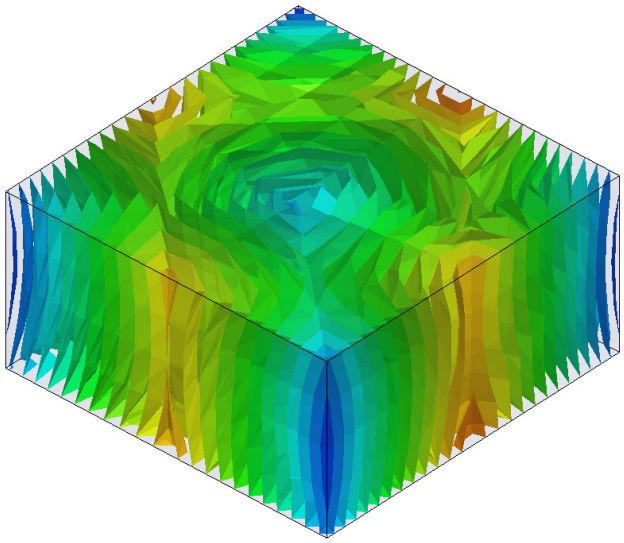

(a)

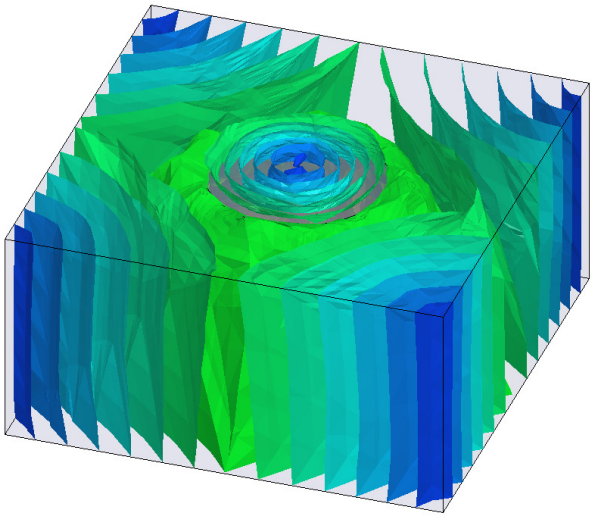

(b)

Figure 4.21 H-field inside the cavity by HFSS10.0 eigen-mode simulations
(a) rectangular cavity resonator (b) evanescent mode cavity resonator

Figure 4.20 shows the simulated electrical field inside a rectangular cavity resonator and evanescent-mode cavity resonator. Figure 4.21 shows the simulated magnetic field inside a rectangular cavity resonator and evanescent-mode cavity

resonator. All simulations for the resonators are at resonance. Loading a resonant cavity with a capacitive post creates a quasi-lumped element structure. This capacitive post provides a perturbation to the resonance of the cavity and can lower the frequency.

As is shown Figure 4.20, most of the electric field is stored in the air gap between the central post and upper surface of the resonator, while the magnetic field is stored in the area surrounding the post. As a result, the top of the post is referred to as the capacitive section while the region external to the post is referred to as the inductive section. The Q of this resonator is not sacrificed mainly because the currents induced are very similar to the ones excited in an unperturbed cavity. Since there is a magnetic field null at the center of the cavity with and without the perturbation (Figure 4.21b), the post introduced at the center of the resonant cavity leaves the magnetic field relatively unchanged. The region surrounding the capacitive post, the primary inductive region, still has the full thickness of the substrate in which to store the magnetic field, thus maintaining the Q of an enclosed resonator. The magnetic field is directly related to ohmic losses, since the Q is proportional to the volume storage area for the field relative to the surface area for the currents. In the position of the post, there is a strong electric field resulting in a high stored electric energy and standing charges associated with it. Though this region has a relatively small volume, it does not entirely sacrifice the Q because the currents are not affected. However, this region stores the electric field and the increased capacitance decreases the resonant frequency significantly [ ].

To accurately describe and simulate the 'evanescent' effect of the resonance, an equivalent circuit can be developed. The resonator can be divided into two distinct sections, the capacitive and inductive regions. As the air gap between the top surfaces of

the post and cavity becomes much smaller, a lumped element model for the resonator becomes more accurate because the electric field becomes more confined to the capacitive section.

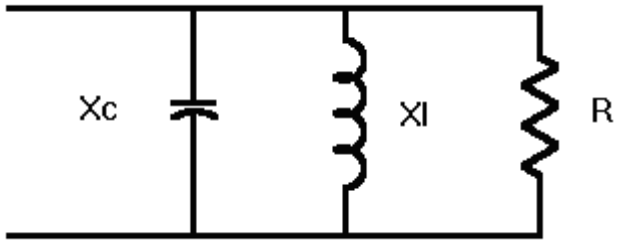

Figure 4.22 Equivalent circuit model of evanescent-mode cavity resonator

Figure 4.22 shows an equivalent-circuit model can be used to characterize the evanescent mode cavities. The total capacitance of the resonator is given by [43],

$$C_{total} = C_{post} + C_{remaining} \tag{4.17}$$

The post area adds a capacitance value that can be approximated by idealized quasi-static formula for a parallel plate capacitor:

$$C_{post} = \frac{\varepsilon_r \varepsilon_0 A}{d} \tag{4.18}$$

Then, the resonant frequency can be approximated by:

$$\omega \approx \frac{1}{\sqrt{L(C_{post} + C_{remaining})}} \tag{4.19}$$

Since most electric field is stored in the air gap, assuming $C_{post} >> C_{remaining}$, L is constant, then,

$$\omega \approx \frac{1}{\sqrt{LC_{post}}} \tag{4.20}$$

From Equation (4.18) and Equation (4.20), then,

$$f_0 = \frac{\omega}{2\pi} \approx \frac{1}{2\pi\sqrt{LC_{post}}} = \frac{1}{2\pi}\sqrt{\frac{d}{L\varepsilon_r\varepsilon_0 A}} \tag{4.21}$$

where f_0 is the resonator frequency of the evanescent-mode cavity resonator air gap d. Assume the there is a small change Δd of the air gap, i.e., the air gap becomes $d - \Delta d$, then for the new resonant frequency f_r:

$$\frac{f_r}{f_0} = \frac{\omega_r}{\omega_0} = \sqrt{\frac{d}{d - \Delta d}} \tag{4.22}$$

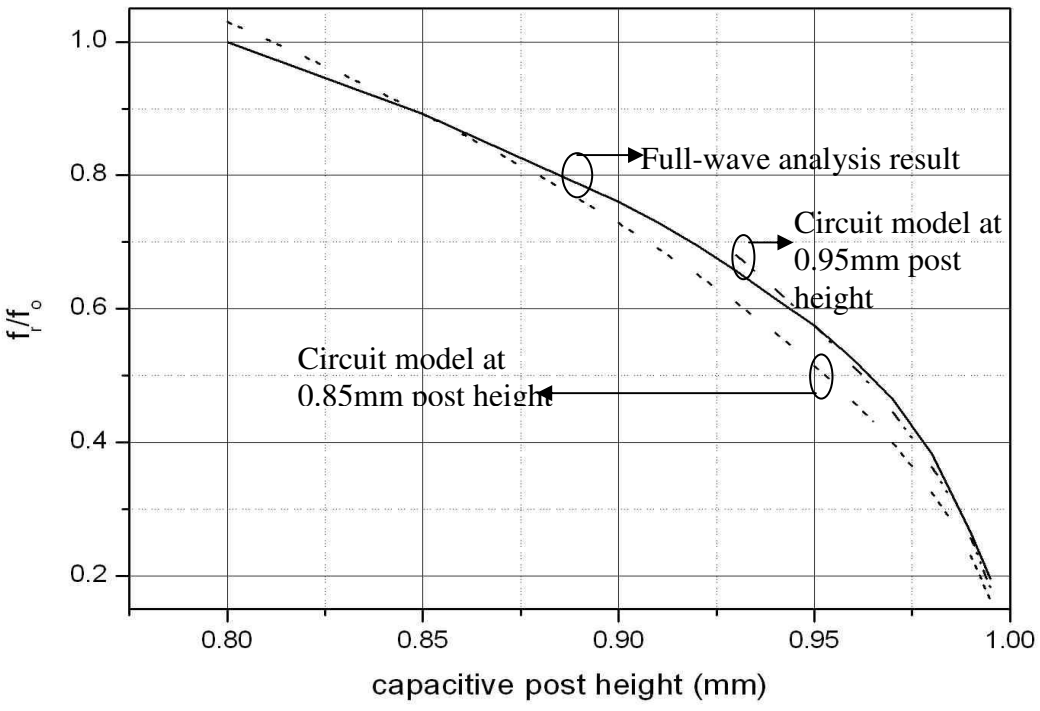

Figure 4.23 Simulated normalized resonant frequency vs. the post height using full-wave analysis and equivalent circuit model

Figure 4.23 shows the simulated resonant frequency (normalized) versus the post height, normalized by the resonant frequency before the change of air gap. The simulated cavity has a diameter of 5mm and height of 1mm. The solid curve is simulated by HFSS full-wave analysis, while the two dashed curves are simulated by Equation (4.22). It shows that when the air gap size is chosen to be 0.15mm, the simulated S11 curve based on the circuit model is less accurate. When the air gap size is chosen to be 0.05mm, the circuit model agrees very well with the full-wave analysis. Based on further simulations, a conclusion can be made that when the air gap size is less than 10% of the cavity height, the circuit model agrees well with the full-wave analysis (less than 10% error), however, when the air gap size is more than 10% of the cavity height, the circuit model is less accurate. Since the simulation time of circuit model is much shorter than the full-wave analysis, it is particular convenient for the sensitivity analysis in Chapter 5.

From equations 4.14 to 4.16, when the top surface of the post is close to the top of the cavity, C_{post} becomes the dominant capacitance, and the resonant frequency is highly sensitive to the post height. An approximate equation of the frequency sensitivity in relation to the post height can be derived from equation 4.21,

$$\Delta f \approx (\frac{1}{2\pi}\sqrt{\frac{d}{L\varepsilon_r\varepsilon_0 A}})' \Delta d \tag{4.23}$$

i.e.:

$$\Delta f \approx \frac{-\Delta d}{4\pi\sqrt{L\varepsilon_r\varepsilon_0 A d}} = -f_0 \frac{\Delta d}{2d} \tag{4.24}$$

Equation 4.24 shows that when the post-to-upper surface gap d is close to zero,

the sensitivity of the resonant frequency to the post height is increasing rapidly. So in a highly loaded cavity resonator, the frequency is highly sensitive to distance between the post and the top surface of the cavity.

For a given resonant frequency, the achievable size reduction of the cavity depends on the post height. The sensitivity analysis shows that fabrication tolerances are extremely important when the post height is close to the cavity height, representing a high loading factor. Evanescent-mode filters inside Low Temperature Co-fired Ceramic (LTCC) substrates can achieve limited size reductions, because the uncertainties of the individual layer's tape thickness prevents highly loaded frequency-precise LTCC resonators [85]. Layer-by-layer polymer stereolithography processing has been reported to realize evanescent-mode cavities in different geometries [43]. However, it is only useful for standalone structures and difficult to integrate with other components due to the challenges of selective metallization. A low cost and highly precision manufacturing technique is desired for this type of RF components, and small fabrication tolerances enable the accurate prediction of the desired post and cavity heights, and in turn, achieve desired resonant frequencies. Micromolding, as a precision replica technology, has a wide process window which enables the batch fabrication of these structures. Once the master structure is fabricated, the molded replicas can be fabricated with highly precise dimensions.

4.3.3 Design and Fabrication

Figure 4.24 shows the schematic of the CPW fed cavity resonator. 4.24(a) shows the cavity structure with capacitive post, and after a top plate bonding the side view of the

final device is shown in 4.24(b). The cavity is designed to be 6mm wide and 1mm high. By using the metal transfer technique, cavities with capacitive posts as well as CPW fed lines can be simultaneously formed.

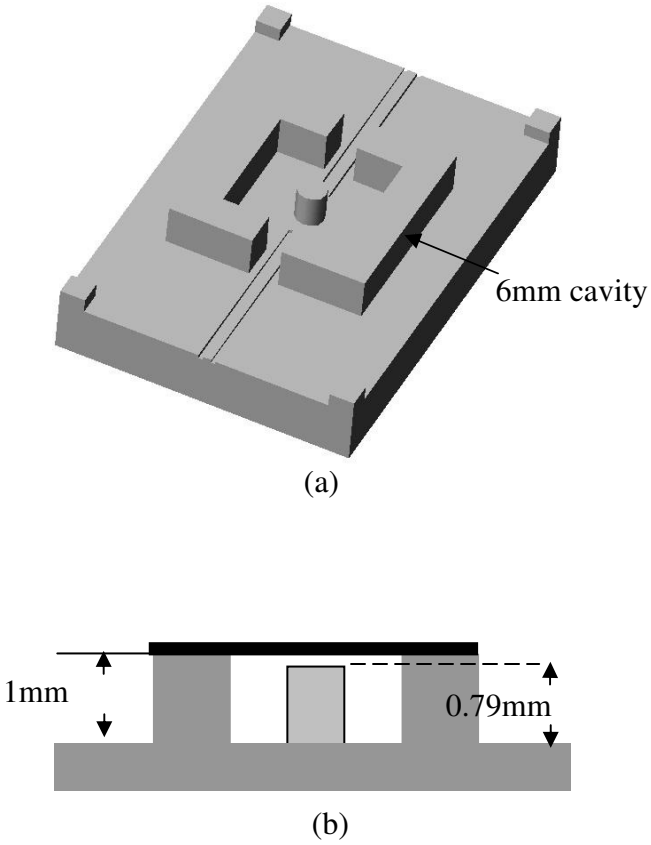

Figure 4.24 Schematic of the CPW-fed cavity resonator design
(a) lateral view (b) cross-sectional view

To accurately characterize the above design of evanescent-mode cavity resonators, an eigen-mode solution is obtained using full-wave analysis. Figure 4.25 shows the simulated results for a 6mm evanescent mode cavity by HFSS10.0 model. Figure 4.25(a) shows the resonant frequency and quality factor versus the post height. By adopting a

0.79mm capacitive post the frequency of the 6mm cavity will be reduced from 35.3GHz to 25GHz, while the unloaded Q still remains over 500. Figure 4.25(b) shows the surface current. When a small slot is opened on the sidewall, it is parallel to the surface current flow, so the effect of the opening on the resonator performance is expected to be minimal. The slot opening can be used for feeding structures.

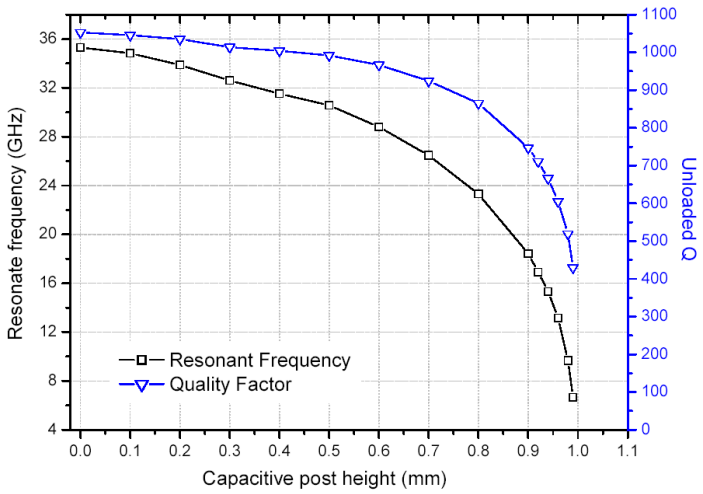

(a) Simulated resonant frequency and Q above design

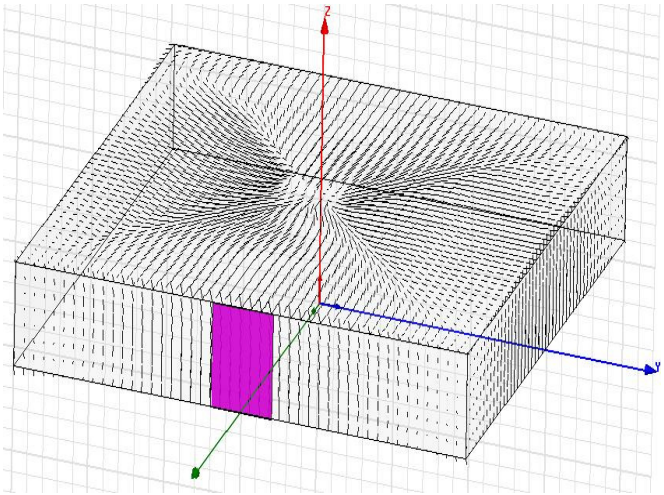

(b) Surface current flow by HFSS10.0

Figure 4.25 Simulated results for the evanescent-mode cavity resonator

Figure 4.26 shows the process flow for the evanescent-mode cavity resonator. The master structure is fabricated by stereolithography, and cavities are fabricated by MTM process. A piece of silicon with electroplated copper (10μm) seals the cavity by using silver epoxy bonding. The fabricated devices are shown in Figure 4.27. The height of capacitive post in the master structure made by stereolithography is 0.786mm.

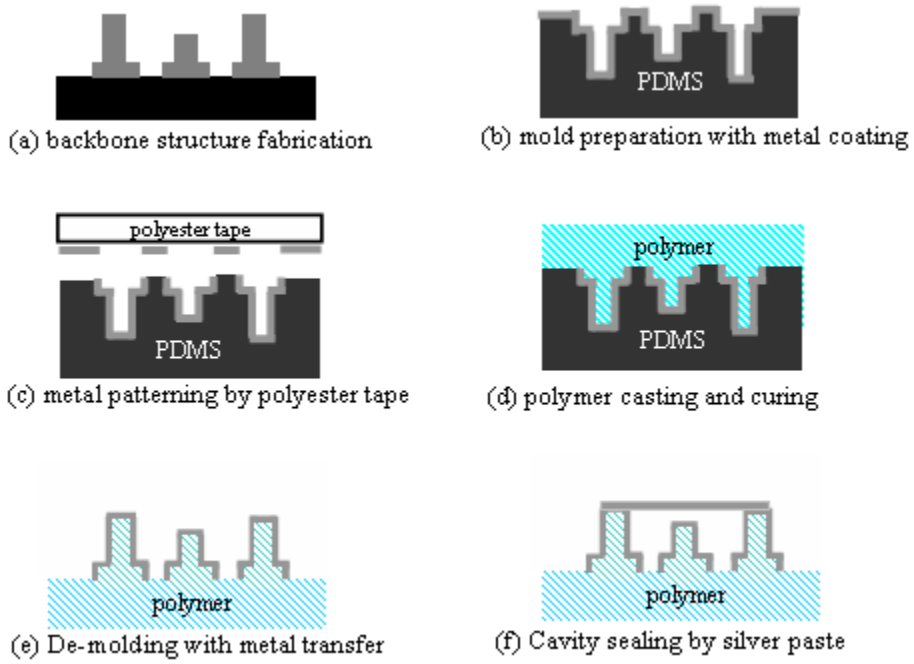

Figure 4.26 Process flow of cavity resonators

The external coupling can be modeled by an impedance transformer. The impedance barrier created by this transformer controls the amount of energy coupled to the filter. The larger the impedance mismatch the less the energy coupling. Critical external coupling is required for correct resonator responses. The resonators can be coupled to the outside using electrical field coupling, e.g. open coax feeding, or magnetic coupling, e.g. shorted CPW feeding. These external coupling mechanisms perturb the

field distribution inside the resonators, creating a frequency shift which makes the resonators resonate at different frequency. The accuracy of the post-fabrication resonant frequency is completely decided by the fabrication tolerances of the micromachining technique for the resonators and external coupling network.

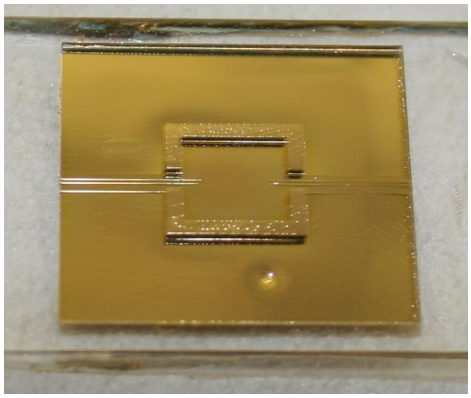

(a)

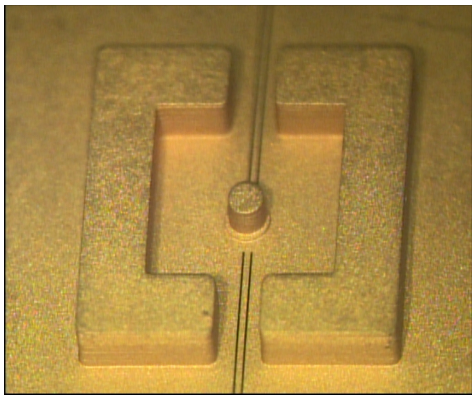

(b)

Figure 4.27 Metal-transfer-molded cavity resonator
(a) rectangular cavity (b) evanescent mode cavity resonator

In this work, CPW is used to feed the resonators via two openings on the sidewalls of the cavity. The CPW is designed to weakly couple the electric energy into

the cavity. The weak coupling enables the accurate determination of the unloaded Q of the resonator. Further, by using a CPW feed instead of coaxial cable, integration of other passive components on the same substrate is possible.

4.3.4 Characterization

The S-parameters of the fabricated resonators are measured by Agilent 8510C network analyzer. The resonant frequencies are measured by reading the peak of S21. The measured resonant frequencies of a 6mm cavity resonator with or without capacitive post are as predicted by HFSS eigenmode simulation. As desired, the resonant frequency is significantly reduced (from 35GHz to 24GHz) due to the evanescent mode caused by the small gap (210μm) between the top of the capacitive post and the top of the cavity (Figure 4.28(a)). , i.e, for a given frequency of operation, a 45.8% size reduction has been achieved.

Figure 4.28(b) and (c) show the S21 curves for the two resonators. The measured resonance shows good agreement with the HFSS10.0 simulation. From the measured curves, the 3dB bandwidth of each resonator and the minimum insertion loss are listed in table 4.4.

Table 4.4 Measured results of the cavity resonators

	Maximum S21	Resonant Frequency
Conventional Cavity	-15.23dB	34.99GHz
Evanescent Cavity	-21.53dB	23.90GHz

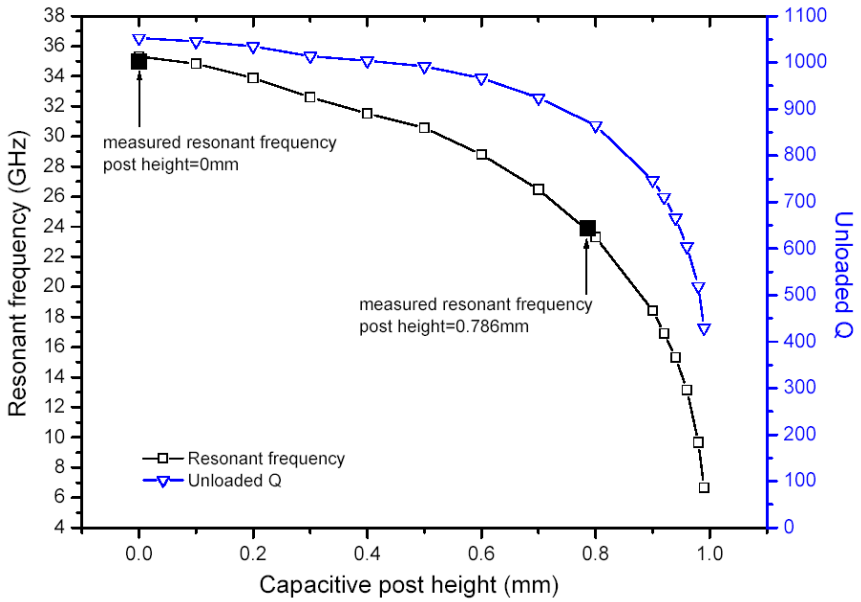

(a) Resonant frequency and unloaded Q versus post height

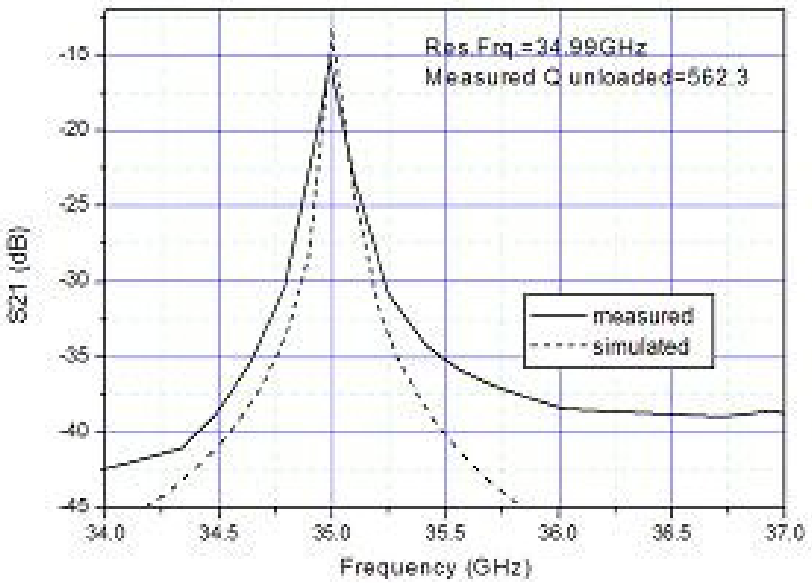

(b) measurement and simulation of regular cavity resonator

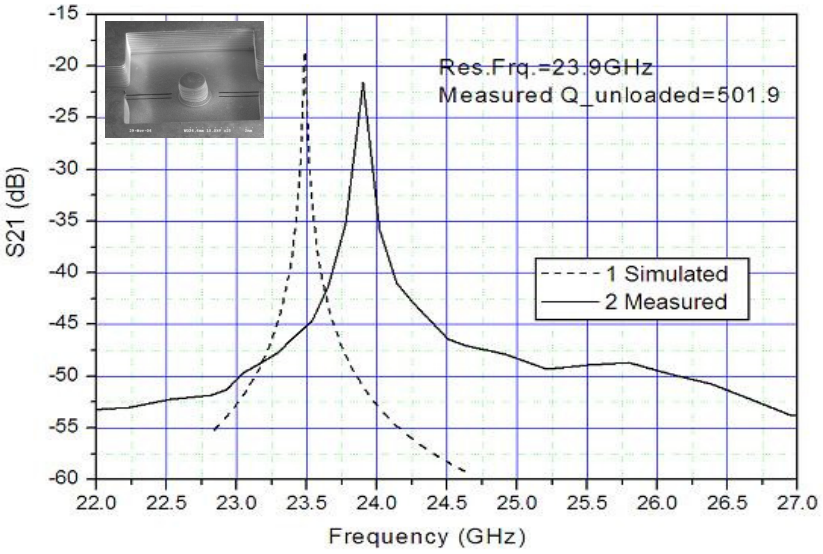

(c) Measurement and simulation of evanescent mode cavity resonators

Figure 4.28 Characteristics of MTM fabricated cavity resonators

For resonator, the unloaded Q can be derived from the measured loaded Q, as equation 4.6:

$$\frac{1}{Q_{loaded}} = \frac{1}{Q_{unloaded}} + \frac{1}{Q_{external}} \tag{4.18}$$

i.e.,

$$Q_{unloaded} = Q_{loaded} /(1 - Q_{loaded} / Q_{external}) \tag{4.19}$$

Since weak coupling is utilized in the design, the $Q_{external}$ can be derived from:

$$S_{21} = 20\log_{10}(\frac{Q_{loaded}}{Q_{external}}) \tag{4.20}$$

The Q_{loaded} can be derived form the measured S_{21} curve:

$$Q_{loaded} = \frac{f_{res}}{\Delta f} \tag{4.21}$$

The unloaded Q can be derived from the above equations from 4.18 to 4.21.High unloaded Q of more than 500 for both cavity resonators have been achieved (560 for half-wavelength cavity and 500 for evanescent mode cavity). The measured unloaded Q is less than that theoretically predicted (more than 800); this is attributed to the roughness of the sidewalls in the master devices produced by stereolithography. (Figure 4.26(b)). This indicates that in the MTM process, the master is critical; however, significant expense can be allotted to the master structure fabrication to achieve high part performance while still maintaining low part cost due to the nature of the MTM process.

4.4 Conclusion

This chapter explored the application of metal-transfer-molding (MTM) technique to 3-D RF components. Air-gap CPW bandstop filters, quarter wavelength monopole antennas, and evanescent-mode cavity resonators are successfully demonstrated as test vehicles. It has been shown the MTM technique can achieve lower loss and high performance with greater geometrical versatility. The consistency of the fabricated dimensions enables the realization of wideband radiators (up to 21% monopole) and high Q (more than 500) resonators. High-Q reduced-size resonators based on evanescent-mode cavities are developed and characterized. The reduced-size, low-loss resonators are envisioned as narrow-band filters for highly integrated communication packages, or novel wireless resonator sensor applications.

Chapter 5

Metal-Transfer-Molded RF Resonator for Sensor Applications

In addition to the wireless communication systems discussed previously, there is also an increasing need for wireless sensors ranging from medical/clinical research and structural health monitoring, to mission-critical industrial and military applications [86, 87]. Small size, wireless interrogation, and low power requirements will not only make these sensors more convenient for data acquisition and environmental monitoring, but will also open up new applications. Passive wireless sensors that do not require on-board power supplies is a desirable approach to meet the above requirements. System-on-package (SOP) integration of RF components and sensing elements not only meets the requirements of low cost and compact size, but also provides a solution to harsh environment sensor applications, where active circuits or batteries will not work properly. In this chapter, a novel miniature RF airflow sensor based on MTM technology is presented, and wireless interrogation of the sensor is demonstrated.

5.1 RF evanescent-mode cavity resonator as sensing element

5.1.1 Review of RF resonator sensor

RF passive sensors are usually based on resonant circuits, which often include several key components such as a resonator and antenna.

Communication can be established between a passive wireless sensor and reader system in two ways. The first one is called inductive coupling. Inductive coupling operates in the near field, and typically functions in the LF (125 kHz) and HF (13.56 MHz) bands [89]. Most current wireless passive sensors are based on inductive coupling. For example, M. Fonseca and M. G. Allen report a wireless high temperature pressure sensor operating up to 450 °C and up to 5 bars of pressure [90]. The sensor LC circuit is integrated into a LTCC package that contains a sealed embedded cavity with pressure deformable plates. A planar spiral inductor is integrated and embedded into the substrate. A parallel-plate capacitive element is interconnected with the inductive element to form the LC resonator. The capacitor is integrated into the mechanically deformable structure to create a pressure-variable capacitive element. When the environmental hydrostatic pressure surrounding the sensors changes, the plates deflect and bring the electrodes of the capacitor closer or farther apart. In turn, the capacitance change of the system changes the resonance frequency. Therefore, the sensor's self-resonance frequency of the LC circuit is a function of the environmental pressure.

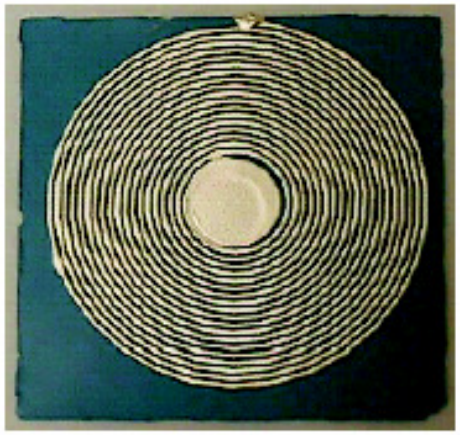

Figure 5.1 Ceramic pressure sensor with silver screen printed conductors [75]

The second method for wireless sensor communication is modulated backscatter coupling. Similar to passive RFID technologies, backscatter operates at UHF (>100 MHz) or higher frequency bands. When the sensor is introduced to the read field, the sensor antenna gathers enough power to activate, and returns an echo. The echo is modulated by the sensor resonator and reflected with enough power to be recognized by the reader antenna. RF wireless sensors based on backscattering have been reported recently for embedded wireless strain monitoring [90]. The strain sensor is a conducting coaxial electromagnetic cavity that is embedded in the structure in which strain is measured. The cavity exhibits resonance for electrical wavelengths two times the cavity length. Changes in the structure's dimensions reflect in the shift of the resonant frequency of the cavity. A loop antenna is connected with the cavity as a sensor antenna. As long as the unstrained resonant frequency is known, the strain can be determined with the same accuracy as the resonant frequency can be measured. One advantage of this approach is that RF signals can be generated with very high accuracy and stability, and transmitted to the far field. Figure 5.2 shows the reported wireless strain sensor using metal RF cavity resonators (operating in 2.45GHz) [90]. The sensor is machined out of brass or aluminum. For TEM_{001} mode,

$$\Delta f_r = -f_{unstrained}\varepsilon \tag{5.1}$$

where $\varepsilon = \frac{\Delta l}{l}$. The sensor is operating at 2.45GHz, so the sensitivity is $2.45 KHz/\mu\varepsilon$ (2.45KHz per microstrain).

Table 5.1 shows a comparison of these two types of wireless passive sensor based on LC circuit and waveguide resonator. Wireless sensors based on LC circuit are compact in size and can be fabricated on flexible substrate, however, the sensitivity is limited by the relatively low quality factor, and the interrogation distance is typically limited within one wavelength. Wireless sensors based on cavity or waveguide resonators have a high quality factor and longer interrogation distance, however are typically bulky and costly to fabricate. They also typically require an external antenna for wireless interrogation. Miniature and high-Q resonator sensor is highly desired for wireless sensor applications.

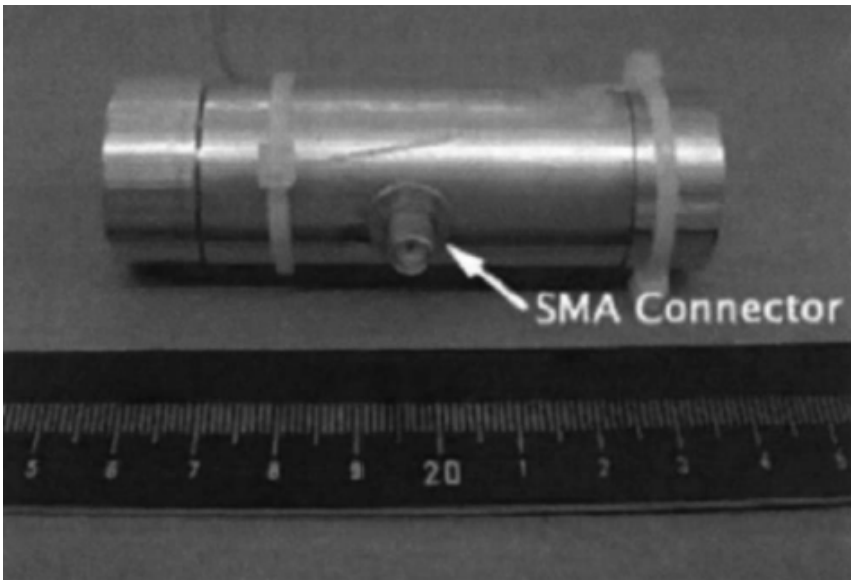

Figure 5.2 Photograph of coaxial cavity sensor made from aluminum [90]

Molded polymer-core RF components are very promising for passive wireless sensor applications, especially in lower-cost scenarios. The polymer components have low cost, low weight and ease of packaging. These molded components are also very useful for disposable or implantable applications. This chapter proposes a novel sensor

concept based on an evanescent-mode cavity resonator, and demonstrates its applications to airflow measurement. Compared with conventional waveguide RF resonator sensors, the sensor based on an evanescent-mode cavity resonator has much higher sensitivity due to the phenomenon that most of the electrical field is confined within the air gap. In addition, the physical size of the evanescent-mode cavity is much smaller than conventional cavity or waveguide, so the sensor size can be greatly reduced. A CPW feeding structure on the bottom of the cavity is utilized to excite the cavity resonance. The simplicity of the feeding structures enables easy integration of the sensing elements. Metal-transfer molding (MTM) process-based MEMS technology is adopted for the realization of the cavity structures to achieve a low-cost batch fabrication. The sensing elements are fabricated separately and integrated with the cavity resonator by a simple fixture method.

Table 5.1 Comparison of two types of RF passive wireless sensor based on resonator

	LC Circuit	Waveguide Resonator	Evanescent-mode Cavity Resonator
Frequency	Low (LF and HF)	High (UHF or higher)	High (UHF or higher)
Size	Compact	Bulky	Reduced size
Interrogation distance	Near field	Far field	Far field

Advantages	Simple structure Low profile	Long transmitting range High-Q	Long reading range High Q High sensitivity
Challenges	Low Q Easy to detune Limited reading range	Need external antenna Bulky size Costly fabrication	External antenna

5.1.2 Design Concept

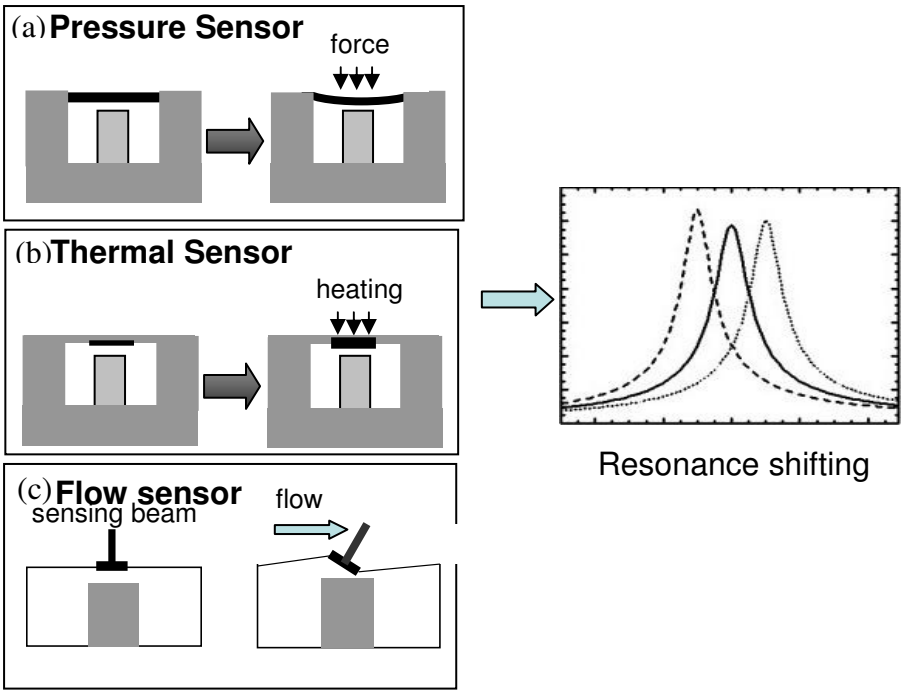

Figure 5.3 Schematic of the evanescent-mode cavity resonator for sensor applications

Highly loaded evanescent-mode cavity resonators have a great potential for RF wireless sensors. When the air gap between the top surfaces of the post and the cavity

becomes close to zero, the resonant frequency drops dramatically with a relatively high Q still maintained. So the resonating is very sensitive to the air gaps, and the high Q enables a high signal-to-noise ratio. This mechanism can be utilized in RF wireless sensor design. Figure 5.3 shows the design concept of evanescent-mode cavity resonator as a sensing element. Figure 5.3(a) shows a concept of pressure/strain sensor with surface displacement, Figure 5.3(b) shows a concept of temperature sensor with a thermal conductor on the top surface, and Figure 5.3(c) shows a flow sensor with a flexible membrane integrated with a sensing beam. The shift of resonant frequency can be measured and transferred to physical parameter changes.

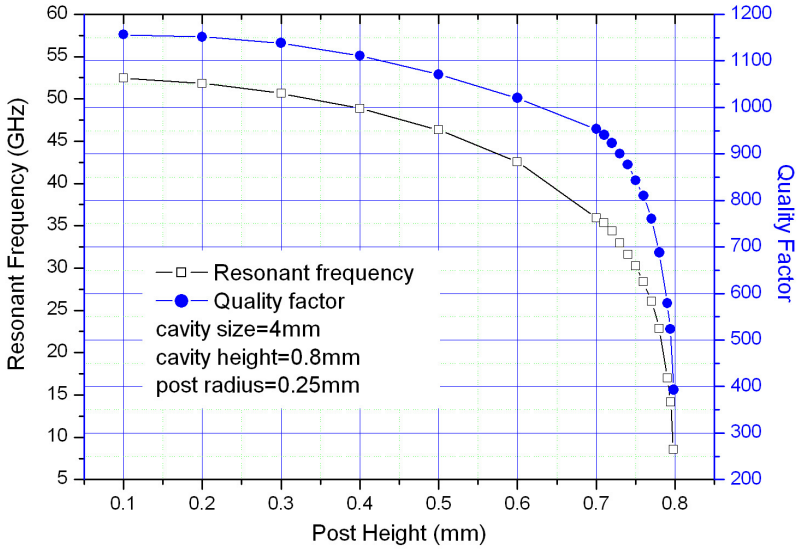

Figure 5.4 Resonant frequency & Q VS. post height for an example evanescent-mode cavity resonator

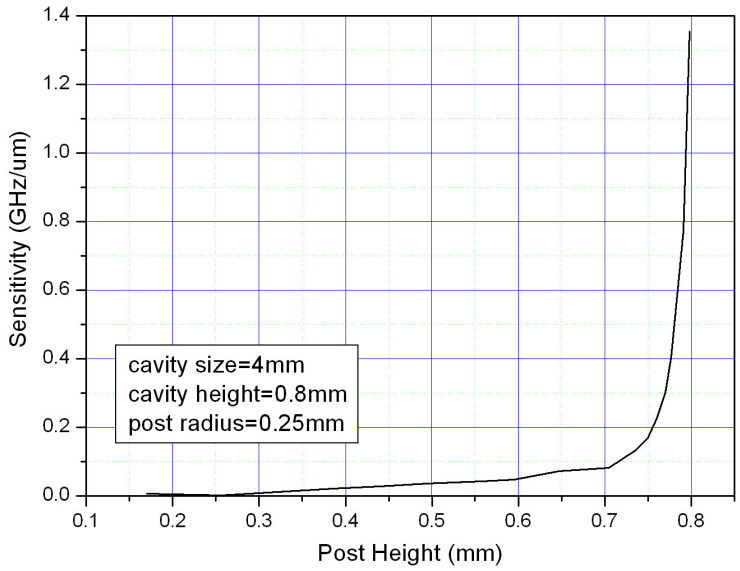

Figure 5.5 Sensitivity vs. post height for an example evanescent-mode cavity resonator

For example, Figure 5.4 shows the resonant frequency and quality factor (Q) versus the post height for a $4mm \times 4mm \times 0.8mm$ rectangular cavity resonator with a capacitive post at diameter of 0.5mm, and by calculating the derivative from the curves, the sensitivity of the resonant frequency versus the post height can be derived (Figure 5.5). When the air gap is 50μm, the resonant frequency shift versus the cavity top surface displacement of 200MHz/μm achieved, while the Q is still more than 850. Using the multi-layer SU-8 fabrication technology discussed in Chapter III, the height difference between the cavity top surface and the post top surface can be achieved precisely to 10μm, which enables a sensitivity of more than 750MHz/μm. Meanwhile, the Q is still more than 400, i.e. the 3dB bandwidth of the resonance is less than 38MHz.

For the regular waveguide sensor with length, l, for a longitudinal dimensional change, Δl, for the dominate resonance mode,

$$\Delta f_r = -f_0 \frac{\Delta l}{l} \tag{5.2}$$

While for an evanescent-mode cavity resonator with an air gap, d, for a dimensional change, Δd, according to the equation (4.5) in chapter 4,

$$\Delta f_r = f_0 \frac{\Delta d}{2d} \tag{5.3}$$

Then:

$$\frac{\Delta f_{evanescent-\mathrm{mod}\,e}}{\Delta f_{conventional}} = \frac{\Delta d/(2d)}{\Delta l/l} = \frac{1}{2}\left(\frac{l}{d}\right)\left(\frac{\Delta d}{\Delta l}\right) \tag{5.4}$$

Since d is limited by the fabrication resolution, while l is limited by the wavelength, d is far smaller than l, i.e. $d << l$. For same dimension changes $\Delta l = \Delta d$, , the shift of resonant frequency for evanescent-mode cavity resonator is far more than that of conventional cavity resonator. Figure 5.6 shows an example comparison of the two types of cavity resonator both operating at 10GHz. The evanescent-mode resonator can be ten times smaller size while a frequency sensitivity of 150~360 times of the regular waveguide resonator liquoring the frequency measurement precision. On the other side, the fabrication of evanescent-mode cavity resonator has a higher accuracy requirement for the micromachining techniques, and the proposed MTM technique has a great potential in the fabrication of such structures.

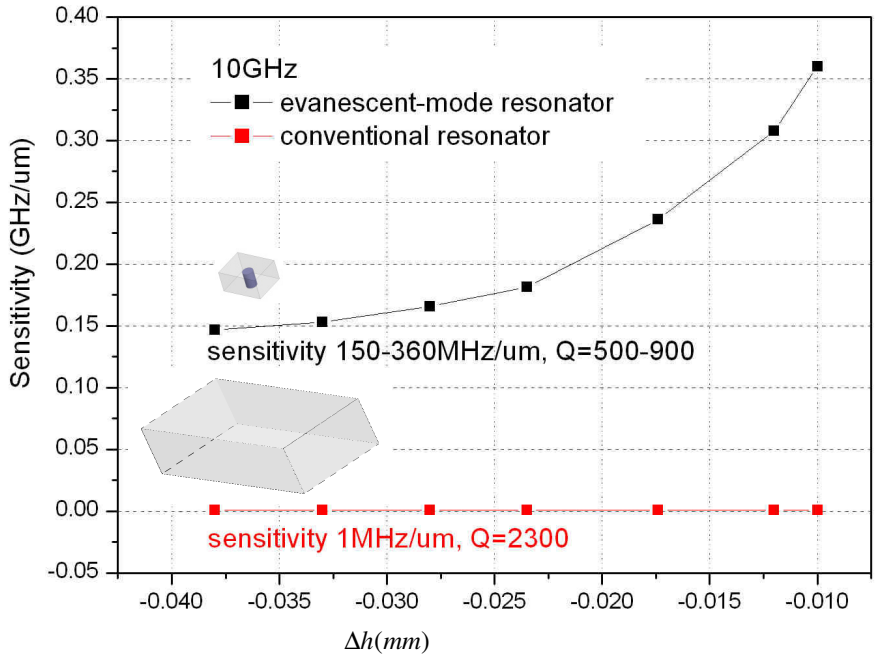

Figure 5.6 Sensitivity vs. dimension for evanescent and conventional cavity resonator

In addition, at a given cavity size, by changing the radius of the capacitive post in the cavity, the resonant frequency of the resonator can be also changed. For example, a resonant frequency versus the post radius (post height and cavity size is given) is shown in Figure 5.7. This mechanism enables the fabrication of an array of the resonators with the same cavity size while operating at difference resonant frequencies.

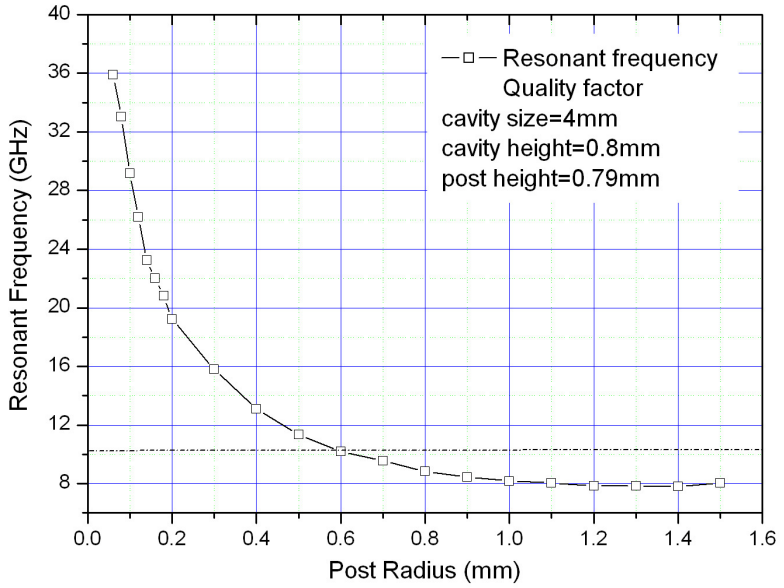

Figure 5.7 Simulated resonant frequency vs. post radius for a given cavity size

5.2 Air-flow Sensor based on RF Evanescent-mode Cavity Resonator

5.21 Design Concept and Sensitivity Analysis

Flow measurement is a necessary task in diverse fields as dynamic aircraft maneuvering, medical instrumentation, environmental monitoring, automotive applications, and process control. Many previous studies have demonstrated the successful application of micro-electro-mechanical- system (MEMS) techniques to the fabrication of a variety of flow sensors, capable of detecting both the flow rate and the flow direction [91-93]. However, few researchers report such flow sensors with the wireless capability that is essential for distributed sensor networks. Evanescent-mode cavity resonators better suit the need for sensor applications, because the size of the evanescent-mode resonator is reduced and the sensitivity to the distance between the capacitive post and the top of the cavity becomes more pronounced. Miniature

evanescent-mode cavity resonator with highly sensitive tunable resonant frequencies has been demonstrated recently [94]. The fabrication of these RF components is usually by surface micromachining or silicon DRIE, and the resonance is excited by aperture coupling through microstrips. However, it is challenging to integrate the sensing element on the top of the cavity due to the complexity of the fabrication. In addition, the feeding structures to excite the resonance are often on the top of the cavity, leaving limited space for the integration of sensing elements.

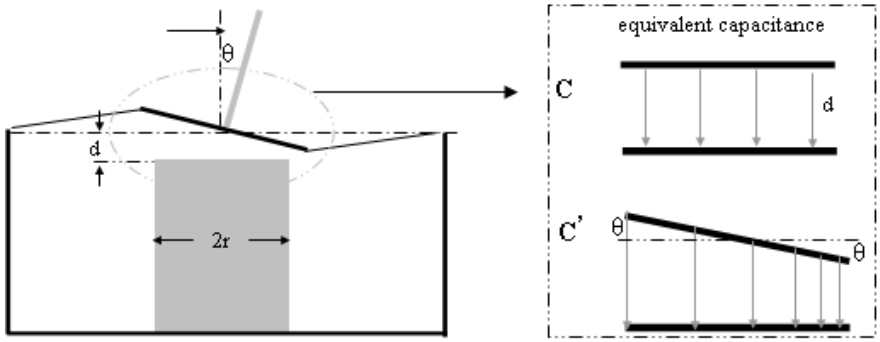

(a)

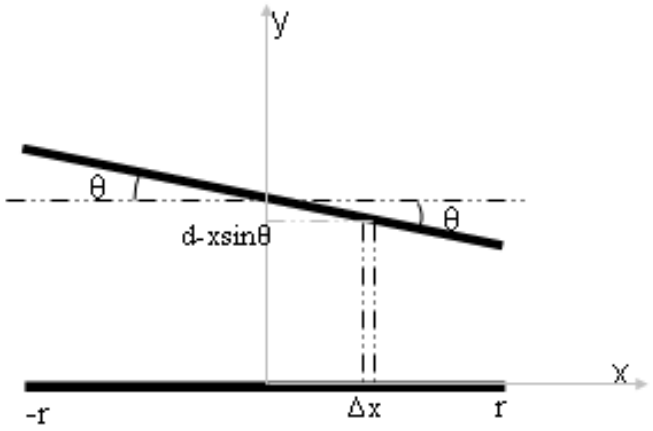

(b)

Figure 5.8 airflow sensor mechanism (a) sensor schematic (b) equivalent capacitance

Figure 5.8(a) shows the operation mechanism of an airflow velocity sensor based on the evanescent-mode cavity resonator. An elastic membrane seals the cavity, and a miniature sensing beam protrudes from the membrane surface and extends into the flow. The beam is deflected by the air flow, changing the capacitance between the cavity and evanescent post top surfaces, thereby altering the resonance frequency of the highly loaded cavity resonator.

A simplified sensitivity analysis can be performed based on the equivalent circuit model described in Chapter 4. As is shown in Figure 5.8(b), for a small beam deflection angle θ ($\sin\theta \approx \theta$), the equivalent capacitance of the resonator can be derived form the integral:

$$C' = \int_{-r}^{r} \varepsilon_0 \frac{\Delta A}{d - x\sin\theta} = \int_{-r}^{r} \frac{\varepsilon_0 l}{d - x\theta} dx \qquad (5.4a)$$

where ΔA is the area of the parallel plate for Δx length, l is average width of the parallel plate, d is the air gap between the top surfaces of the cavity and post, r is the radius of the capacitive post, then:

$$C' = (-\frac{\varepsilon_0 l}{\theta}) \ln(d - x\theta)\Big|_{-r}^{r} \qquad (5.4b)$$

i.e.:

$$C' \approx C \frac{s}{(2\theta)} \ln(\frac{s+\theta}{s-\theta}) \qquad (5.5)$$

where $s = \frac{d}{r}$, then,

$$f_r = f_0 \sqrt{\frac{C}{C'}} = 1/\sqrt{\frac{s}{2\theta} \ln(\frac{s+\theta}{s-\theta})} \qquad (5.6)$$

where C and C' are the equivalent capacitance of the resonator before and after the beam deviation; f_0 and f_r are the resonant frequencies before and after shifting. This model only applies for a small deflection angle and air gap. The accurate resonant frequency shift can be predicted by the using full-wave eigen-value analysis.

Figure 5.9(a) shows the design schematic of a 2×2 airflow sensor array based on an evanescent-mode cavity resonator. The sensor comprises two main parts including the RF structure (cavity and CPW) and mechanical structure (membrane and sensing beam). Elastomer polydimethylsiloxane (PDMS) is utilized for the membrane structure and is coated with a thin layer (3μm) of copper for electrical functionality. Figure 5.9(b) shows the cross sectional view of the sensor. The sensitivity of the sensor can be expressed by following equation:

$$S = \frac{\Delta f_r}{\Delta v_{airflow}} = \frac{\Delta f_r}{\Delta \theta_{beam}} \bullet \frac{\Delta \theta_{beam}}{\Delta v_{airflow}} = S_{RF} \bullet S_{mechanical} \tag{5.8}$$

$$S_{RF} \equiv \frac{\Delta f_r}{\Delta \theta_{beam}} \tag{5.9}$$

$$S_{mechanical} \equiv \frac{\Delta \theta_{beam}}{\Delta v_{airflow}} \tag{5.10}$$

In accordance with equations 5.8 to 5.10, the sensitivity of the sensor is composed of two parts: RF sensitivity, which is determined by the cavity physical design; and mechanical sensitivity, which is determined by the mechanical properties of the elastic

membrane and beam structures. Each of these can be optimized independently depending on the application space. The mechanical and RF portions of the sensor are fabricated separately and assembled by a small fixture. This assembly method is particularly useful for sensor prototyping and characterization. In actual sensor production, a bonding process can utilized instead of the fixture to minimize the size and maximize manufacturing through-put.

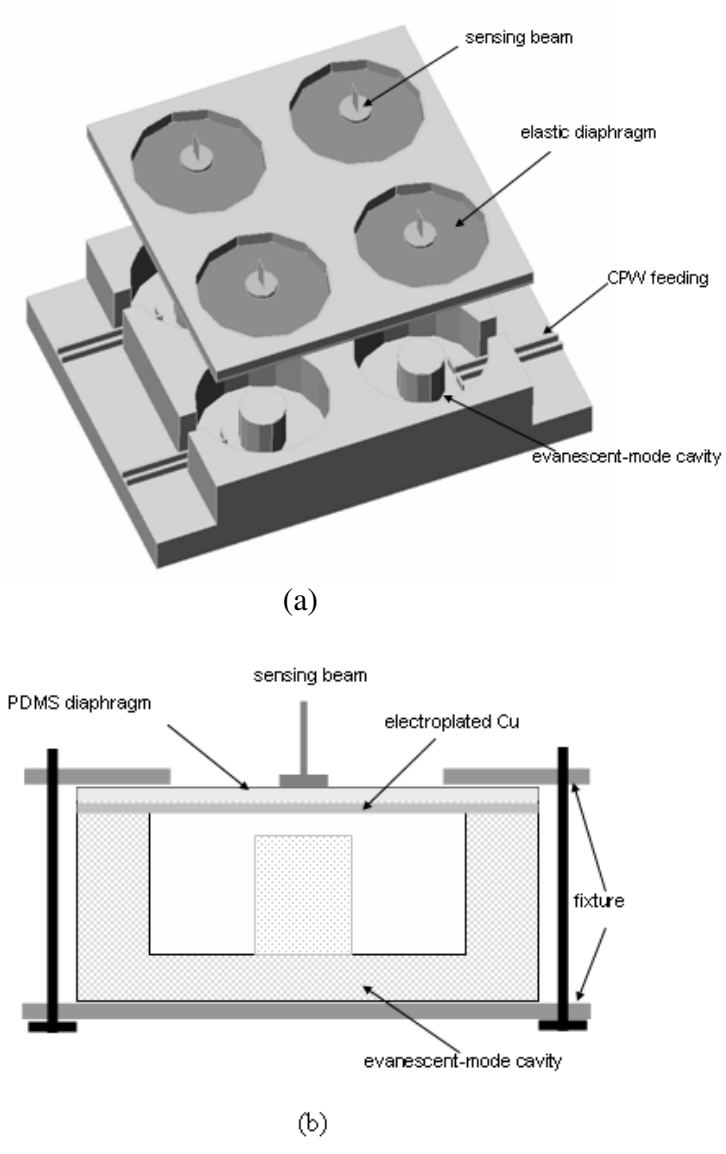

Figure 5.9 Design schematic of the airflow sensor array
(a) lateral view (b) cross-sectional view

Table 5.2 shows the design parameters for the cavity resonators. Two different size cavities are designed and fabricated. They are designed to operate at different resonant frequencies of 21.4GHz and 13.9GHz, respectively.

Table 5.2 Design parameters of cavity resonators for airflow measurement

	Cavity Radius	Cavity Height	Post Radius	Post height
Cavity Design I	2.50mm	1.00mm	1.00mm	0.85mm
Cavity Design II	2.00mm	2.50mm	0.75mm	2.40mm

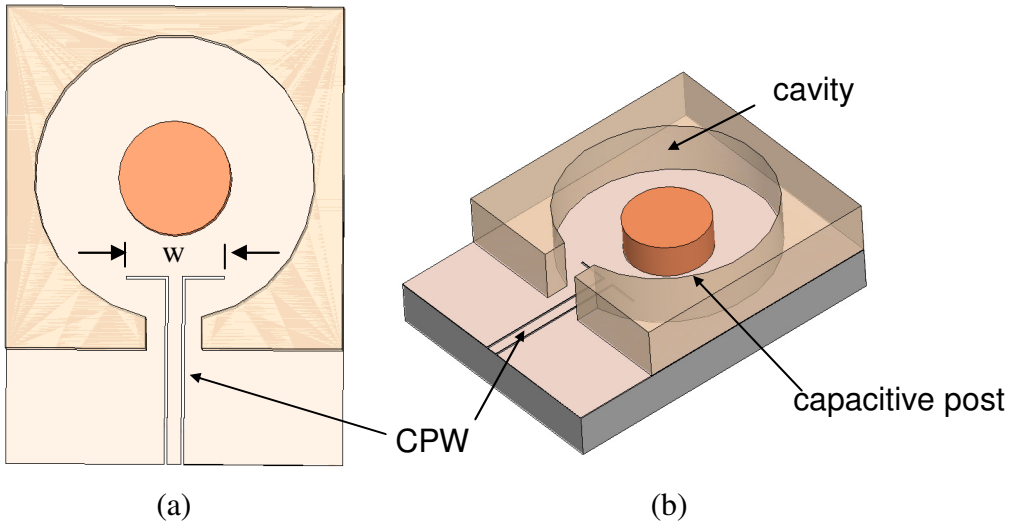

Figure 5.10 Schematic of the CPW-to-cavity transition structure design
(a) top view (b) lateral view

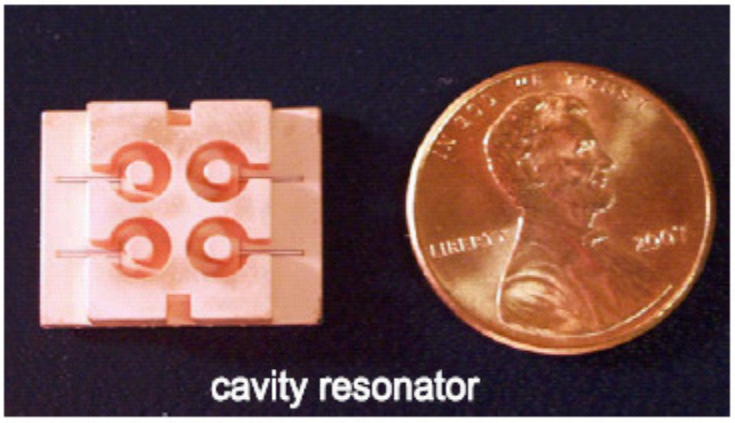

(a)

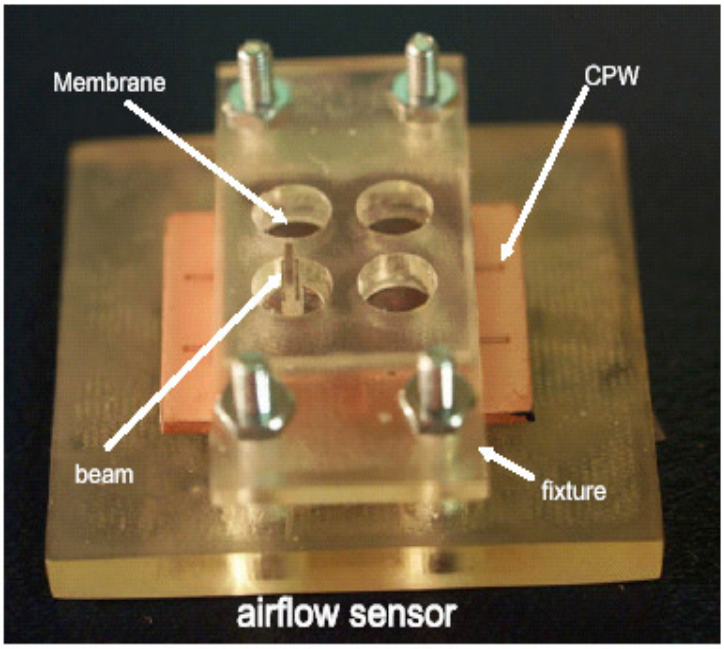

(b)

Figure 5.11 Fabricated airflow sensor array
(a) fabricated evanescent-mode cavity resonator array by MTM process
(b) assembled airflow sensor by fixture

Figure 5.10 shows a schematic view of the proposed evanescent-mode cavity resonator which is composed of the cavity resonator and integrated CPW feeding line. The CPW feeding line critically couples the cavity resonator as described below. The width of the CPW center conductor is 0.18mm, and the slot between the signal and the ground is 0.05mm. The insertion end of the CPW has a split slot structure with an arm of 0.9mm at each end. HFSS full-wave analysis shows that at a certain width of the CPW split-end structure, a critical coupling from the CPW to the evanescent-mode cavity resonator can be achieved, and the S_{11} has a deep notch at the resonant frequency of the evanescent–mode cavity resonator, indicating a strong resonance.

5.2.2 Fabrication

The MTM technique is utilized in fabricating airflow sensor RF cavities. The fabrication process is the same as Figure 4.26 in Chapter 4. The master for molding is made by stereolithography of SLA resin and can be repetitively used for continuous molding processes. A PDMS mold is made by cast and curing the pre-polymer (Dow Corning Sylgard 184). The PDMS mold is then coated with Au/Ti (200nm/30nm) using DC sputter. The metal film is then pre-patterned by using polyester tape right after the deposition process. Since only the metal film on the narrow CPW slots is needed to remove, a small tape bonded on a silicon wafer can be carefully contact the extrusion parts of the PDMS mold, and peeled off after 10 minutes. The SLA epoxy resin is utilized for the molding materials because of the ease of curing by UV light (OAI UV aligner, 5 minutes). After the MTM process, copper electroplating is performed to grow the metal coating with a thickness of above 10μm.

The PDMS membrane is fabricated by spin-coating the pre-polymer (Dow Corning Sylgard 184) on a glass slide by 2000rpm for 40 seconds, and peeling off after curing in $80^{\circ}C$ oven for 2 hours. A 3 minutes O_2 plasma treatment by RIE is then performed on the PDMS membrane to increase the surface adhesion. The PDMS membrane is then coated with Ti/Cu film (30nm/300nm) by DC sputter. Copper electroplating is performed to reinforce the metal coating with a thickness of above 5μm. A plastic fixer is fabricated by stereolithography with alignment holes for screws (Small Parts, inc.). The PDMS membrane is bonded and fixed on the top of the cavity by a fixer. The 3mm long sensing beam is fabricated using stereolithography and bonded on the PDMS membrane by super glue to complete the flow sensor.

Figure 5.11(a) shows the fabricated cavity resonator array using MTM process. The CPW feeding structures extend into the cavities through a small opening on the side of each cavity. Figure 5.11(b) shows the assembled sensor, which was packaged using a plastic fixture.

5.2.3 Characterization and Discussion

RF measurement is performed first to characterize the RF properties of the airflow sensor using an Agilent 8510C network analyzer, in conjunction with an on-wafer probing station. Figure 5.12 shows the experimental setup. The beam is deflected by gently applying a horizontal force, and both the deflecting angle and the resonant frequency are recorded simultaneously. The dynamic range of the sensor is decided by the maximum deflection angle where the top membrane touches the capacitive post inside the cavity.

Figure 5.13 shows the measured S_{11} at different deflection angles for the cavity design I listed in Table 5.2. When the beam is deflected, the effective capacitance increases, and the resonant frequency shifts lower, and a return loss of more than 10dB is observed at the resonance. The sharp frequency selectivity is due to the high-Q nature of the RF cavity resonator. Fig. 5.13(b) shows the measured resonant frequencies as a function of beam deflection angle. Approximately maximum 1.0GHz/degree change is observed from the measurement results, indicating a very high sensitivity achieved by the proposed sensor.

The simulated curve is based on equivalent circuit model of the resonator (Figure 4.22). The air gap d and post radius r are precisely measured using microscope. Full wave analysis is then performed to simulate the resonant frequency f_0. From the equation 5.6, the simulated resonant frequency as a function of the deflection angle can be calculated. As discussed in chapter 4, the air gap (0.15mm) is more than 10% of the cavity height (1mm), so the difference between the measurement and the simulation is due to the inaccuracy of the simplified circuit model.

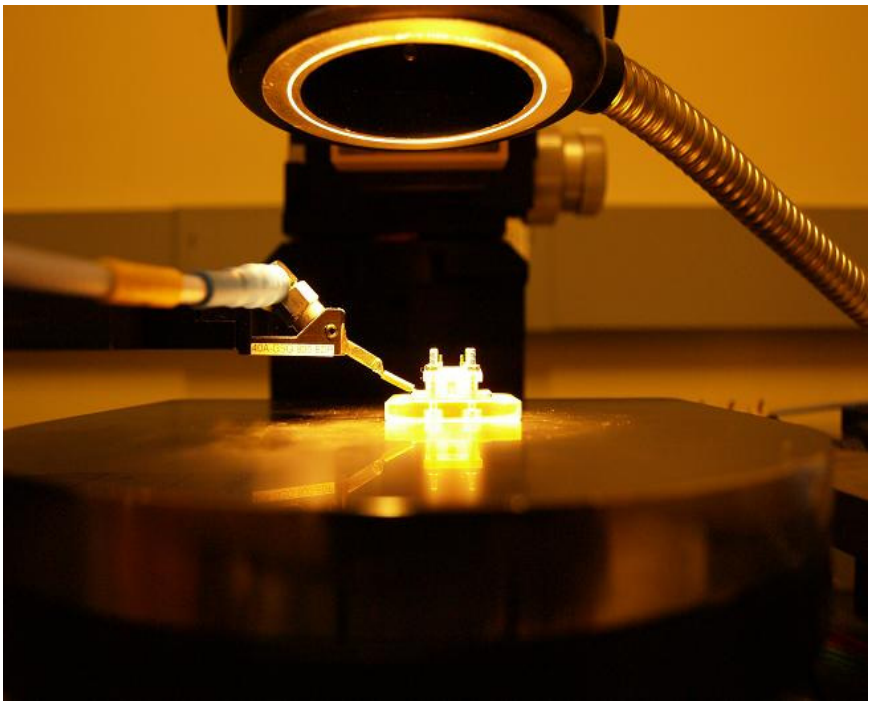

(a)

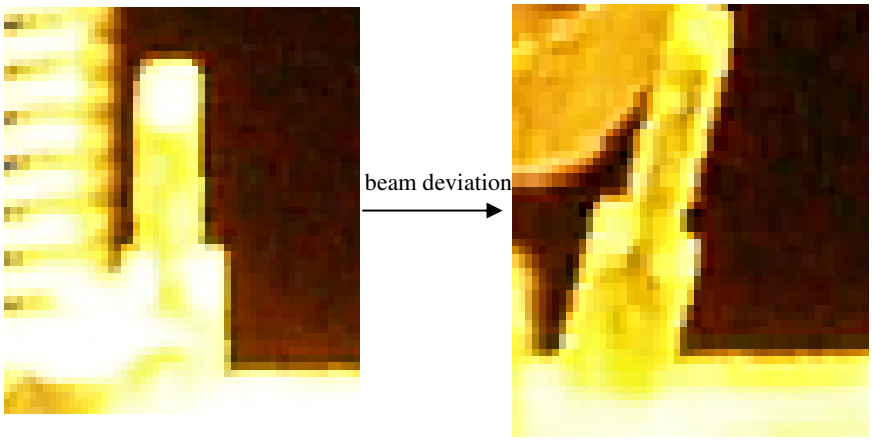

(b)

Figure 5.12 Measurement setup for the beam deflection and resonance frequency (a) measurement setup (b) beam deflection

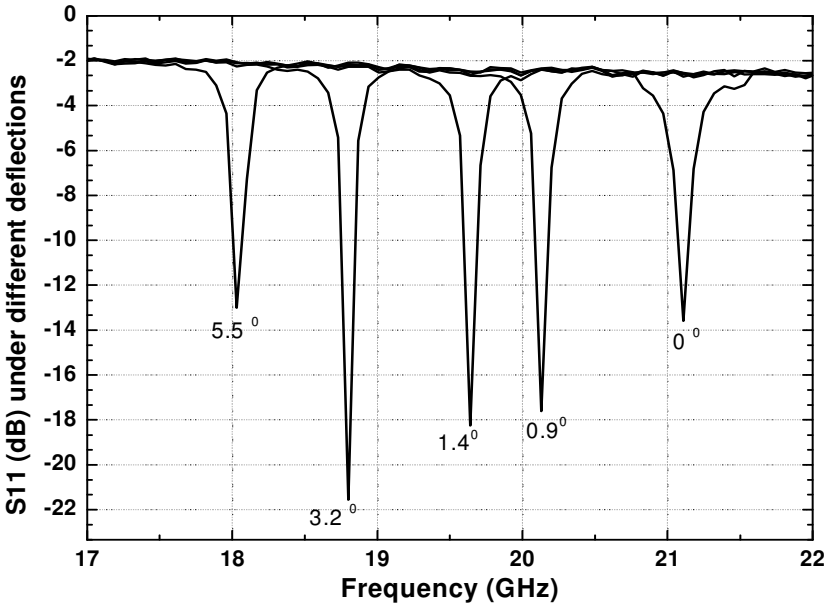

(a)

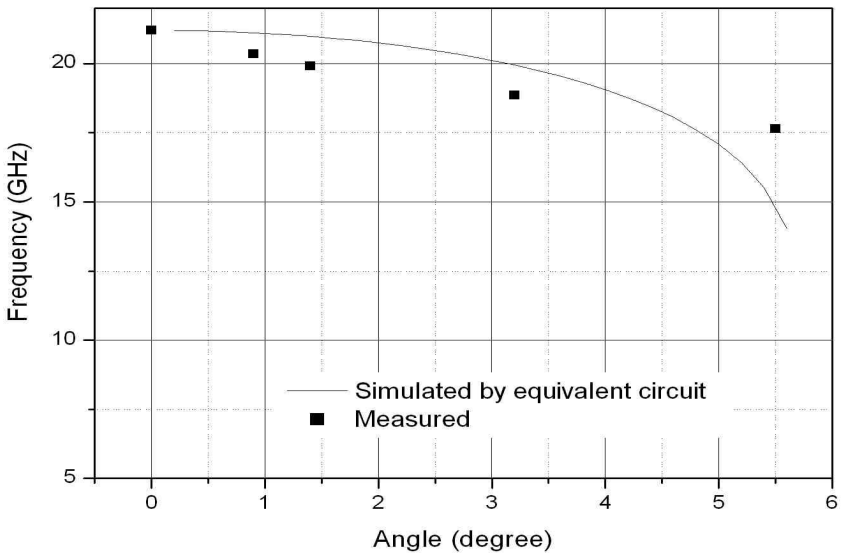

(b)

Figure 5.13 RF measurement results of the airflow sensor design I
(a) measured S11curves at different deflection angles
(b) measured resonance frequency versus beam deflection angle

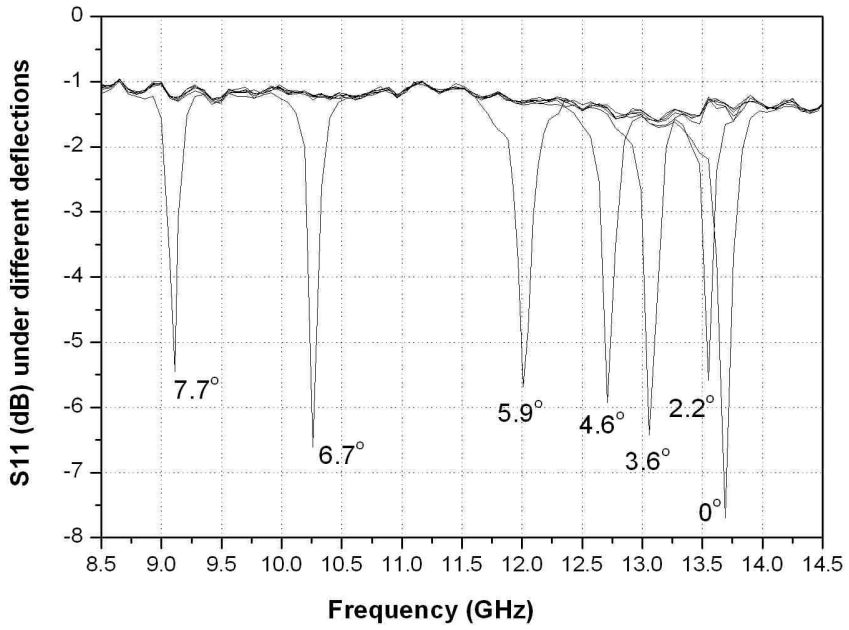

(a)

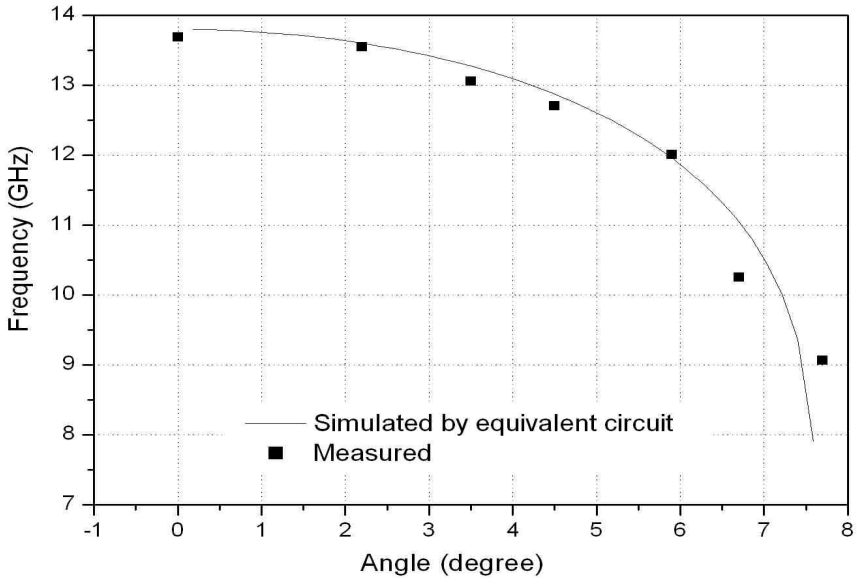

(b)

Figure 5.14 RF measurement results of the airflow sensor design II
(a) measured S11curves at different deflection angles
(b) measured resonance frequency shift versus the beam deflection angles

Figure 5.14 shows the measured S_{11} at different deflection angles for the cavity design II listed in Table 5.2. A return loss of more than 6dB is observed at the resonance. Fig. 5.14(b) shows the measured resonant frequency shift from 13.6GHz to 9GHz as a function of beam deflection angle.

The simulated curve is based on equivalent circuit model of the resonator (Figure 4.22). The air gap d and post radius r are precisely measured using microscope. Full wave analysis is then performed to simulate the resonant frequency f_0. From Equation 5.6, the simulated resonant frequency as a function of the deflection angle can be calculated. As discussed in chapter 4, the air gap (0.10mm) is far less than the 10% of the cavity height (2.5mm), so the equivalent circuit model is very accurate and the measurements agree well with the simulation. The sensitivity varies with the deflection angle, and increases to 1.5GHz/degree when the deflection angle is close to the limit.

Knowledge of the velocity-deformation characteristics of the resonant cavity allows the transduction of flow velocities to readout frequency. The sensor is then put in the wind tunnel to characterize the airflow response. Figure 5.15 shows the experimental setup of the wind tunnel (ScanTEK2000). By adjusting the airflow velocity, the beam deflection angle is recorded. The airflow velocity is measured at the same time using a flow velocity meter. Figure 5.16 shows the measured results in the wind tunnel. The deflection angle has an approximately linear relation to the airflow velocity when the velocity is below 7.8m/s. In our current sensor design, the linear region at small beam deflection angle range is mostly interested. An approximately 1.4m/s per degree change of the beam angle can be observed in the linear region, and according to the RF characteristic of the sensor, an equivalent sensitivity of more than 0.36GHz/(m/s) has

been achieved for the airflow velocity sensing by the evanescent cavity resonator based sensor.

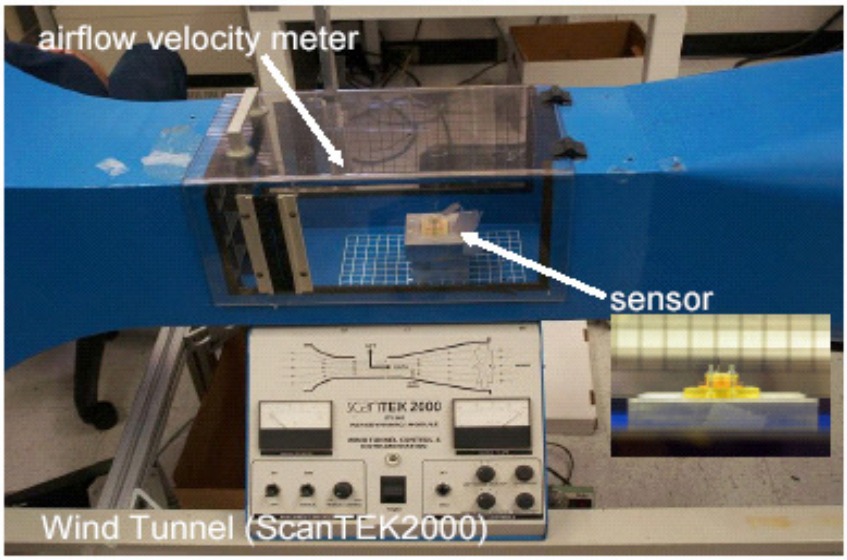

Figure 5.15 Wind tunnel measurement setup of the evanescent-mode cavity airflow sensor

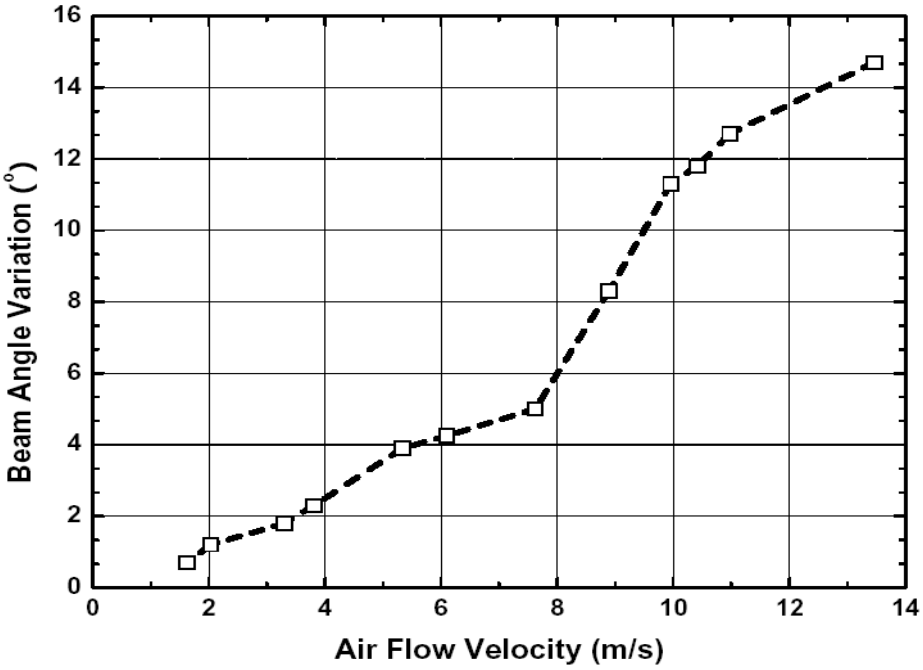

Figure 5.16 Measured deflection angle vs. airflow velocity

5.3 Wireless Interrogation Design

The above resonator sensor measurement results are obtained using probe and cable. However, in many practical applications, wireless interrogation has a large advantage compared to wired sensors. There are usually two types of wireless sensors, active and passive sensors. Active wireless sensors typically have integrated active circuits such as low noise amplifiers (LNA), and an onboard power supply such as a battery, which enable a longer transmitting distance and higher signal-to-noise ratio. However in many applications, such as harsh environment (high temperature or high pressure) or bio implantable systems, either the active components can not work properly, or the onboard batteries are challenging to replace. Furthermore, active components and batteries increase the costs and complexity of the wireless sensor. Thus, it is highly desirable to consider wireless passive sensors with high sensitivity and low cost for these applications. In this section a wireless interrogation method is presented for sensors based on RF evanescent-mode cavity resonators.

5.3.1 Wireless interrogation mechanism

A typical passive wireless sensor has resonator circuits and embedded antennas [89, 90]. Two wireless interrogation mechanisms based on S parameter measurement can be developed for the airflow sensor based on the evanescent-mode cavity resonator. Figure 5.17 shows a one-port wireless interrogation mode.

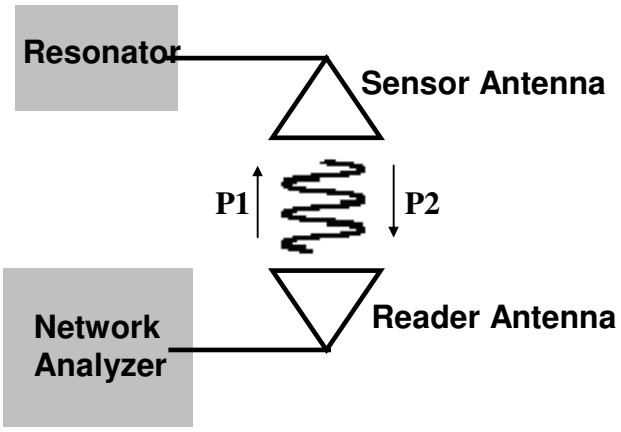

Figure 5.17 Schematic of one-port wireless interrogation mechanism

The cavity resonator is connected to an antenna via a CPW transmission line. The CPW feeding structure is the same as the previously demonstrated airflow sensor. Instead of feeding RF signals by probe, the sensor antenna is utilized to receive and transmit RF signals. A portion of the incoming power P1 from the reader antenna is reflected by the sensor antenna and returned as power P2. The reflection characteristics of the antenna can be influenced by altering the load connected to the antenna. The impedance of the resonator changes with the frequency, and the amplitude of the power P2 reflected from the sensor can thus be modulated (a modulated backscatter). In this work, the return loss S_{11} is wirelessly measured by a network analyzer to characterize the wireless sensor. Similar to the previously demonstrated airflow sensor, there is a deep notch in the S_{11} curves at resonance. The bandwidth is determined by the loaded Q of the resonator.

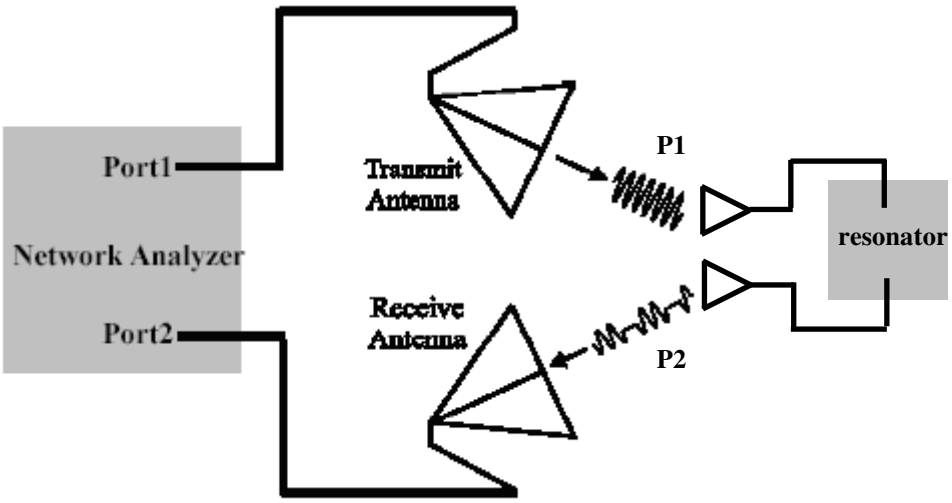

Figure 5.18 Schematic of two-port wireless interrogation mechanism

The second interrogation method is shown in Figure 5.18. The cavity resonator is connected to two antennas. Power P1 is emitted from one of the reader's antennas, a portion of which (after free space attenuation) reaches one of the sensor's antennas. The power P1' is supplied to the antenna connections as RF voltage. The voltage obtained may be sufficient to serve as a power supply and generates RF current through the cavity resonator. The RF signal is then transferred to the other port and drives the second sensor antenna. The insertion loss for this transition can be minimized by careful design of the matching network. The second sensor antenna then emits a RF signal with power of P2, and a portion reaches the second reader antenna of the network analyzer. In this work, S_{21} is measured to characterize the wireless sensor. Similar to a narrowband bandpass (BP) filter, there is a peak at the S_{21} curves at resonance. The bandwidth of the passband is determined by the loaded Q of the resonator.

5.3.2 Embedded Antenna Design

To design the embedded sensor antenna, several parameters and the tradeoffs between them need to be considered: bandwidth, gain, radiation pattern and size. The first consideration for the sensor antenna design is the impedance bandwidth. Wireless interrogation systems usually transmit and receive modulated pulses, which occupy a wide bandwidth. Moreover, the sensor design is based on the resonance frequency shift of a highly-loaded cavity resonator. The antenna bandwidth determines the readable frequency range. For example, for the simulated cavity resonator example in Figure 5.5, the RF sensitivity with respect to a change in the air gap generates up to 350MHz frequency shift per micron, so if the dynamic range of the gap change is 10μm, a minimum impedance bandwidth of 3.5GHz is needed for the sensor antennas, i.e., the bandwidth of the antenna should be more than 35%.

An omni-directional radiation pattern is also preferred for the sensor antenna design because it enables the freedom of the position and angle of the sensor. Gain is another very important consideration for the strength of wireless signals. The reader antennas should have a high gain for interrogation, such as horn antennas, or reflector type antennas. Moreover, it is always an advantage if the wireless sensor and antenna have a compact size.

Based on the above considerations, a quarter-wavelength monopole antenna is an attractive choice of the sensor antenna design due to its wideband frequency characteristic, nearly omni-directional radiation patterns, simple structure and low cost. CPW-fed planar monopole antenna is chosen for the wireless sensor design due to its simplicity and capability for both integration and miniaturization. Figure 5.19 shows the

schematic of a typical ultra-wide-bandwidth (UWB) monopole antenna design [95]. The monopole is fed by a CPW transmission line. Matching of CPW-fed monopole antennas can be improved over the desired frequency band either by changing the height or by changing the tapering angle of the radiator.

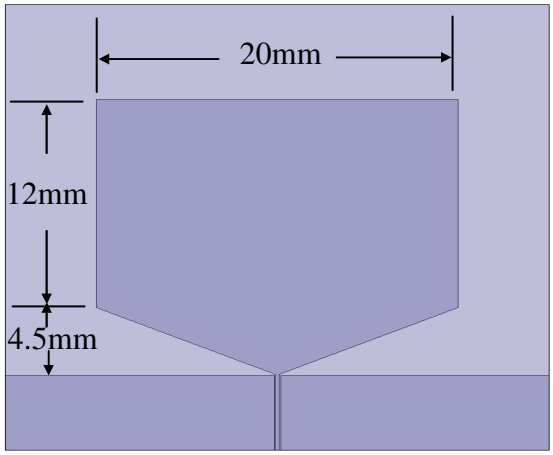

Figure 5.19 Schematic of a CPW-fed monopole antenna with ultra wide bandwidth (UWB)

LCP substrate (ε_r =3.0) with thickness h=0.1mm, and CuClad250 substrate (ε_r =2.5) with thickness h=0.75mm are used for both the sensor and reader antennas. The monopole antenna has a length equal to the quarter wavelength of the lowest frequency. The tapered structure from the grounded plane is designed to achieve ultra-wide bandwidth. By HFSS 10.0 simulations, the optimized taper angle is 66º for wide impedance bandwidth. A simulated S_{11} of the proposed monopole antenna on LCP substrate is shown in Figure 5.20. Although the radiation efficiency is not uniform over this range of 3-20GHz, significant radiation is observed. Figure 5.21 shows the simulated radiation pattern for the proposed antenna at 8GHz. The gain is about 2.84dB, which is

close to the gain of a conventional monopole antenna (3dB). The omni-directional radiation pattern is maintained up to 12GHz for the proposed antenna design.

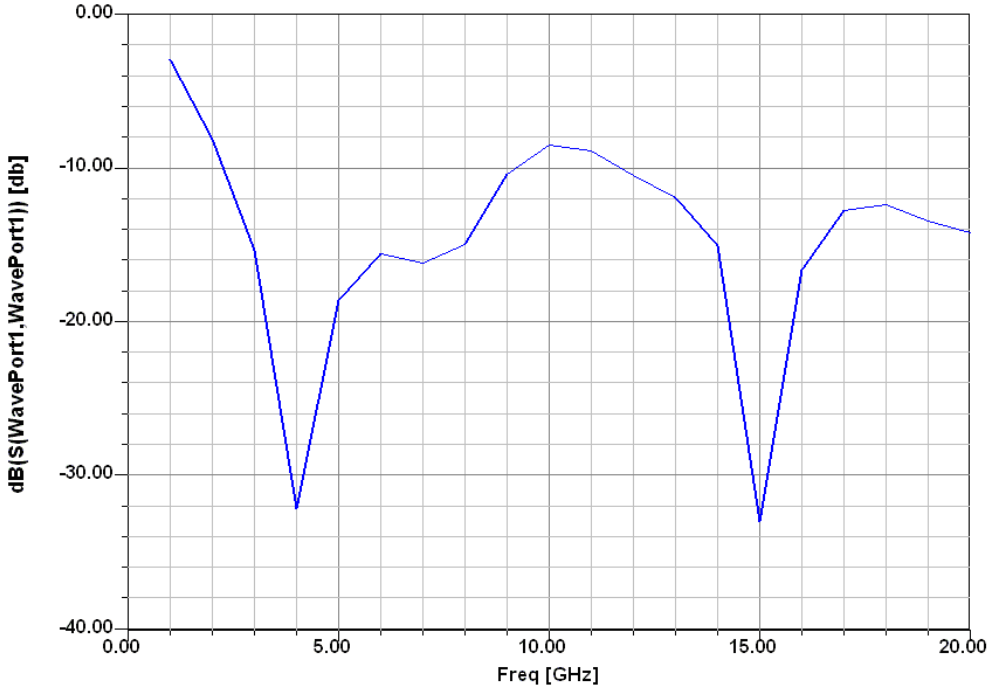

Figure 5.20 Simulated S11 of UWB monopole antenna on LCP substrate

Liquid crystal polymer (LCP) is utilized as the substrate for sensor antennas to minimize the dielectric loss. In addition, LCP is a flexible polymer material, so it works as a tunable surface on the cavity top to change resonant frequency.

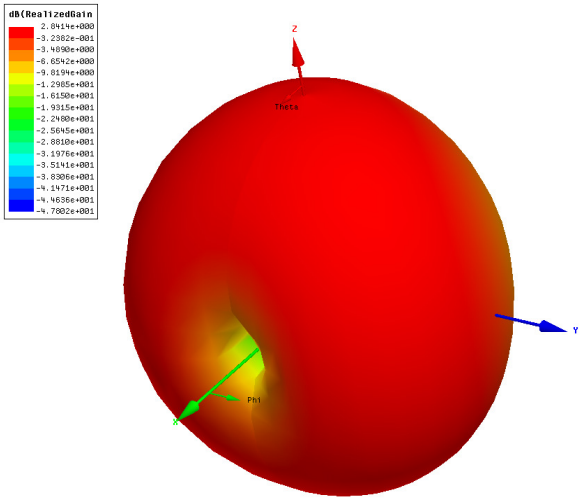

Figure 5.21 Simulated radiation pattern of UWB monopole antenna on LCP

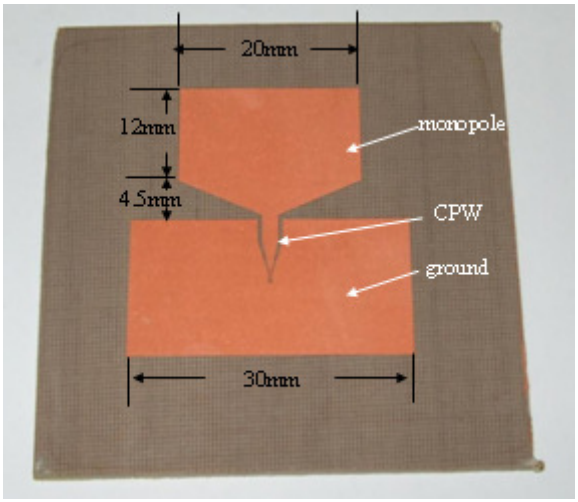

Figure 5.22 Fabricated UWB transmit and receive antennas on CuClad250 substrate

Figure 5.22 shows the fabricated antenna on CuClad250 substrate. The antenna is fabricated by using photolithography (SC1827) and copper etching. The CPW transmission line is design to match the radiation impedance. The fabricated antenna is used as a reader antenna for the interrogation system. When the antenna is placed 2.4mm

above an infinite ground plane, the gain can be reinforced to 8.5dB because of the reflection from the ground plane. Figure 5.23 shows the resultant simulated radiation pattern.

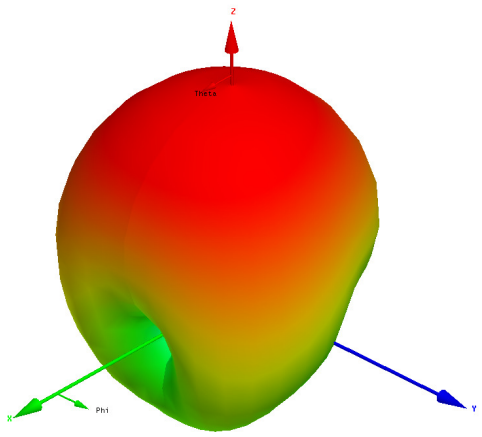

Figure 5.23 Simulated radiation pattern when the reader antenna is 2.4mm above a infinite grounded plane

Figure 5.24(a) shows the experimental setup for the read system. Two elevated reader antennas are placed head to head. A metal sheet as an isolation plane is used to characterize the cross talk. Figure 5.24(b) shows the measured S_{11} with and without isolation for the reader antenna. Because of the presence of the metal stage, which works as a reflection plane for the monopole antenna, the radiation pattern is changed. By adjusting the elevation distance of the antennas, a 10dB wide radiation impedance bandwidth and high gain can be achieved. It also shows that the crosstalk does not change the insertion loss significantly. Figure 5.24(c) shows the measured S_{21} of the reader antennas with or without isolation. The isolation is achieved by placing a metal plane

between the reader antennas. The crosstalk between the two reader antennas without isolation is about -25dB from 7.5GHz to 9.5GHz, and can be reduced further to -40dB with isolation. In our subsequent wireless sensor measurements, no isolation is used.

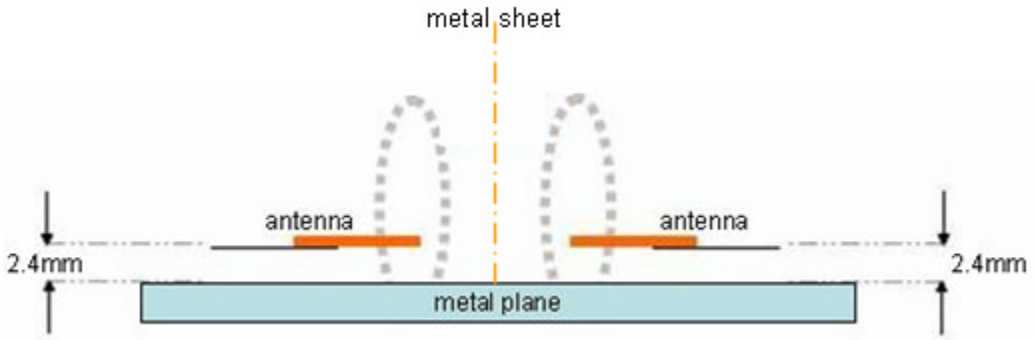

(a)

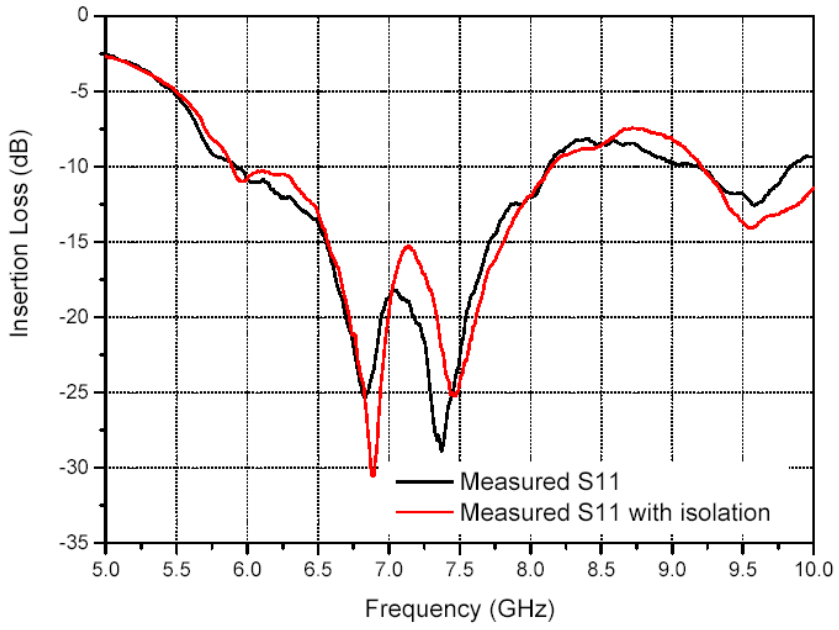

(b)

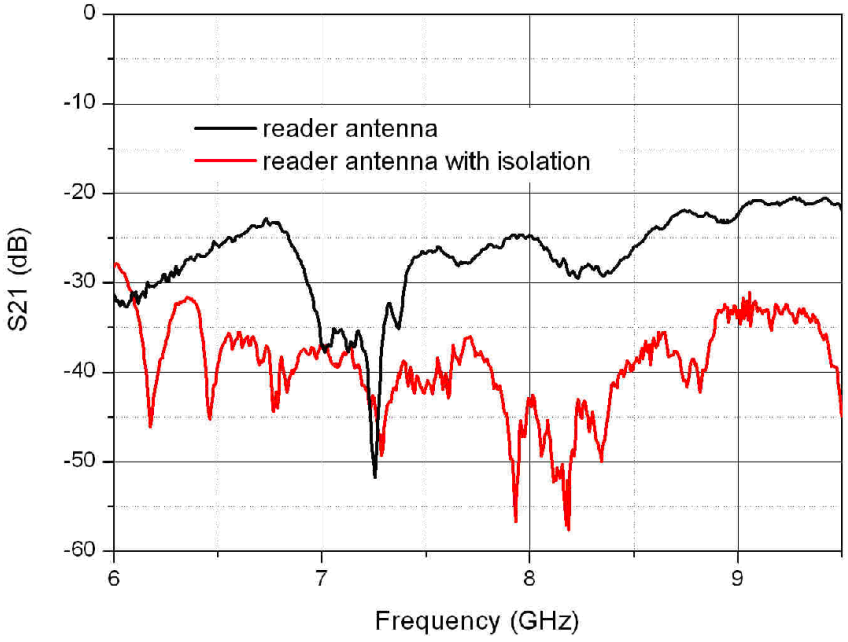

(c)

Figure 5.24 Measured S parameters of the reader antennas
(a) measurement setup schematic
(b) measured S11 with or without isolation
(c) measured S21with or without isolation

5.3.3 Sensor Design

Figure 5.25(a) shows the schematic of the sensor design. The integration of the antenna with the evanescent-mode cavity resonator is achieved by CPW. CPW transmission lines are integrated on the same substrate of antenna, connecting the micromachined cavity resonator and the antenna. RF signals can be received by the antenna and funneled into the cavity. Vice versa, the resonance RF signal can be transmitted from the cavity to the antenna through the CPW. Figure 5.25(b) shows the design schematic of the CPW feeding structures. Similar to the previous CPW fed cavity resonator, a critical coupling from the CPW to the cavity resonator can be achieved by

optimizing the design of the CPW insertion structures. By adjusting the length of the CPW spare-end, the magnetic field is coupled into the cavity at resonance.

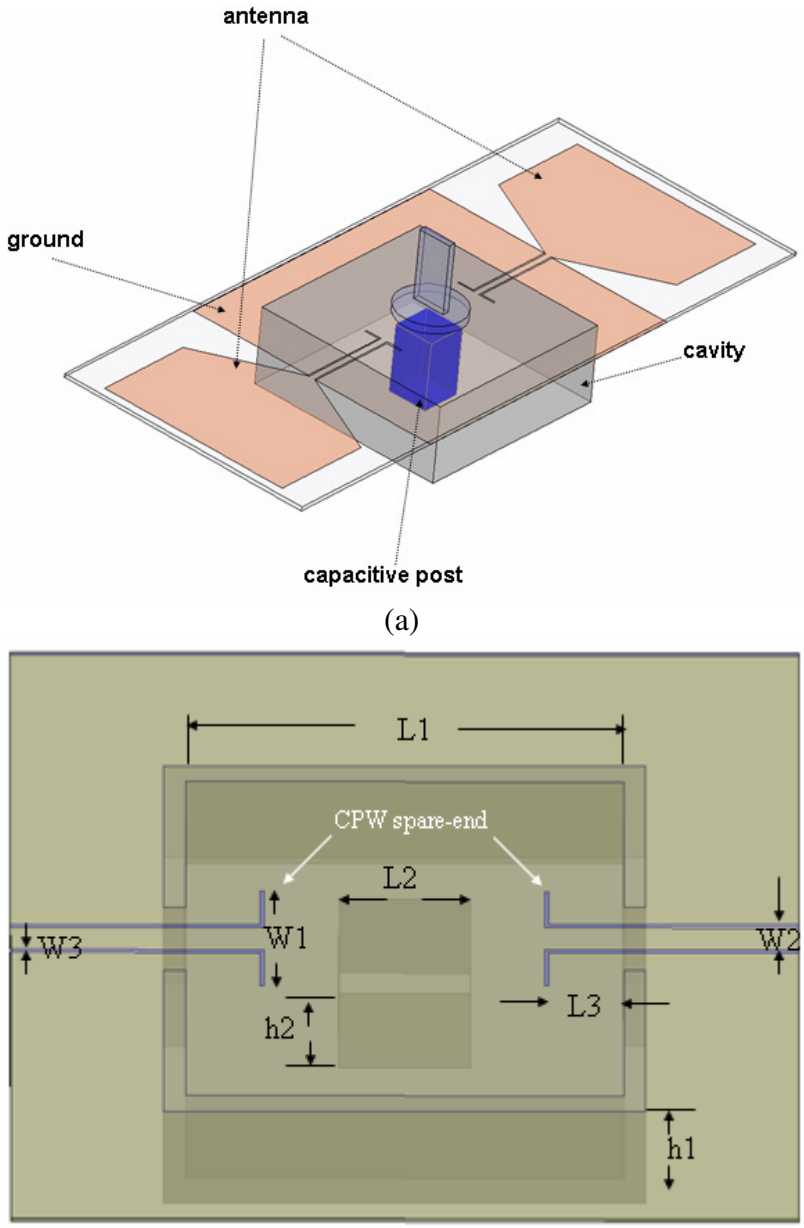

Figure 5.25 Design schematic of the wireless cavity resonator sensor
(a) sensor schematic (b) CPW feeding structure schematic

Table 5.3 shows the design parameters of the evanescent-mode cavity resonator for the wireless sensor in this work. The designed resonance frequency is about 8.9GHz.

Table 5.3 Design parameters of the evanescent-mode cavity resonator for wireless interrogation

L_1	L_2	h_1	h_2
Width of cavity	Width of post	Height of cavity	Height of post
10.00mm	3.00mm	2.70mm	2.44mm

HFSS full wave analysis is performed to find the optimized parameter set for Figure 5.25(b). For example, Figure 5.26 shows the simulated S_{11} and S_{21} for different width of the CPW spare end (W_1). By changing the CPW configuration, the frequency of the sensor shifts slightly because of external loading, as well as the loaded Q and insertion loss at resonance. In this work, width of CPW end (W_1) is chosen to be 3mm as a tradeoff between the loaded Q and insertion loss. By HFSS full wave analysis, the optimized parameters of CPW feeding network design are shown in Table 5.4.

Table 5.4 Design parameters of the coplanar waveguide feeding structure for wireless interrogation

W_1	W_2	W_3	L_3
Spare-end width	Center width	Slot width	Insertion length
3.00mm	0.70mm	0.10mm	3.63mm

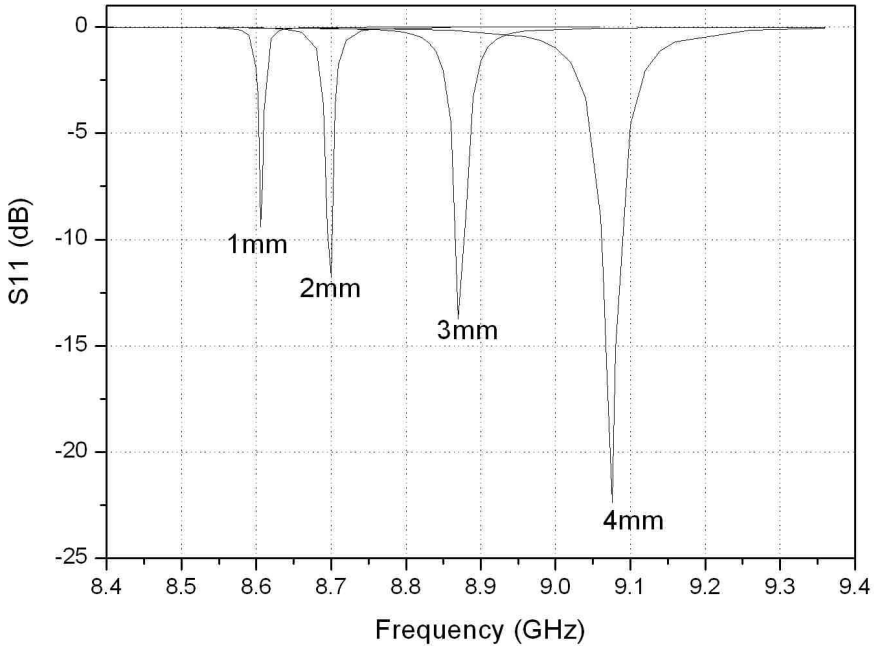

(a)

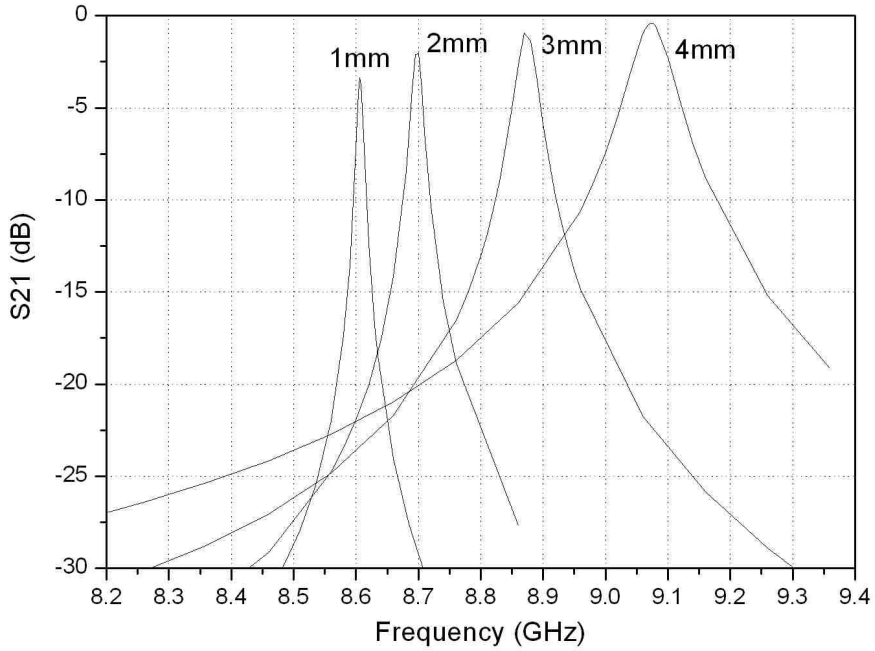

(b)

Figure 5.26 Simulated S parameters for different CPW end width (W1) (a) S_{11} (b) S_{21}

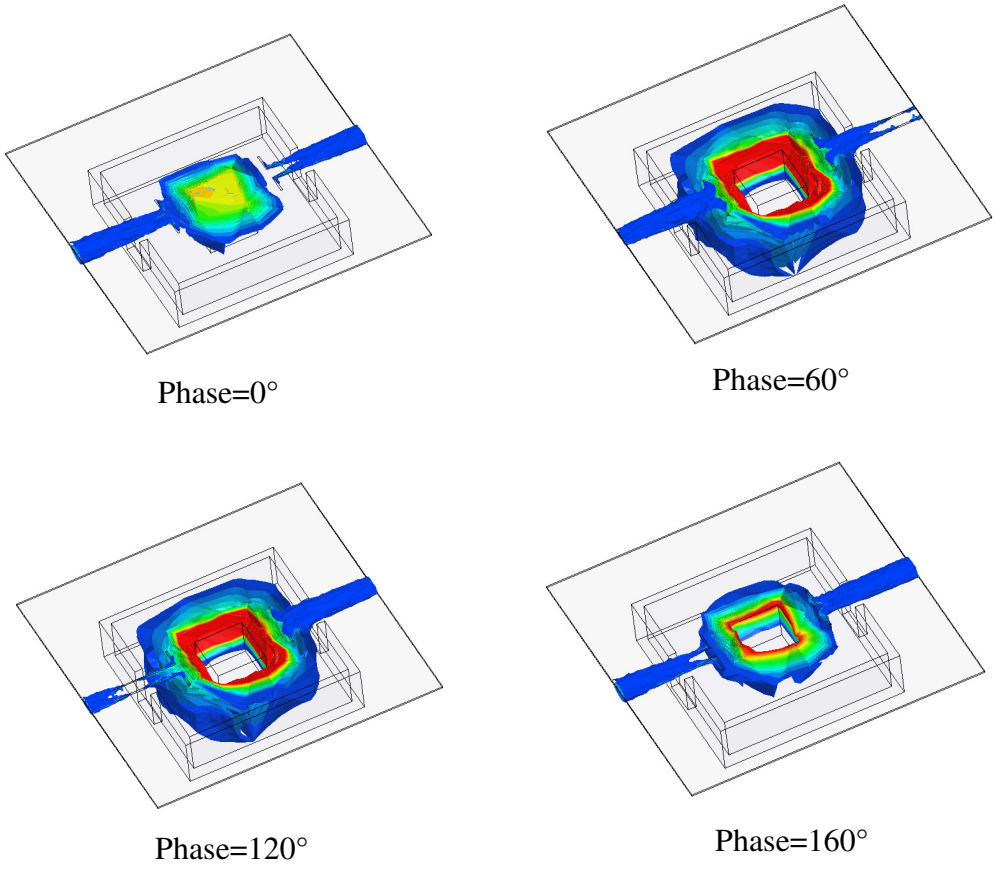

Figure 5.27 Simulated E-field transition as a function of phase

Figure 5.27 shows the simulated signal transition from one port of the resonator to the other port at difference signal phases. The simulation shows that the proposed CPW structure enables a low loss transition at resonance. Figure 5.28 shows the simulated S parameters of the cavity resonator and CPW designs based on Table 5.2 and Table 5.3. The resonant frequency of the cavity resonator is at 8.6GHz. The substrate is LCP with ε_r=3.1, and δ=0.002. A narrow bandwidth of 0.58% can be achieved due to the high Q nature of the cavity resonator. The insertion loss in the pass band is 0.91dB, so the transition loss inside the cavity is very low.

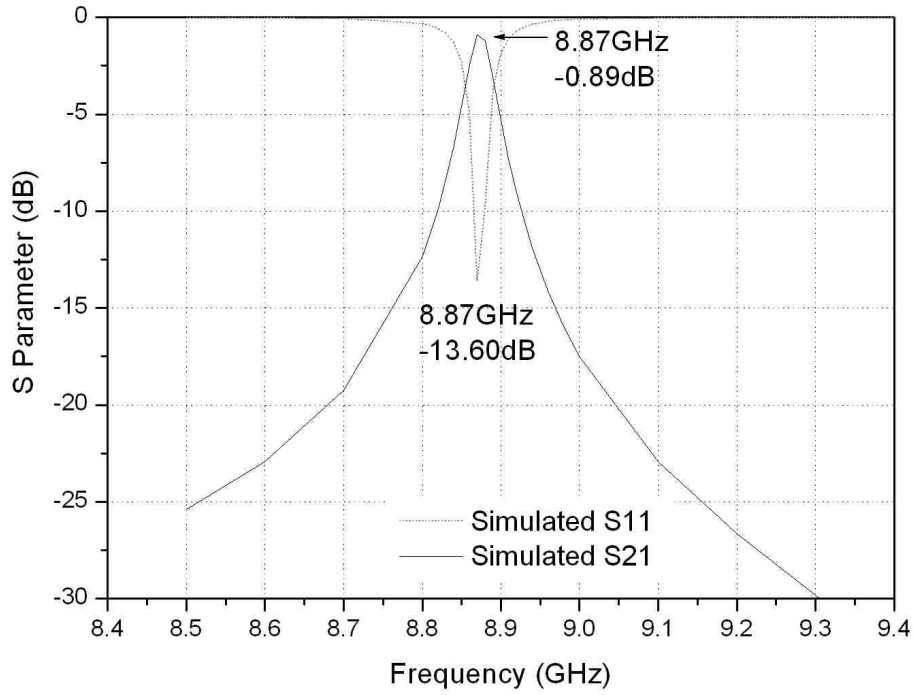

Figure 5.28 Simulated CPW transition for a rectangular cavity resonator

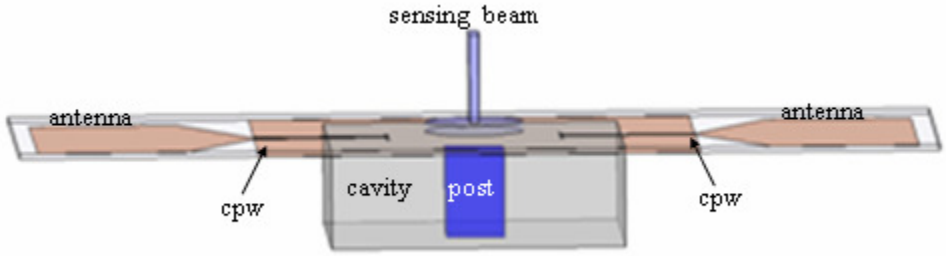

Figure 5.29 Schematic of the wireless passive airflow sensor design

The CPW transmission line is designed to match the impedance of the antenna and the resonator. Figure 5.29 shows the final design of the wireless passive sensor for

airflow or displacement measurement. The CPW transmission line is on the top of the cavity, and at the same substrate with the antennas.

Figure 5.30 shows the fabricated evanescent-mode resonator by MTM process. The master structures are fabricated by using stereolithography. Then a MTM process is performed to make the molded cavities by UV curable SLA epoxy resin. The molded cavities are then coated with above 10μm copper by electroplating. The dimensions are listed in Table 5.3, and the designed resonant frequency is 8.9GHz. Figure 5.31 shows the fabricated sensor antenna with CPW transition structures on LCP substrate. Both the resonator and sensor antenna have small pinholes for alignment, and can be assembled by fixture for ease of integration and testing. Figure 5.32 shows fabricated wireless passive airflow sensor for testing.

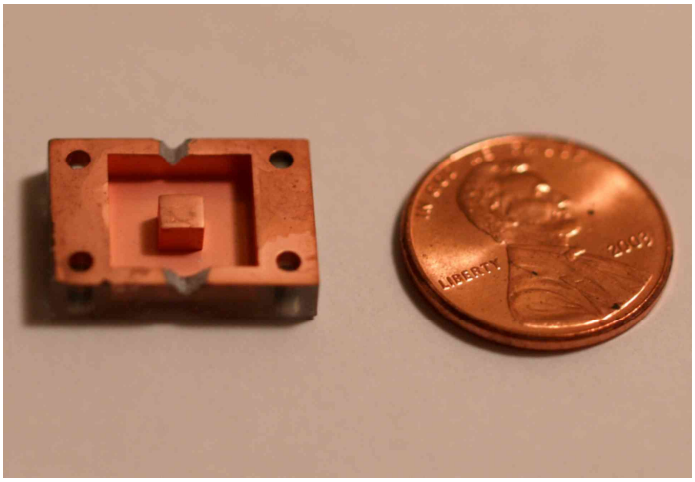

Figure 5.30 Fabricated cavity resonator for wireless interrogation testing

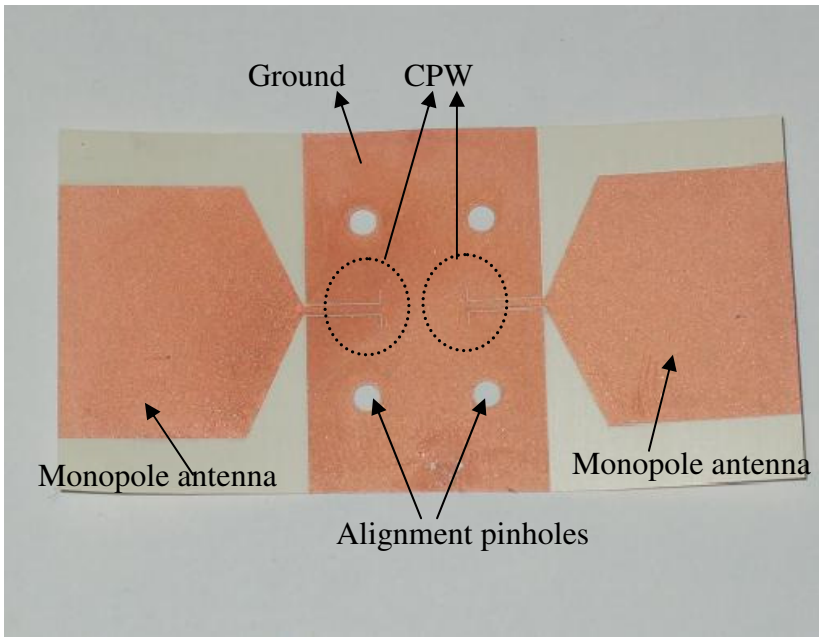

Figure 5.31 Fabricated embedded UWB monopole antenna and CPW transition structure on LCP

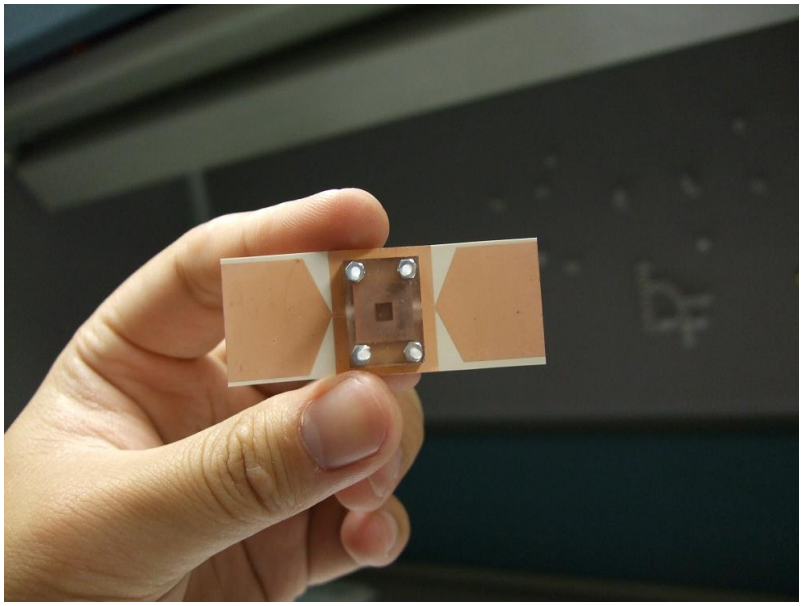

Figure 5.32 Fabricated wireless passive airflow resonator

5.3.4 Wireless Measurement Results

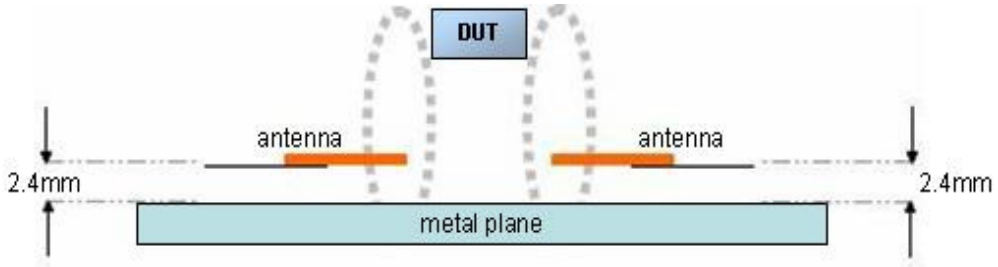

(a) Schematic of wireless measurement

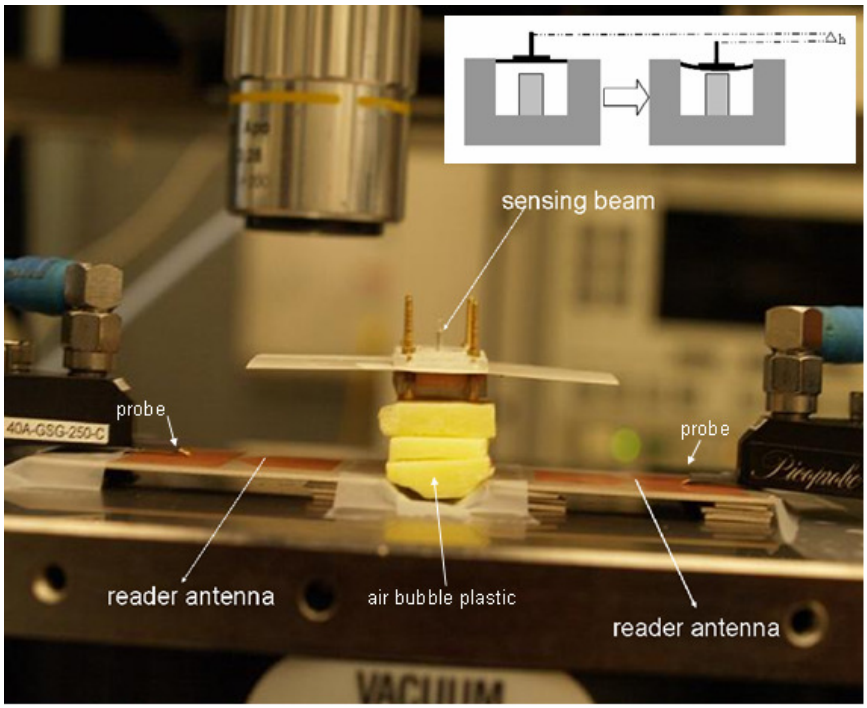

(b) Wireless measurement experimental setup

Figure 5.33 Wireless interrogation measurement setup with difference reading distances

Figure 5.33(a) shows the schematic of the wireless measurements. Two reader antennas are put head to head on the stage, and probes with $250\mu m$ pitch are used to feed the RF signals. Figure 5.23 (b) shows the wireless interrogation setup. The sensor is placed above the reader antennas by using air bubble plastic frame, and the vertical distance between the sensor and reader antennas are from 8mm to 20mm. The air bubble plastic has a dielectric constant close to that of air, so it does not disturb the field. There is a null in the center of the reader antenna's radiation pattern, so the two reader antennas are placed head to head to reduce the cross talk. A force in normal direction is applied to the sensing beam to change the resonance frequency during the experiment, and S parameters are recorded by network analyzer 8510C.

When there is zero force on the beam, the measured S parameters are shown in Figure 5.34. The S_{11} measurements are based on the one-port interrogation mechanism, and a deep notch at the resonant frequency of about 8.9Ghz is observed. The S_{11} curve shows a more than 9dB insertion loss at the resonant frequency when the antenna-to-sensor distance is 6mm, while the insertion loss decreases to 2.5dB when the distance is 12mm. The S_{12} and S_{21} also show a peak at the resonant frequency, which is based on the two-port wireless interrogation mechanism. The RF signal is transmitted from one antenna to the other. And more than 5dB signal to noise ratio is observed, which is in excellent agreement with the high-Q nature of the resonator.

Figure 5.35 to 5.37 shows the measured S parameter results for the wireless sensor with beam vertical displacements. The displacement is applied by using a tape to generate a vertical force on the beam. The distance between the sensor and the reader antenna varies from about 8mm to 21mm. Figure 5.38 and Figure 5.39 show the resonant

frequency shift due to the beam displacement when the sensor is 12mm above the reader antennas. The resonance can be detected in both the S11 and S21 curves. The displacement of the beam and the resonance frequencies are listed in table 5.5. Table 5.5 and Figure 5.40 show the measured curve of the resonant frequency versus the vertical displacement of the beam. The simulated curve is calculated by using HFSS full-wave eigen-mode analysis.

Table 5.5 Measured displacement and resonant frequencies

Displacement	0.00mm	0.08mm	0.11mm	0.14mm
Resonant Frequency	8.85GHz	8.17GHz	7.72GHz	7.16GHz

Because the RF signal decays quickly in space, and the network analyzer only has less than 1mW power, the interrogation distance is limited in the near field. However, with the help of low noise amplifier (LNA), the interrogation distance can be greatly increased.

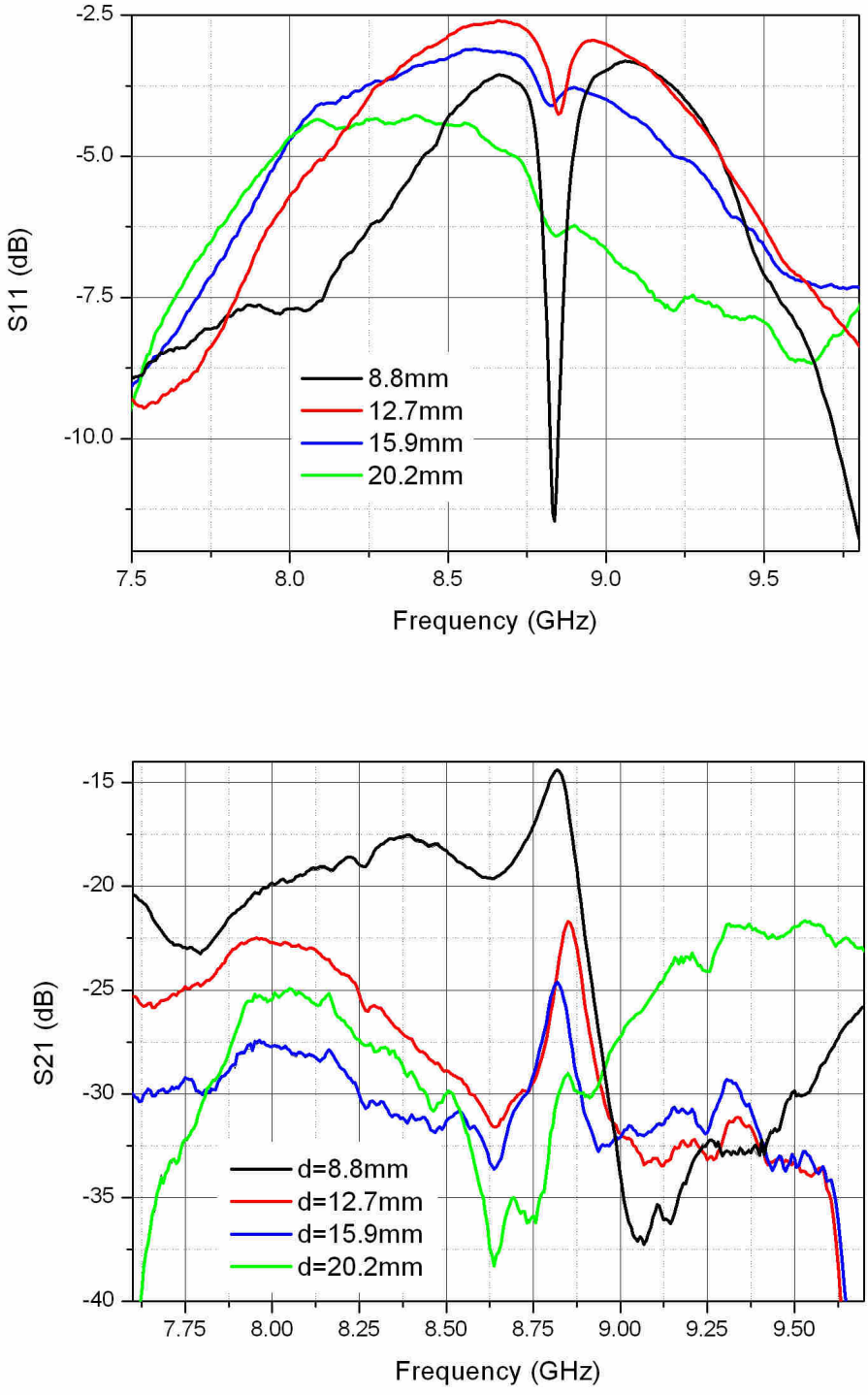

Figure 5.34 Measured S11 and S21 for the sensor beam of zero displacement

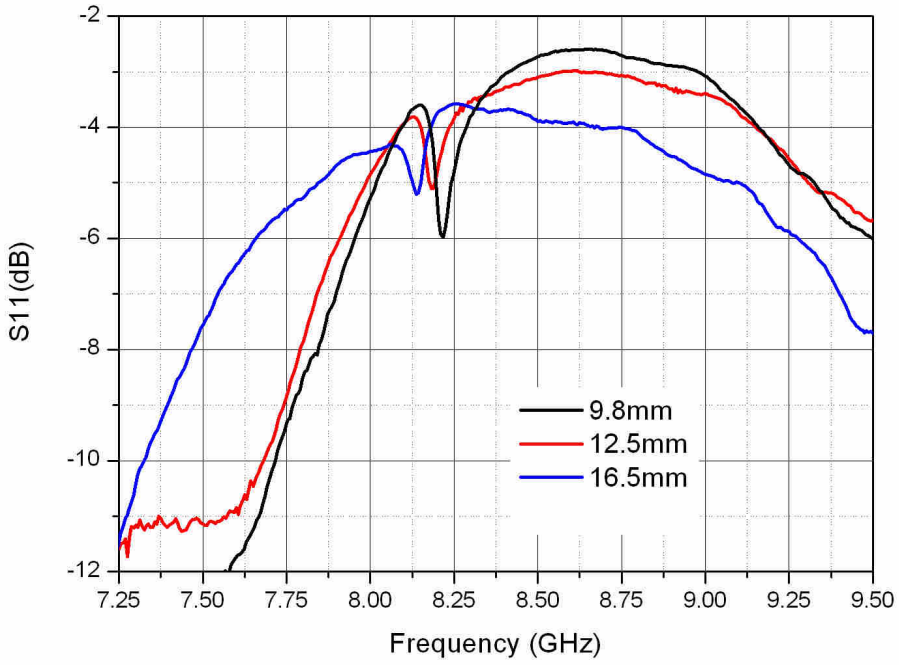

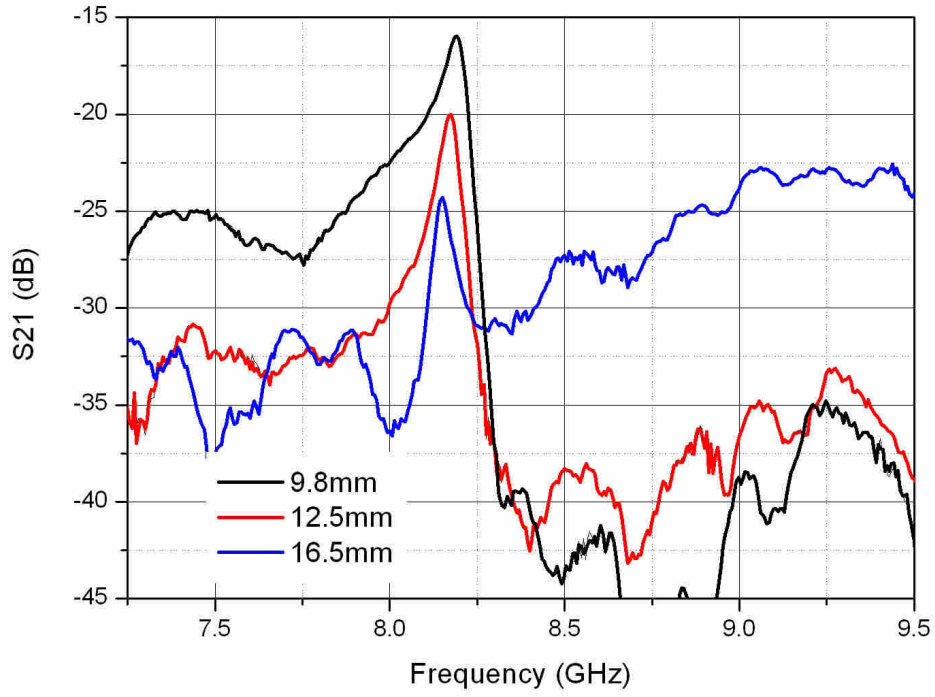

Figure 5.35 Measured S11 and S21 with the sensor beam of 80μm displacement

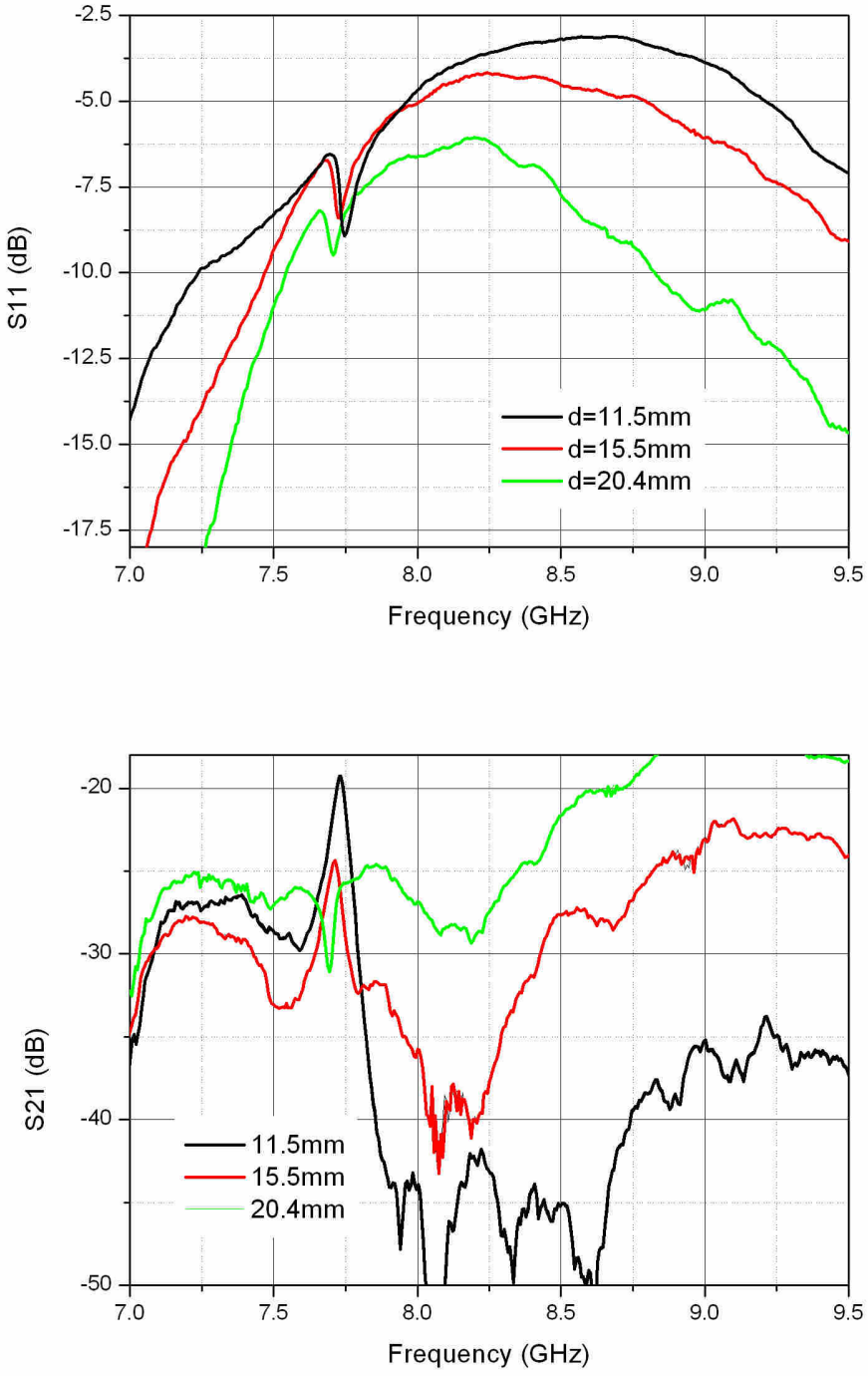

Figure 5.36 Measured S11 and S21 with the sensor beam of 110μm displacement

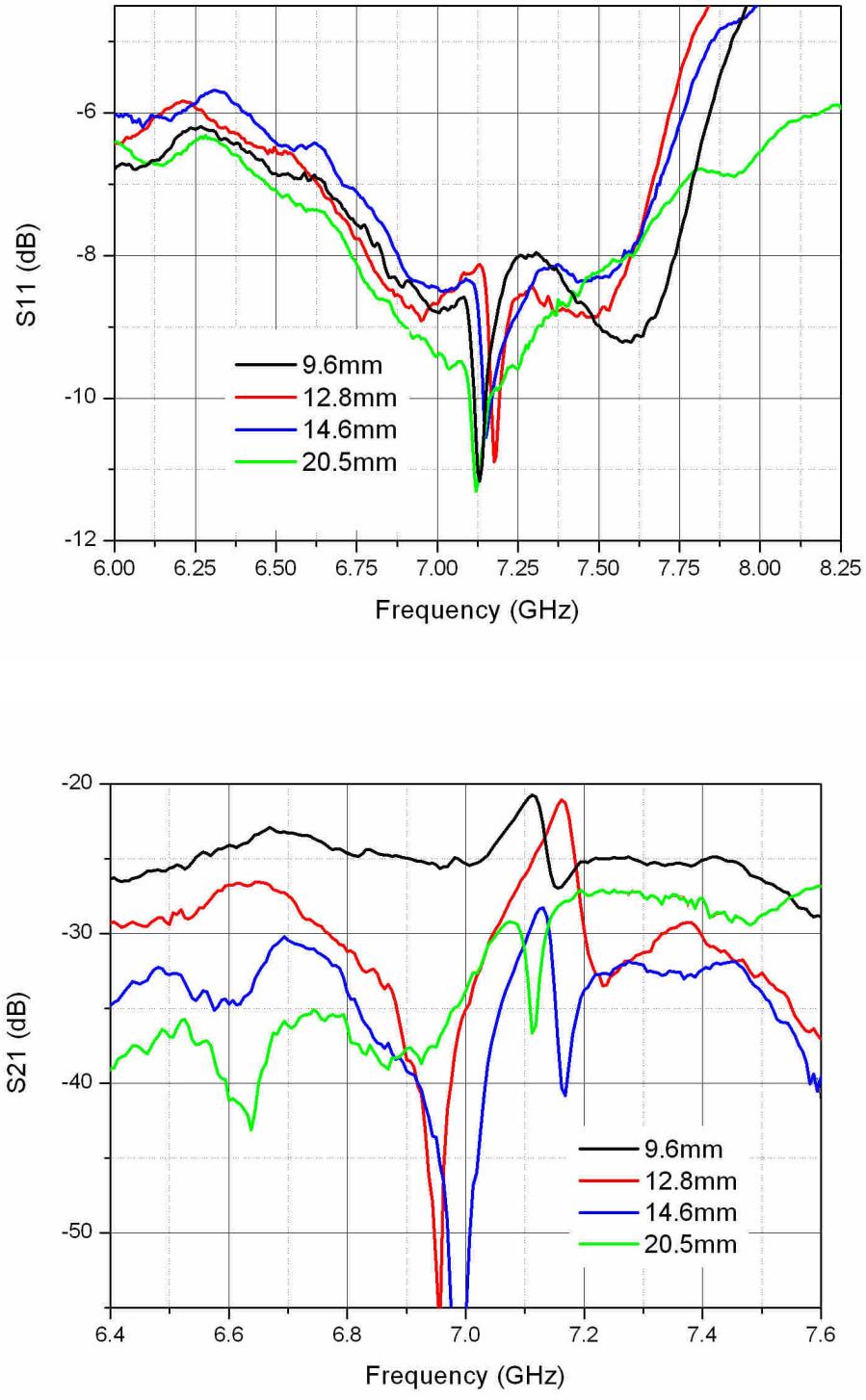

Figure 5.37 Measured S11 and S21 with the sensor beam of 140μm displacement

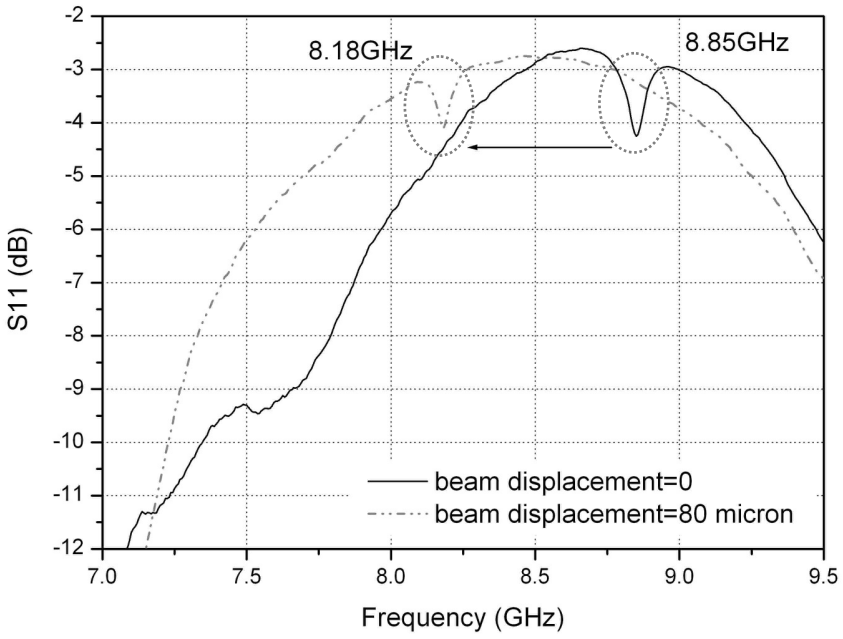

(a)

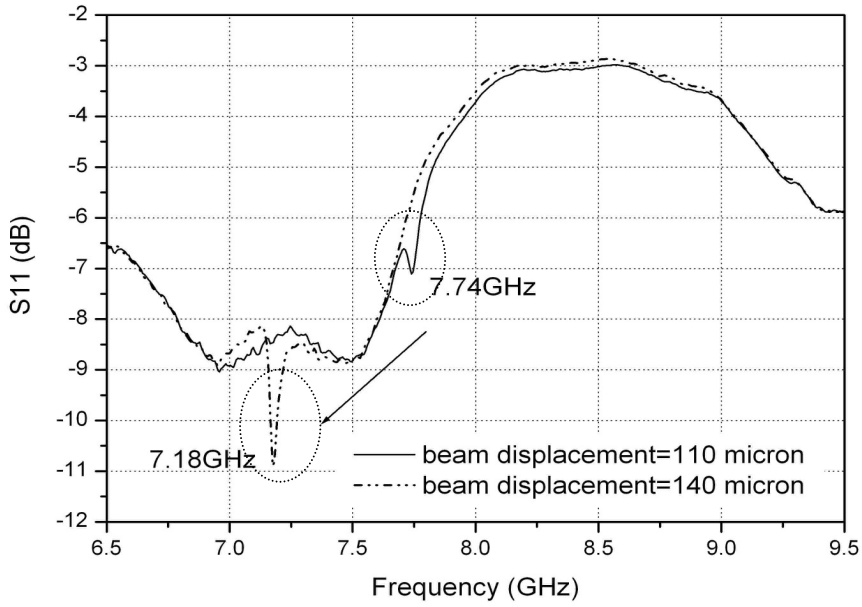

(b)

Figure 5.38 wireless measurement results
(a) S11 when beam displacement = 0 and 80 μm
(b) S11 when beam displacement = 110 and 140 μm

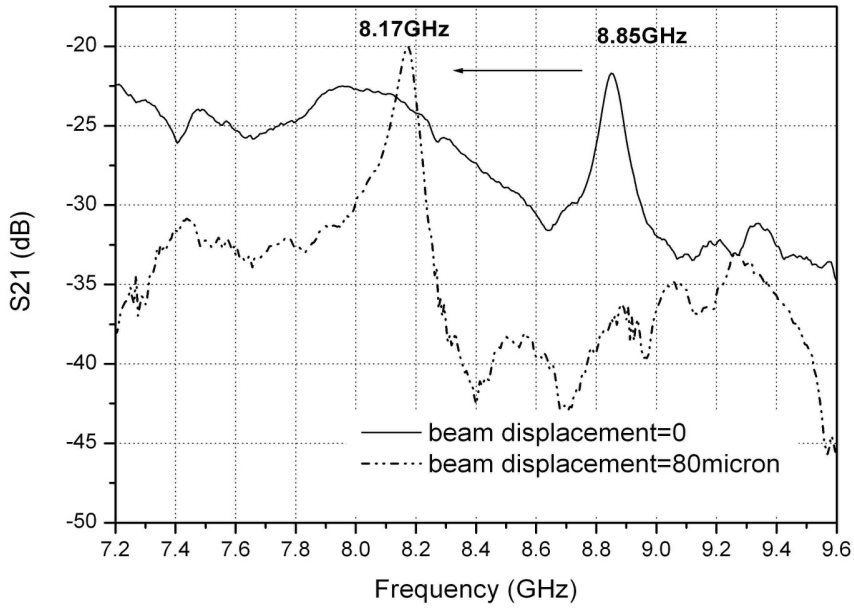

(a)

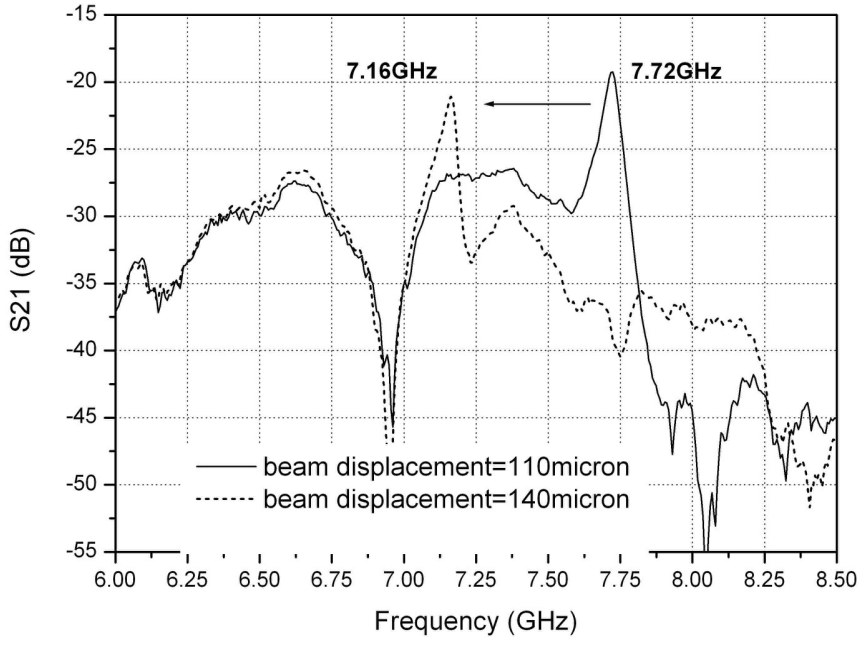

(b)

Figure 5.39 Wireless measurement result
(a) S21 when beam displacement = 0 and 80 μm
(b) S21 when beam displacement = 110 and 140 μm

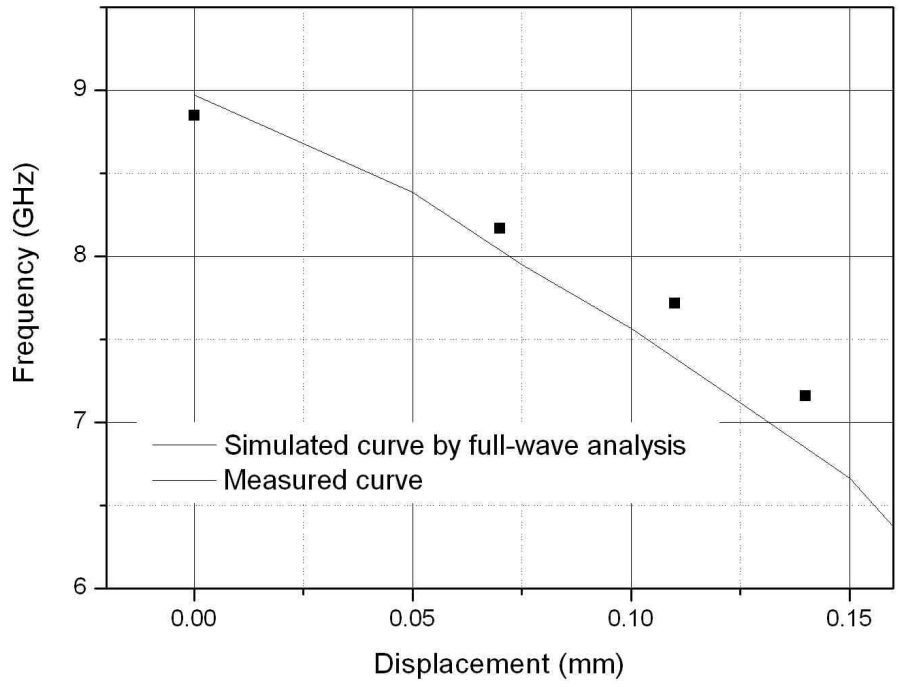

Figure 5.40 Wirelessly measured resonant frequency shift due to the displacement of the beam

5.4 Conclusion

In this chapter, the design concept of evanescent-mode cavity resonator as sensing elements has been presented. A simple circuit model is proposed for the sensitivity analysis. As one of the applications, an RF airflow sensor based on evanescent-mode cavity resonator has been developed. Miniature sensing beam and thin elastic membrane are used as a sensing structure to change the resonant frequency of a highly loaded RF resonator. Two sensor designs operating at about 21GHz and 14GHz are demonstrated. A novel CPW to cavity resonator transition is developed to excite a strong resonance. The

airflow sensor has shown a RF sensitivity of up to 1.4Ghz/degree, and an equivalent sensitivity of 0.36GHz/(m/s) for the airflow velocity measurement.

The wireless interrogation methods for the proposed airflow sensor have been also demonstrated. Wireless interrogation mechanisms based on the one-port and two-port detection have been demonstrated. To efficiently receive and transmit wireless signals, an ultra-wide-bandwidth (UWB) monopole antenna is designed for both the reader and sensor antennas. The design of CPW transition structures is also optimized by using full-wave analysis. The wireless measurement results show the resonance shift in all the S parameters due to the sensing beam displacement.

Chapter 6

Conclusion and Future Work

6.1. Summary

The research objective of this thesis is to develop a low cost and high efficiency fabrication technique for micromachined RF components, and exploit this technique in the application areas of high performance RF components and wireless sensors applications. A series of 3-D polymer-core RF components based on air-lifting mechanisms have been developed, including a low loss CPW transmission line, a vertical monopole antenna, and an evanescent-mode high-Q cavity resonator. Furthermore, a new type of wireless passive sensor has been designed and demonstrated, and it use as an airflow sensor has been illustrated.

In the first portion of the thesis, the metal-transfer mechanism is introduced into the conventional micro molding process, creating a novel metal-transfer-molding technique particularly usefully for 3-D RF structures. Compared with SU-8 micromachining, the unique advantages of MTM in the fabrication of 3-D polymer-core structures have been demonstrated.

In the second portion of the thesis, several RF air-lifted components based on MTM technology are developed. All components showed greatly improved performance over their printed counterparts. The feasibility and usefulness of the MTM process in RF 3-D components has been successfully demonstrated.

In the last portion of the thesis, a new type of wireless passive airflow sensor based on RF evanescent-mode cavity resonator and the MTM technique is presented. The sensor prototype shows an excellent sensitivity for airflow velocity measurement and can be greatly improved by MEMS sensing structures. Wireless interrogation of the sensor has been developed by embedding ultra-wide-bandwidth (UWB) antennas.

6.2. Future Work

The developed fabrication technique in this thesis is believed to have great potential for high-performance RF passive components and integration. One possible future area of work is the integration of different types of air-lifted RF components on the same substrate. It is imperative to implement the front-end functionalities integrating a cavity-resonator-based duplexer and 3-D antenna structure such as monopole or horn. Greatly improved performance is expected for the micromachined 3-D front-end module.

Another possible future area of work is the further development of the wireless passive sensor based on an evanescent-mode cavity resonator. As shown in chapter 5, the same concept can be utilized in many sensing applications other than airflow velocity measurement, such as pressure, temperature, or strain. The mechanical sensing structures can be further developed using advanced MEMS technology and integrated with RF evanescent-mode cavity using advanced packaging technology. The RF design of the sensor can also be optimized, such as reducing the size of the embedded antenna. Since this type of structure has been already demonstrated to be very promising for passive wireless sensor applications, the sensor reader system enabling a longer interrogation

system can be developed instead of the network analyzer. It will be very exciting to develop a complete wireless passive sensor and interrogation system based on the high-sensitivity evanescent-mode cavity resonator and metal-transfer-molding (MTM) technique.

References

[1] WWW. TRIQUINT.COM

[2] J. H. Chen, P. Fedorenko, and J. S. Kenney, "A Low Voltage W-CDMA Polar Transmitter with Digital Envelope Path Gain Compensation," IEEE Microwave and Wireless Lett., Vol. 16, No. 7, pp. 428-30, July, 2006.

[3] Y. C. Park, R. Melville, R. C. Frye, and J. S. Kenney, "Dual-Band Transmitters using Digitally Predistorted Frequency Multipliers for Reconfigurable Radios," IEEE Trans. Microwave Theory and Tech. Vol. 53, No. 1, pp. 115-22, Jan. 2005.

[4] Felix K. Schwering, "Millimeter Wave Antennss," Proceedings of the IEEE, vol. 80, no. 1, pp. 92-102, January, 1992.

[5] Gabriel M. Rebeiz, "Millimeter-Wave and Terahertz Integrated Circuit Antennas," Proceedings of the IEEE, vol. 80, no. 11, pp. 1748-1770, November, 1992.

[6] Warren L. Stutzman and Gary A. Thiele, Antenna Theory and Design, John Wiley & Sons, Inc., New York, 1998.

[7] Sangwoo Han; Neeraj Lal; Chang-Ho Lee; B. Matinpour, J. Laskar, "Development of MMIC-based modules for multichannel RF/optical subcarrier multiplexed communications applications", IEEE Journal of Solid-State Circuits, Vol. 36, Iss.9, pp.1360-1364,Sept.2001

[8] D. M. Pozar, "Considerations for millimeter wave printed antennas", IEEE Transaction on Antenna and Propagation, vol. AP-31, no. 5, pp. 740-747, September 1983

[9] J. Papapolymerou, R. F. Drayton, Linda P. B. Katehi, "Micromachined Patch Antennas," IEEE Trans. Antennas and Propagation, Vol. 46, No. 2, 1998, pp. 275-283

[10] T.G. Lim, H.N. Ang, I.D. Robertson and B.L. Weiss, "Tapered slot antenna using photonic bandgap structure to reduce substrate effects", ELECTRONICS LETTERS, vol. 41 no. 7, pp. 393-394, Mar. 2005

[11] Sanghyo Lee, Sangsub Song, Youngmin Kim, Jangsoo Lee, Chang-Yul Cheon, Kwang-Seok Seo, and Youngwoo Kwon, "A V-Band Beam-Steering Antenna on a Thin-Film Substrate With a Flip-Chip Interconnection", IEEE Microwave and Wireless Components Letters, Vol.18, Iss.4, pp. 287-289, Apr. 2008

[12] Xiangying Wu, Ikuo Awai, Zhongyou Yan, K. Wada, and T. Moriyoshi, "Quality factor of coplanar waveguide resonators", 1999 Asia Pacific Microwave Conference, vol. 3, pp.670-673, Dec. 1999

[13] G. L. Matthaei, L. Young, and E. M. T. Jones, Microwvae Filters, Impedance Matching Networks, and Coupling Structures, Artech House, 1980.

[14] Ian C. Hunter, L Billonet, B. Jarry, and Pierre Guillon, “Microwave filters - applications and technology”, IEEE Trans. Microwave Theory & Tech., vol. 50, no. 3, pp. 794-805, Mar. 2002

[15] Giwan Yoon and Jae-Don Park, “Fabrication of ZnO-based film bulk acoustic resonator devices using W/SiO_2 multilayer reflector”, Electronics Letters, Vol.36, iss.16, pp.1435-1437, Aug. 2000

[16] J. J. Yao, “RF MEMS from a Device Perspective”, J. Micromech. Microeng. 10, 2000, R9 - R38

[17] A. Hierlemann, O. Brand, C. Hagleitner, H. Baltes, "Microfabrication techniques for chemical/biosensors," Proc. IEEE 91 (2003) 839-863.

[18] H. shin, P. J. Hesketh, B. Mizaikoff, and C. Kranz, "Batch Fabrication of Atomic Force Microscopy Probes with Recessed Integrated Ring Microelectrodes at a Wafer Level", Anal. Chem., 79 (13), 4769 -4777, May, 2007

[19] J. Y.-C. Chang, A. A. Abidi, and M. Gaitan, "Large Suspended Inductors on Silicon and Their Use in a 2-um CMOS RF Amplifier," IEEE Electron Device Letters, vol. 14, pp. 246-248, 1993.

[20] Ahn, C.H., Kim, Y.J., and Allen, M.G., "A Fully Integrated Planar Toroidal Inductor with a Micromachined Nickel-Iron Magnetic Bar," IEEE Transactions on Components, Packaging, and Manufacturing Technology, Part A, vol. 17, no. 3, pp. 463-469, 1994.

[21] Yong-Kyu Yoon, J.-W. Park, and M.G. Allen, “RF MEMS Based on Epoxy-Core Conductors,” Digest of Solid-State Sensor, Actuator, and Microsystems Workshop 2002, Hilton Head Island, South Carolina, pp.374-375, 2002.

[22] M. Ozgur, M. E. Zaghloul, and M. Gaitan, "Optimization of Backside Micromachined CMOS Inductors for RF Applications," IEEE International Symposium on Circuits and Systems, pp. 185-188, 2000.

[23] Choi, S.O., Yoon, Y.K., Allen, M.G., Hunt, A.T., “A tunable capacitor using an immiscible bifluidic dielectric,” 2004 IEEE MTT-S International Microwave Symposium Digest (IEEE Cat. No.04CH37535), 2004, pt. 2, p 873-6 Vol.2.

[24] Zheng, M, et. al, “Broadband microstrip patch antenna on micromachined silicon substrates”, Electronics Letters, Volume 34, Issue 1, 8 Jan. 1998, pp 3 – 4

[25] R. Katehi, et al.: 'Micromachined circuits for millimeter- and submillimeter-wave application', IEEE Antennas Propag. Mag., 1993, 35, pp. 9–17

[26] Lee, H.S.; Shin, D.H.; Chun, Y.H.; Kim, S.C.; Lim, B.O.; Baek, T.J.; Kim, S.K.; Park, H.C.; Rhee, J.K. "Design and characterisation of micromachined transmission line with dielectric post for millimeter-wave applications", Electronics Letters, Volume 39, Issue 25, 11 Dec. 2003 Page(s):1827 - 1828

[27] B. Pan, Yong-kyu Yoon, Yanzhu Zhao, J.Papapolymerou, M.M.Tentzeris and M.Allen, "A Broadband Surface-Micromachined 15-45 GHz Microstrip Coupler", Proceedings of 2005 IEEE-IMS Symposium, Long Beach, CA, June 2005.

[28] B. Pan; Yoon, Y.-K.; Ponchak, G.E.; Allen, M.G.; Papapolymerou, J.; Tentzeris, M.M.; "Analysis and Characterization of a High-Performance Ka-Band Surface Micromachined Elevated Patch Antenna," Antennas and Wireless Propagation Letters, Vol. 5, Issue 1, Dec. 2006, p. 511–514

[29] Yong-Kyu Yoon, B. Pan, M.M. Tentzeris, J. Papapolymerou, and M.G. Allen, "Surface-Micromachined Millimeter-Wave Antennas," International Conference on Solid-StateSensors, actuators, and microsystems (Transducers '05), Seoul, Korea, June 5-9, 2005, pp.1986-1989

[30] Yong-Kyu Yoon, B. Pan, J. Papapolymerou, M.M. Tentzeris, and M.G. Allen, "A Vertical W-band Surface-Micromachined Yagi-Uda Antenna," presented in IEEE AP-S International Symposium and USNC/URSI National Raid Science Meeting in Washington, DC, July 3-8, 2005

[31] Hill, M.J.; Papapolymerou, J.; Ziolkowski, R.W. "High-Q micromachined resonant cavities in a K-band diplexer configuration", IEEE Proceedings of Microwaves, Antennas and Propagation, Volume 148, Issue 5, Oct. 2001 Page(s):307 – 312

[32] Y. Li, B. Pan, C. Lugo, M. Tentzeris, and J. Papapolymerou, "Design and Characterization of a W-Band Micromachined Cavity Filter Including a Novel Integrated Transition From CPW Feeding Lines**",** IEEE MTT, vol.55, iss.12, pp. 2902-2910, Dec. 2007

[33] A. Matsuzawa, "RF-SoC - expectations and required conditions," IEEE Trans. Microwave Theory Tech., vol. 50, no. 1, pp. 245–253, Jan. 2002.

[34] R. R. Tummala, M. Swaminathan, M. M. Tentzeris, J. Laskar, G. K. Chang, S. Sitaraman, D. Keezer, et al., "The SOP for Miniaturized, Mixed-signal Computing, Communication, and Consumer Systems of the Next Decade", IEEE Transactions on Advanced Packaging Vol. 27, No. 2, 2004, pp. 250-267

[35] R. R. Tummala and J. Laskar, "Gigabit wireless: system-on-a-package technology", Proceedings of the IEEE, Vol.92, Iss.2, pp. 376-387, Feb. 2004

[36] J. H. Lee, G. DeJean, S. Sarkar, S. Pinel, K. Lim, et al., “Advanced 3-D LTCC system-on-package (SOP) architectures for highly integrated millimeter-wave wireless systems”, 34th European Microwave Conference, Vol. 2, Iss. 13, pp. 523-526, 2004

[37] M. M. Tentzeris, J. Laskar, J. Papapolymerou, et al., “3-D-Integrated RF and Millimeter-Wave Functions and Modules Using Liquid Crystal Polymer (LCP) System-on-Package Technology”, IEEE Transactions on Advanced Packaging, Vol. 27, No. 2, 2004

[38] O. Brand, "Microsensor integration into systems-on-chip," Proceedings of the IEEE, Vol. 94, pp.1160-1176, 2006

[39] Y.-J. Kim and M. G. Allen, "Surface Micromachined Solenoid Inductors for High Frequency Applications," IEEE Trans. Components, Packaging, and Manufacturing Technology, vol. Part C, 21, pp. 26-33, 1998.

[40] T.L. Willke and S.S. Gearhart, “LIGA micromachined planar transmission lines and filters,” IEEE Transactions on Microwave Theory and Techniques, vol. 45, pp. 1681–1688, 1997

[41] D. M. Pozar, Microwave Engineering, John Wiley & Sons, Inc. 2005

[42] J. Oh, J. Lee and C. Lee, “Plasma pretreatment of the Cu seed layer surface in Cu electroplating”, Materials Chemistry and Physics, Vol. 73, Iss.2-3, pp. 227-234, Jan. 2002

[43] X. Gong, A. Margomenos, B. Liu, S. Hajela, W. J. Chappell, and L. P. B. Katehi, “Precision Fabrication Techniques and Analysis on High-Q Evanescent-Mode Resonators and Filters of Different Geometries,” IEEE Transactions on Microwave Theory and Techniques, Vol. 52, No. 11, pp. 2557-2566, Nov. 2004.

[44] B. Liu, X. Gong, W. J. Chappell, "Layer-by-layer polymer stereolithography fabrication for three-dimensional RF components", IEEE MTT-S, Vol.2 pp. 481-484, 2004

[45] WWW.MICROCHEM.COM

[46] Y. Yoon, J. H. Park; F. Cros, and M.G. Allen, “Integrated vertical screen microfilter system using inclined SU-8 structures,” Proceedings of 16th IEEE MEMS, pp. 227-30, 2003

[47] Y. Zhao, X. Wu, Y. Yoon, J. H. Park, S.J. Kennedy, Z. Schwartz, B.D. Boyan, and M.G. Allen, “Fabrication of Micromachined Mold Masters for 3-D, High-aspect-ratio Cell Culturing Substrates”, Proceedings of 2005 ASME IMECE, IMECE2005-81991, pp.1-7, Nov. 2005

[48] R. L. Barber, M. K. Ghantasala, R. Divan, D. C. Mancini, E. C. Harvey, "An investigation of SU-8 resist adhesion in deep x-ray lithography of high-aspect-ratio structures", Proceedings of the SPIE, Volume 5276, pp. 85-91, 2004

[49] Y.K. Yoon, "Micromachined Components for RF Systems", Doctoral Dissertation, Georgia Institute of Technology, 2004

[50] Shen X-J, Pan L-W and Lin L, "Microplastic embossing process: experimental and theoretical characterizations", Sensors and Actuators A, 97–8 428–33, 2002

[51] Lehmacher S, Neyer A and Mederer F Polymer optical, "waveguides integrated in printed circuit boards", Proc. 27th. European Conf. Optical Communication (Amsterdam, Netherlands, 30 Sept–4 Oct 2001, pp 302–3, 2001

[52] Niggemann M, Blaesi B, Boerner V, Gombert A, Klicker M, Kuebler V, Lalanne P and Wittwer V, "Periodic microstructures for large area applications generated by holography", Conf. Physics, Theory, and Applications of Periodic Structures in Optics, Proc. SPIE 4438 108–15,2001

[53] Grigaliunas V, Kopustinskas V, Meskinis S, Margelevicius M, Mikulskas I and Tomasiunas R, "Replication technology for photonic band gap applications", Opt. Mater. 17 15–8, 2001

[54] Olsson A, Larsson O, Holm J, Lundbladh L, et al., "Valve-less diffuser micropumps fabricated using thermoplastic replication", Proc. IEEE Tenth Annu. Int. Workshop on Micro Electro Mechanical Systems, MEMS'97 (Nagoya, Japan, 26–30 Jan. 1997) pp 305–10

[55] Goll C, Bacher W, B¨ustgens B, Maas D, Menz W and Schomburg W K, "Microvalves with bistable buckled polymer diaphragms", J. Micromech. Microeng. **6** 77–9, 1996

[56] Grass B, Neyer A, Johnck M, Siepe D, Eisenbeiss F, Weber G and Hergenroder R, "A new PMMA-microchip device for isotachophoresis with integrated conductivity detector", Sensors Actuators B **72** 249–58, 2001

[57] Dittmann D, Ahrens R, Rummler Z, Schlote-Holubek K and Schomburg W K, "Low-cost flow transducer fabricated with the AMANDA process", 11th Int. Conf. on Solid-State Sensors and Actuators, Transducers'01 (Munich, Germany,10–14 June 2001) paper 4B2.10P

[58] C.P.Wong, et al, "Recent Advances in Plastic Packaging of Flip-Chip and Multichip Modules (MCM) of Microelectronics", IEEE Transactions on Components and Packaging Technology, Vol. 22, No. 1, 1999, pp.21

[59] R. R. Tummala, et al, Microelectronic Packaging, Handbook. New York: Van Nostrand Reinhold, 1989.

[60] Malaquin L, Carcenac F, Vieu C and Mauzac M, "Using polydimethylsiloxane as a thermocurable resist for a soft imprint lithography process, Microelectron. Eng. 61–62 379–84

[61] E. Kim, Y. N. Xia, and G. M. Whitesides, "Unconventional Approaches for Advanced Nanotechnology", J. Am. Chem. Soc. 118, 5722 (1996).

[62] Y. Xia and G. M. Whitesides, "Review: Soft Lithography", Angew. Chem., Int. Ed. 37, 550 (1998).

[63] S.O. Choi, J.H. Park, Y. Kim, H.S. Gill, Y. Choi, M.G. Allen and M.R. Prausnitz, "Microneedle electrode array for electroporation of skin for gene therapy", 32nd Annual Meeting & Exposition of the Controlled Release Society, 2005

[64] X. Wu, Y. Zhao, Yong-Kyu Yoon, S.O. Choi, J.H. Park, and M.G. Allen, "Wafer-scale Micromolding of Unitary Polymeric Microstructures with Simultaneously Formed Functional Metal Surface", Proceeding of International Conference on micro Total Analysis Systems, pp.205-207, Oct. 2005.

[65] J. Zaumseil, M. A. Meitl, J. W. P. Hsu, B. R. Acharya, K. W. Baldwin, Y. L. Loo, and J. A. Rogers, "Three-dimensional and Multilayer Nanostructures Formed by Nanotransfer Printing", Nano Lett., 3, 1223 (2003).

[66] J. Zaumseil, K. W. Baldwin, and J. A. Rogers, "Electrical Characteristics of Organic Transistors Formed by Soft Contact Lamination", J. Appl. Phys., 93, 6117 (2003).

[67] T. W. Lee, J. Zaumseil, Z. Bao, J. W. P. Hsu, and J. A. Rogers, "Organic light-emitting diodes formed by soft contact lamination", Proc. Natl. Acad. Sci. U.S.A. 101, 429 (2004).

[68] C. Kim, P. E. Burrows, and S. R. Forrest, "Micropatterning of organic electronic devices by cold-welding", Science, 288, 831 (2000).

[69] J. Rhee and H. H. Lee, "Patterning organic light-emitting diodes by cathode transfer", Appl. Phys. Lett., 81, 4165 (2002).

[70] G. Blanchet, Y. L. Loo, J. A. Rogers, F. Gao, and C. R. Fincher, "Large area, high resolution, dry printing of conducting polymers for organic electronics", Appl. Phys. Lett. 82, 463 (2003).

[71] J. A. Rogers, et al, "Nanotransfer printing by use of noncovalent surface forces: Applications to thin-film transistors that use single-walled carbon nanotube networks and semiconducting polymers**",** Applied Physics Letters, 85, 5730 (2004)

[72] J. Brandrup, E.H. Immerqut, and E. A.Grulke, Polymer Handbook, Wiley-Interscience, 2003

[73] W. Hu, B. Yang, C. Peng, and S. W. Pang, “Three-dimensional SU-8 structures by reversal UV imprint”, J. Vac. Sci. Technol. B, vol.24, no. 5, pp.2225-2229, Sep. 2006

[74] Stephane A. Page, Raffaele Mezzenga, Louis Boogh, John C. Berg, Jan-Anders E. Manson, “Surface Energetics Evolution during Processing of Epoxy Resins”, Journal of Colloid and Interface Science, vol.222, iss.1, pp. 55-62, Feb. 2000

[75] Y. Kwon, H. T. Kim, J. H. Park, Y. K. Kim, "Low-loss micromachined inverted overlay CPW lines with wideimpedance ranges and inherent airbridge connection capability", Microwave and Wireless Components Letters, IEEE Volume 11, Issue 2, Feb 2001 Page(s):59 - 61

[76] Leung, L.L.W., et al, "Characterization and attenuation mechanism of CMOS compatible micromachined edge-suspended coplanar waveguides on low-resistivity silicon substrate", IEEE transactions on Components, Packaging and Manufacturing Technology, Part B: Advanced Packaging, Volume 29, Issue 3, Aug. 2006 PP.496 – 503

[77] Katehi, L.P. et al, "Miniature stub and filter designs using the microshield transmission line", Microwave Symposium Digest, 1995, IEEE MTT-S International, 16-20 May 1995 PP675 - 678 vol.2

[78] Warren L. Stutzman and Gary A. Thiele, Antenna Theory and Design, Chapter 2 and 5, John Wiley & Sons, Inc., New York, 1998.

[79] Iyer, M.K.; Seager, R.D.; Vardaxoglou, J.C., "Wireless chip to chip interconnection for multichip modules usingleaky wave antennas", Electronics Letters
Volume 29, Issue 23, 11 Nov 1993 Page(s):2030 - 2031

[80] P. Blondy, A. R. Brown, D. Cros, and G. M. Rebeiz, “Low-loss micromachined filters for millimeter-wave communication systems," IEEE Trans. Microwave Theory and Tech., vol. 46, no. 12, pp. 2283{2288, December 1998.

[81] C.-Y. Chi and G. M. Rebeiz, “A low-loss 20 GHz micromachined bandpass filter," IEEE MTT-S Int. Microwave Symp. Dig., Orlando, FL, May 1995, pp. 1531-1534.

[81] L. P. B. Katehi, G. M. Rebeiz, and C. T.-C. Nguyen, “MEMS and si-micromachined components for low-power, high-frequency communications systems," IEEE MTT-S Int. Microwave Symp. Dig., vol. 1, Baltimore, MD, June 1998, pp. 331-333.

[82] A. KIinlenko, L. Rud, V. Tkachenko, and D. Kulik, “Evanescent-mode ridged waveguide bandpass filters with improved performance,” IEEE Trans. Microwave Theory & Tech., vol. 50, no. 3, pp. 1324-1327, May 2002

[83] R. Levy, R. V. Snyder, and G. Matthaei, “Design of microwave filters,” IEEE Trans. Microwave Theory & Tech., vol. 50, no. 3, pp. 7830793, Mar. 2002

[84] R. V. Snyder, S. Sanghoon, and K. Keck, “Bandstop filter design using evanescent mode resonators,” 2001 IEEE MTT-S Int. Microwave Symp. Dig., vol. 3, pp. 20-25, May 2001

[85] Y. Rong, K. A. Zaki, M. Hageman, D. Stevens, and J. Gipprich, “Low-temperature cofired ceramic (LTCC) ridge waveguide bandpass chip filters,” IEEE Trans. Microwave Theory & Tech., vol. 47, pp. 2317-2324, Dec. 1999

[86] M.G.Allen, “Micromachined Endovascularly-Implantable Wireless Aneurysm Pressure Sensor: From Concept to Clinic”, Proc. Transducers 2005, Vol1, pp275-278

[87] DeHennis, A.D.; Wise, K.D., "A fully integrated multisite pressure sensor for wireless arterial flow characterization", Journal of Microelectromechanical Systems, Volume 15, Issue 3, Page(s):678 - 685, June 2006

[88] J. H. Seo, and O. Brand, "High-Q factor resonant sensor platform for chemical and biological applications”, Proc. Transducers ’05, pp. 593-596

[89] Klaus Finkenzeller, RFID Handbook: Fundamentals and Applications in Contactless Smart Cards and Identification, Wiley, 2003

[89] Fonseca, M.A.; English, J.M.; von Arx, M.; and Allen, M.G., "Wireless Micromachined Ceramic Pressure Sensor for High Temperature Applications," IEEE J. Microelectromechanical Systems, vol. 11, no.4, p. 337-43 (2002)

[90] J. Chuang, D.J. Thomson, and G.E.Bridges, “Embeddable wireless strain sensor based on resonant RF cavities”, Review of Scientfic Instruments, 76, 094703, 2005

[91] Matova, S.P.; Makinwa, K.A.A.; Huijsing, J.H. “Compensation of packaging asymmetry in a 2-D wind sensor,” IEEE Sensors Journal 2003, 3, 761-765.

[92] Mailly, F.; Giani, A.; Bonnot, R.; Temple-Boyer, P.; Pascal-Delannoy, F., Foucaran, A.; Boyer, A. “Anemometer with hot platinum thin film,” Sensors and Actuators A 2001, 94, 32-38.

[93] Kim, S.; Nam, T.; Park, S. “Measurement of flow direction and velocity using a micromachined flow sensor,” Sensors and Actuators A 2004, 114, 312-318

[94] Joshi, Himanshu; Sigmarsson, Hjalti H.; Peroulis, Dimitrios; Chappell, William J., "Highly Loaded Evanescent Cavities for Widely Tunable High-Q Filters," 2007 IEEE/MTT-S International, pp.2133-2136, 3-8 June 2007.

[95] M.Yanagi, S.Kurashima, T. Arita and T. Kobayashi , “Planar UWB Monopole Antenna Formed on a Printed Circuit Board”, FUJITSU COMPONENT LIMITED. http:// www.fcai.fujitsu.com/pdf/uwb_monopole_antenna.pdf